

## Copyright Undertaking

This thesis is protected by copyright, with all rights reserved.

**By reading and using the thesis, the reader understands and agrees to the following terms:**

1. The reader will abide by the rules and legal ordinances governing copyright regarding the use of the thesis.
2. The reader will use the thesis for the purpose of research or private study only and not for distribution or further reproduction or any other purpose.
3. The reader agrees to indemnify and hold the University harmless from and against any loss, damage, cost, liability or expenses arising from copyright infringement or unauthorized usage.

### IMPORTANT

If you have reasons to believe that any materials in this thesis are deemed not suitable to be distributed in this form, or a copyright owner having difficulty with the material being included in our database, please contact [lbsys@polyu.edu.hk](mailto:lbsys@polyu.edu.hk) providing details. The Library will look into your claim and consider taking remedial action upon receipt of the written requests.

**VISUALIZING ATOMS AND ELECTRONS FOR  
STRUCTURE-PROPERTY RELATIONSHIP BY  
TRANSMISSION ELECTRON MICROSCOPY**

**WONG LOK WING**

**PhD**

**The Hong Kong Polytechnic University**

**2023**

**The Hong Kong Polytechnic University**

**Department of Applied Physics**

**Visualizing Atoms and Electrons for Structure-  
Property Relationship by Transmission Electron  
Microscopy**

**WONG Lok Wing**

A thesis submitted in partial fulfilment of the requirements for  
the degree of Doctor of Philosophy

**December 2022**

# **CERTIFICATE OF ORIGINALITY**

I hereby declare that this thesis is my own work and that, to the best of my knowledge and belief, it reproduces no material previously published or written, nor material that has been accepted for the award of any other degree or diploma, except where due acknowledgement has been made in the text.

\_\_\_\_\_ (Signature)

WONG Lok Wing (Name of candidate)





# Abstract

Beyond the discovery of extraordinary properties and potential next-generation applications of low-dimensional carbon family: fullerene, carbon nanotube, and graphene, there are abundant low-dimensional materials are tremendously investigated to reproduce the success of the low-dimensional carbon family. The smaller and better characteristics provide the opportunities to fabrications of high-performance devices. However, there are still a lot of mysteries of the emerged low-dimensional materials, for example, large scale and controllable synthesis, exceptional properties (for example, super-plasticity), and the fundamental physical and chemical questions (for instance, the bonding, and their accurate atomic structure).

In order to unveil the mysteries, atomic structures and nanomanipulations are needed to explore the full pictures of structure-property relationships. Transmission electron microscopy provides the opportunity to study to the low-dimensional materials in atomic scale. Although transmission electron microscopy is a powerful instrument, the experiments and data analysis are difficult, especially for the advanced techniques, like 4D-STEM. Thus, the appropriate technique is chosen to study and analyze the specimen is the key. Combining with other techniques and instruments, the preliminary checks of specimens can be done before implementing transmission electron microscopy.

In this thesis, only *ex situ* atomic scale and *in situ* micro scale experiments have been conducted to study the growth kinetics as well as intermediate species of synthesis, exceptional plasticity of 2D materials, and quantitative dDPC-STEM for MOFs and atomic columns by using transmission electron microscopy. The first 2 topics mainly use the conventional STEM techniques with the specific specimen preparation methods to



show the intermediate structures to analyze the whole picture of mechanisms. First, the critical intermediate species octahedral  $\text{Re}_6\text{Se}_8$  was found that reduced by hydrogen from the precursors in atmosphere, that is the key to the nucleation and epitaxial growth. Second, the exceptional plasticity of InSe has been comprehensively investigated by microscopic view and macroscopic view. The overlooked phase transition from 2H to 3R increases the gliding barrier significantly as high as 24.07%, that ceases the micro-crack propagation surrounded. Hence, the excellent plasticity of InSe is caused by the synergetic effect of strain relaxation, phase transition, strain accumulation, and structural strengthening. Finally, statistical measurements have been conducted to minimize the low SNR problem of dDPC-STEM, that provide not only the coordination number, but also the lower energy site, that provides the insight to the structural engineering of metal-organic frameworks.

In the near future, *in situ* atomic scale studies will be applied to unveil more mechanism of the low-dimensional materials' properties. It depends on the complete installation of a new transmission electron microscopy due to the delay caused by COVID-19 pandemic. On the other hand, the general rule of brittle-ductile materials will be investigated by either computational based or experimental based methods. Besides, the undiscovered dDPC-STEM will be further studied from the big data.



# Acknowledgements

It is a pleasure to thank my supervisor, **Dr. Jiong ZHAO**, for 5-year supervision including my MPhil degree. He provides numerous opportunities to study different techniques related to TEM. He always provides new insights that I did not notice. That makes me think deeply and widely.

Thank you for **Prof. Shu Ping LAU**, **Prof. Jianhua HAO**, **Prof. Xuming ZHANG**, **Prof. Jiyan DAI**, **Prof. Feng YAN**, **Dr. Yuen Hong TSANG**, **Dr. Ming YANG**, **Dr. Zhiyang Yu**, **Prof. Qingming Deng**, and **Dr. Thuc Hue Ly**, for providing valuable collaborations and specimens, that I can apply my knowledge to contribute to their works.

Especially thanks for **Dr. Thuc Hue LY** and **Mr. Xin CHEN**, for providing many high-quality CVD grown 2D specimens, the characterization of Raman, PL, and AFM, and sharing the specimen transfer experiences (**ReSe<sub>2</sub>** in **Chapter 3**). Also, thanks for **Dr. Dengrong SUN** and **Mr. Hok Yin WONG**, the MOFs (Ni-BDC and Ni-BDC<sub>9</sub>ATA in **Chapter 5**) are well prepared.

On the other hand, greatly thanks for **Prof. Qingming DENG** (in **Chapter 3** & **Chapter 5**), **Dr. Ming YANG** (in **Chapter 4**), and **Dr. Ke YANG** (in **Chapter 4**), for the DFT calculation by using VASP.

Another thanks for **Dr. Nicolas ONOFRIO** for his course “Atomistic view of matter: modeling & simulation” in 2020. I have studied the basis of MD, LAMMPS, and Quantum ESPRESSO. Finally, LAMMPS can be applied to my study in **Chapter 4**.



I am appreciative to **Dr. Wei LU**, and **Dr. Yuan CAI**, for sharing their experiences on different TEMs and keeping the TEM center runs well.

I'm so grateful to **all supporting staff** in **Department of Applied Physics** for helping us deals with the administrative works.

Finally, it is hard to find words to express my gratitude to all my (ex-)groupmates: **Dr. Fangyuan ZHENG, Dr. Wei HAN, Dr. Qiang FU, Dr. Xiaodong ZHANG, Dr. Dengrong SUN, Dr. Hui DONG, Dr. Quoc Huy THI, Mr. Ka Hei LAI, Mr. Hok Yin WONG, Mr. Shan JIANG, Mr. Tianren CHEN, Mr. Chi Shing Ben TSANG, Mr. Zhangyuan YAN** and **Ms. Wenqian SHEN**, and my peers who have known since undergraduate: **Dr. Ping Kwong CHENG, Dr. Sin Yi PANG, Mr. Chun Ki LIU** for supporting technically and emotionally.



# Table of Contents

CERTIFICATE OF ORIGINALITY .....	iii
Abstract .....	iv
Acknowledgements .....	vi
Table of Contents .....	viii
List of Figures .....	xii
List of Tables.....	xxiv
List of Publications .....	xxv
List of Abbreviations.....	xxx
Chapter 1.     Introduction .....	1
<b>1.1.     Applications of transmission electron microscopy.....</b>	<b>4</b>
<b>1.2.     Synthesis kinetics in two-dimensional materials .....</b>	<b>10</b>
<b>1.3.     Unexpected plasticity in vdW materials.....</b>	<b>15</b>
<b>1.4.     Quantitative charge density study of hydrogen bonds in MOFs .....</b>	<b>20</b>
<b>1.5.     Summary.....</b>	<b>23</b>
Chapter 2.     TEM: History, Principle and Experiment Preparations .....	25
<b>2.1.     Introduction to transmission electron microscopy .....</b>	<b>27</b>
<b>2.2.     Introduction to scanning transmission electron microscopy .....</b>	<b>34</b>
<b>2.3.     Introduction to integrated differential phase contrast .....</b>	<b>40</b>



2.4.	Introduction of energy dispersive x-ray spectroscopy .....	42
2.5.	Introduction to electron energy loss spectroscopy .....	44
2.6.	Specimen preparations .....	48
2.7.	<i>In situ</i> AFM tip preparations .....	49
2.8.	Summary .....	49
Chapter 3. Unveiling the Nucleation and Growth Kinetics of Rhenium Diselenide		50
3.1.	Introduction .....	51
3.2.	Methodology .....	53
3.2.1.	Rhenium diselenide preparations .....	53
3.2.2.	Topographical measurement .....	54
3.2.3.	Optical characterizations .....	55
3.2.4.	Transmission electron microscopy and imaging simulations .....	55
3.2.5.	Density functional theory simulation .....	56
3.3.	Results and discussion .....	56
3.3.1.	2D ReSe <sub>2</sub> morphology and characterization .....	57
3.3.2.	Identification of Re <sub>x</sub> Se <sub>y</sub> molecular clusters .....	61
3.3.3.	Key reactions and intermediate steps involved in growth .....	64
3.4.	Summary .....	69
Chapter 4. Unexpected Plasticity in VdW Materials .....		70
4.1.	Introduction .....	70
4.2.	Methodology .....	73



4.2.1.	Specimen preparations and experimental design .....	74
4.2.2.	Preliminary characterizations .....	74
4.2.3.	(S)TEM characterizations .....	74
4.2.4.	<i>In situ</i> TEM .....	75
4.2.5.	Thickness estimation in HAADF-STEM .....	75
4.2.6.	HAADF-STEM simulations .....	75
4.2.7.	Molecular dynamics .....	75
4.2.8.	DFT calculations .....	76
4.2.9.	Mechanical properties from the elastic constants .....	77
4.3.	Results .....	78
4.3.1.	The atomic structures close to micro-cracks .....	80
4.3.2.	Mechanical manipulations by <i>in situ</i> TEM .....	85
4.3.3.	Phase transition barrier and interlayer gliding barrier .....	87
4.3.4.	Macroscopic view via elastic constants .....	91
4.3.5.	The origin of ultra-high plasticity .....	92
4.4.	Summary .....	94
Chapter 5.	Quantitative Charge Density Study of Hydrogen in MOFs .....	96
5.1.	Introduction .....	96
5.2.	Methodology .....	97
5.2.1.	Specimen preparations .....	97
5.2.2.	STEM characterization .....	97



5.2.3.	Density functional theory simulation .....	98
5.2.4.	DDPC-STEM image simulations .....	99
5.3.	Results and discussion .....	99
5.3.1.	Modeling Ni-BDC by direct observation .....	99
5.3.2.	Amino acid in Ni-BDC <sub>9</sub> ATA .....	101
5.3.3.	ATA orientation preference .....	103
5.3.4.	Quantitative study of the charge density with hydrogen.....	104
5.4.	Summary .....	105
Chapter 6.	Conclusion and Outlook.....	107
Appendices	.....	109
Reference	.....	110





# List of Figures

Figure 1. Low-dimensional materials beyond carbon family. The categories are divided by the number of atom thickness. ....	2
Figure 2. Typical background subtracted and deconvoluted EELS spectra of C-K edge and Mn-L <sub>2,3</sub> edge. a, EELS spectra of C-K edge from different C and different minerals containing C <sup>54</sup> . b,c, (b) EELS spectra of different valence and coordination number of Mn with the corresponding (c) Table about L <sub>2,3</sub> peak distances and L <sub>2,3</sub> integrated peak ratio <sup>55</sup> . ....	5
Figure 3. Phonon dispersion of graphite and h-BN resolved by EELS spectra. a,b, Series of phonon EELS spectra of (a) graphite, and (b) h-BN. c,d, Momentum intensity maps with DFT simulation results of (c) graphite, and (d) h-BN <sup>57</sup> . ....	6
Figure 4. A summary of <i>in situ</i> TEM. a, Overview of <i>in situ</i> TEM <sup>58</sup> . b, Recent progress of mechanical studies via <i>in situ</i> TEM. The images contribution as follows: compression <sup>60,61</sup> , tensile <sup>62-64</sup> , bending <sup>65,66</sup> , and shearing <sup>67,68</sup> were arranged by Li <i>et al.</i> <sup>59</sup> . ....	7
Figure 5. Mass transportation mechanisms by electrical bias in multiwall CNT <sup>69</sup> . ....	7
Figure 6. Electrochemical studies of Li ion batteries <sup>70</sup> . a, Serial images of Li ion transportation cropped from a video from 0 to 54 s. b, Different type of anode materials. ....	8
Figure 7. Graphene liquid cell design and performance. a, Scheme of double liquid cell. b, A HAADF-STEM image of the homemade liquid cell. Scale bar: 2 $\mu\text{m}$ . c-e, HAADF-STEM images of defocus (c) -42 nm, (d) 0 nm, and (e) 28 nm. Scale bars: 5 nm. Images from (a-e) are reproduced from Ref. <sup>71</sup> . f, A scheme of graphene liquid cell. g, Serial	



images of Pt nanocrystal with a twin boundary under irradiation. Scale bar: 2 nm. Images from (f,g) are reproduced from Ref. <sup>72</sup> .....	9
Figure 8. Comparison between experimental and theoretical projected charge density. a, Experiment. b, DFT simulation. c, Line profile of the black dashed line in (a&b). Images (a-c) are reproduced from Ref. <sup>73</sup> .....	9
Figure 9. Schematic of the three-step synthesis model. a, (I) evaporation of precursors and reduction of $\text{MoO}_3$ to $\text{MoO}_x$ , (II) Condensation of $\text{MoO}_{0.79}\text{Se}_{0.24}$ on the $\text{SiO}_2/\text{Si}$ substrate, and (III) further selenization of the $\text{MoSe}_2$ formation assisted by the aligned nanoparticle $\text{MoO}_2$ . b, Car-Parrinello molecular dynamics simulation atomic model in top view and side view. Figure 9 is reproduced from Ref. <sup>87</sup> .....	11
Figure 10. Scheme of the three-step growth model. The vaporized reactants form a $\text{MoOS}_2$ island. Then, the further vaporization and sulfurization forms $\text{MoS}_2$ monolayer <sup>88</sup> . .....	12
Figure 11. Schematics of nucleation and growth kinetics of $\text{MoS}_2$ . a-c, high and (d-f) low concentration of reactants by controlling the gas flux <sup>89</sup> .....	13
Figure 12. Schematics of nucleation and growth kinetics of $\text{MoS}_2$ in low and high concentration of reactants by controlling the gas flux and temperature <sup>90</sup> .....	13
Figure 13. Optical images with spectroscopy. a, <i>In situ</i> images during growth and the deposition of $\text{MoO}_2$ on a $\text{SiO}_2/\text{Si}$ substrate. Scale bar is 80 $\mu\text{m}$ . b, Ex situ Raman spectra of the marked areas in (a), and c, Ex situ XPS spectrum of the deposited $\text{MoO}_2$ film. Figure 13 is reproduced from Ref. <sup>91</sup> . ....	14
Figure 14. Substrate effect in terms of coverage and energy comparison. a, Serial images of soda-lime glass from 2 to 8 mins. b, Serial images of quartz glass from 10 to 70 mins. Scale bars are 100 $\mu\text{m}$ in (a) and 50 $\mu\text{m}$ in (b). c, $\text{MoS}_2$ coverage comparison between soda-lime glass and quartz. d, $\text{MoS}_2$ coverage comparison between NaCl coating quartz	



and downstream positioned quartz. e,f, DFT calculated epitaxial growth energy diagram, (e) without, and (f) with sodium adsorption. Figure 14 is reproduced from Ref. <sup>83</sup> . .....	14
Figure 15. The exceptional plasticity of InSe. A, Structure of $\beta$ -InSe. B, An image of an as-grown $\beta$ -InSe crystal, and C, its cleavage surface. D-F, The origami of the $\beta$ -InSe crystal. G, Cross section scanning electron microscopy (SEM) image of a folded $\beta$ -InSe. H,I, Compression engineering stress-strain experiment along (H) out-of-plane, and (I) in-plane direction. Figure 15 is reproduced from Ref. <sup>92</sup> . .....	16
Figure 16. Mechanical and chemical properties of $\beta$ -InSe. A, Comparison of intralayer modulus in the perspective of hexagonal 2D inorganic semiconductors. B, DFT calculated slipping energy and cleavage energy in comparisons with other materials. C-I, Calculated differential charge density (C) in perspective view, (D) along $1210$ , (E) charge density, (F) electron localization function (ELF), crystal orbital Hamiltonian populations (COHP) for (G) interlayer In-Se bonding, (H) intralayer In-Se bonding and (I) Intralayer In-In bonding <sup>92</sup> . .....	17
Figure 17. Different prediction of the materials which is ductile or brittle. a, Deformability factor <sup>92</sup> . b, Pugh-Pettifor criterion <sup>96</sup> . Blue vertical dashed line is 0.57. ....	17
Figure 18. ADF-STEM images of a deformed InSe. A, Atomic image, and the slipping steps along $[0001]$ . B,C, Cross section view along (B) $1210$ , and (C) $1010$ <sup>92</sup> . ....	18
Figure 19. Atomic structure of $\beta$ - and $\gamma$ -InSe along $1210$ and $0001$ . The red dashed lines indicate the difference of stacking order and the black dashed lines show a unit of $1010$ direction. ....	19
Figure 20. XRD $\theta$ - $2\theta$ experiments. a, XRD pattern of a cleaved InSe surface. b, XRD data of InSe before and after roller pressing <sup>92</sup> . c,d, XRD patterns of commercial products of (c) $\beta$ phase InSe <sup>101</sup> and (d) $\gamma$ phase InSe <sup>102</sup> . ....	19



Figure 21. Experimental scheme of the external force onto the $\beta$ -InSe single crystal...	20
Figure 22. Hydrogen acquired by STEM. a-b, ABF-STEM image of a, $\text{YH}_2^{104}$ and b, protonated $\text{H}_x\text{SrCoO}_{2.5}^{105}$ . H-H dimers are indicated by orange arrows in (b). c-e, $\alpha$ -Ti to $\gamma$ -TiH interface images taken by (c) contrast inverted ABF-STEM, (d) iDPC-STEM, and (e) contrast inverted dDPC-STEM <sup>103</sup> . Field of view: 3.5 x 3.5 nm in (c-e). The boxes in (a,c-e) display the simulated images. ....	21
Figure 23. Images of a single 8-hydroxyquinoline on Cu (111). a, Theoretic structure. b, DFT simulated electron density maps. c, Scanning tunnelling microscopy (STM) topography image. d-f, Constant-height AFM frequency shift images with respect to the Cu substrate. The height above the Cu substrate is (d) 30 pm, (e) 10 pm, and (f) 0 pm <sup>106</sup> . ....	22
Figure 24. Examples of zeolites and MOFs images by using iDPC-STEM. a, MIL-101. b, UiO-66. c, ZSM-5. d, SAPO-34. Scale bars: 1 nm (a,d), 3 nm (b,c) <sup>110</sup> . ....	23
Figure 25. History of electron microscopy. The images are reproduced from Ref. <sup>113</sup> , <sup>114</sup> , <sup>115</sup> , <sup>116,117</sup> , <sup>118,119</sup> , <sup>120</sup> , <sup>121</sup> , <sup>122</sup> , <sup>123</sup> , and <sup>124,125</sup> for timeline 1-10, respectively (top to bottom and left to right (if there are two images in the same row)). ....	25
Figure 26. The evolution of spatial resolution in microscopy. This image is reproduced from the lecture video of David A. Muller <sup>145</sup> . ....	27
Figure 27. Schematic diagram of mass-thickness contrast in BF image. The left part represents lower atomic number or thinner specimen, and the right part represents higher atomic number or thicker specimen. This figure is reproduced from Ref. <sup>147</sup> . ....	29
Figure 28. Schematic diagram of BF and DF imaging. This figure is reproduced from Ref. <sup>147</sup> . ....	30
Figure 29. Contrast transfer function with different coefficient of $-(C_s\lambda_e)^{1/2}$ under 300 keV accelerating voltage, $\alpha = 0.1$ mrad, and $C_s = 1$ mm. ....	33



Figure 30. The impact of spherical aberration on contrast transfer function under Scherzer defocus. ....	34
Figure 31. Scheme of the imaging contrast of HRABF caused by channeling effect. This image is reproduced from Ref. <sup>151</sup> .....	36
Figure 32. The scheme of reciprocity theorem between Conventional TEM and STEM for zero-loss images. ....	36
Figure 33. Typical CTF of TEM and STEM under similar conditions. This illustrate is reproduced from Ref. <sup>153</sup> .....	38
Figure 34. Examples of channeling effect in STEM. a, Simulations of Cs-corrected ADF-STEM images of a 110 Silicon with 758 Å thick contains a single Bi atom: no Bi, a Bi atom at depth = 20 Å, 342 Å, and 750 Å <sup>155</sup> . b, ADF-STEM image of Si along 211 with corresponding FFT image <sup>156</sup> .....	39
Figure 35. The channeling effect affected electron probe coupling. a-d, Multislice approach of the probability of propagation of an electron probe in different depth (a) in free space, (b) along a single isolated atomic column, (c) along two atomic columns, and (d) along two atomic columns with a full lattice. e, Same condition of (d) but using analytic tight-binding approach. f,g, The coupling amplitudes of the antibonding and bonding states at (f) 0 Å defocus, and (g) 120 Å defocus <sup>156</sup> .....	39
Figure 36. The simulated image contrast of single atoms from Z = 1-103 for BF-, ADF-, and iDPC-STEM <sup>157</sup> .....	41
Figure 37. Schematics of the determination of COM. a,b, the incident beam interacts (a) without specimen potential and (b) with specimen potential .....	41
Figure 38. Signals generated by the interactions between a high-energy electron beam with a thin specimen .....	44



Figure 39. Schematics of EDS. a, A conventional EDS. b, Latest model of the four silicon drift detectors. b is reproduced from Ref. <sup>165</sup> . .....	44
Figure 40. Schematic of electron energy loss spectroscopy with beam propagations. ....	45
Figure 41. Schematics of EELS. a, The region of low loss and high loss region, including the zero loss peak and plasmon peaks. b, A typical core loss peaks for boron nitride (BN). c, An example energy band diagram of BN with the contributions of different excitation to the spectra in (a,b), including plasmon, energy loss near edge structure (ELNES), and extended energy loss fine structure (EXELFS). The scale of energy in (c) is non-linear. ....	46
Figure 42. FIB procedure of a practice. a, Locating specimen. b, Deposition of protective layer. c, Digging two big holes by Ga ion beam. d, Leaving a handle on a side. e, Transferring the specimen to half grid. f, The low magnification image of the cross-section specimen. ....	49
Figure 43. CVD Synthesis of 2D ReSe <sub>2</sub> . a, Atomic models for 2D ReSe <sub>2</sub> , <i>a</i> and <i>b</i> crystal directions are highlighted, <i>a</i> is along Re diamond chain direction. Re atom (blue), Se atom (yellow). b, Scheme of split-zone CVD growth. c,d, Optical images (non-polarized and polarized) for as grown monolayer 2D ReSe <sub>2</sub> flake, showing anisotropic stripe patterns. Scale bars = 10 μm. e, TEM HAADF image for as grown 2D ReSe <sub>2</sub> . Different grains are false colored for contrast enhancement. Red arrows mark the cluster aggregates. White arrows mark the <i>a</i> direction for each grain. Scale bar = 10 nm.....	58
Figure 44. Crystal structures of (a) single layer ReSe <sub>2</sub> (top and side views) and (b) Re <sub>6</sub> Se <sub>8</sub> clusters. Re <sub>4</sub> rhenium chain is illustrated in red dashed lines <sup>208,209</sup> .....	58
Figure 45. (a-c), (d-f), (g-i), (j-l) and (m-o) show bright field, 70° and 110° polarized light optical microscopic images of ReSe <sub>2</sub> grown with 1, 2, 3, 4 and 5 sccm H <sub>2</sub> . ReSe <sub>2</sub> subdomains have the sharpest contrast difference when the polarization angle of light is	



70° and 110°. As the H <sub>2</sub> flow rate increased, the shapes kept as triangular with zigzag edges. Scale bars =10 μm.....	59
Figure 46. Atomic force microscopy images and profiles of 1L-ReSe <sub>2</sub> grown with 1-5 sccm H <sub>2</sub> . (a-c), (d-f), (g-i), (j-l), (m-o) show topographic images of 1-5 sccm H <sub>2</sub> grown ReSe <sub>2</sub> , tiny clusters sized 60 nm in diameter can be observed in all the samples. The surface roughness (R) decreased significantly from 1-3 sccm H <sub>2</sub> conditions (R~1 nm) to 4 sccm, (R~0.6 nm) and 5 sccm (R~0.5 nm) H <sub>2</sub> growth conditions. Scale bars = 10 μm (a,b,d,e,g,h,j,k,m,n), 50 nm (c,f,i,l,o). p, Height profiles of 1-5 sccm H <sub>2</sub> ReSe <sub>2</sub> single layers, corresponding to images (a,d,g,j,m). q, Height profiles of Re <sub>6</sub> Se <sub>8</sub> clusters on 1-5 sccm H <sub>2</sub> ReSe <sub>2</sub> , corresponding to images (c,f,i,l,o). The height of ReSe <sub>2</sub> flakes stayed the same and that of clusters remained similar as the H <sub>2</sub> flow rate changed from 1 sccm to 5 sccm.....	60
Figure 47. PL spectroscopy of 1L-ReSe <sub>2</sub> grown with 1-5 sccm H <sub>2</sub> and transferred on suspended positions on TEM grid. The PL of 2 sccm H <sub>2</sub> ReSe <sub>2</sub> showed a 0.01 eV blueshifts compared with 1 sccm and 3 sccm H <sub>2</sub> ReSe <sub>2</sub> . The PL of 4 sccm and 5 sccm H <sub>2</sub> ReSe <sub>2</sub> showed a 0.01 eV and 0.02 eV redshifts compared with 1 sccm and 3 sccm H <sub>2</sub> ReSe <sub>2</sub> , which may also result from higher strains in the sample caused by more uniform morphology of flakes <sup>211</sup> . .....	60
Figure 48. Polarization angle-resolved Raman spectroscopy of ReSe <sub>2</sub> grown with 1, 2 and 3 sccm H <sub>2</sub> . a-c, show polarized 0° and 70° Raman spectroscopy, descending in Raman intensity of most peaks between 100-300 cm <sup>-1</sup> . Raman single spectrum of 1, 2 and 3 sccm H <sub>2</sub> ReSe <sub>2</sub> show that the Raman intensity of 121 cm <sup>-1</sup> E <sub>g</sub> -like mode decreased at 2 sccm and 3 sccm H <sub>2</sub> ReSe <sub>2</sub> , which can be explained by the hindering of in-plane E <sub>g</sub> -like vibration caused by remaining strain at the flake-substrate interfaces, caused by better uniformity and reduced cluster aggregates by higher H <sub>2</sub> flow.....	61



Figure 49. STEM characterizations of  $\text{Re}_6\text{Se}_8$  clusters. a,b,  $\text{Re}_6\text{Se}_8$  cluster aggregates residing in holes of mono- and bi-layer  $\text{ReSe}_2$ . Scale bars = 2 nm. c-e, STEM-HAADF images, DFT derived atomic models and STEM image simulations of  $\text{Re}_6\text{Se}_8$  clusters in different orientations. f, STEM image, DFT derived atomic model and STEM image simulations for two  $\text{Re}_6\text{Se}_8$  clusters attached to the edge of 2D  $\text{ReSe}_2$ . Scale bar = 0.5 nm. g EELS results (background subtracted) for  $\text{Re}_6\text{Se}_8$  cluster aggregates, EELS quantification consistently gives higher Re/Se ratio in clusters than in 2D  $\text{ReSe}_2$  layers. .... 62

Figure 50. Electron energy loss spectroscopy (EELS) spectra of  $\text{Re}_6\text{Se}_8$  clusters. (a-i) show HRTEM image and EELS spectra of 1L  $\text{ReSe}_2$  and  $\text{Re}_6\text{Se}_8$  clusters on 1, 2, and 3 sccm  $\text{H}_2$  grown  $\text{ReSe}_2$ . (a-c) 1 sccm  $\text{H}_2$ , (d-f) 2 sccm  $\text{H}_2$ , (g-i) 3 sccm  $\text{H}_2$  conditions. (b,e,h) show the original EELS spectra and (c,f,i) show the signals after background subtraction. The peaks of 46 eV and 57 eV in (b, c, e, f, h, i) correspond to  $\text{Re O}_3$  and  $\text{Re O}_2$  with Se  $\text{M}_{4,5}$  peaks, respectively. Scale bar = 2 nm. Red dash boxes indicate the corresponding scanning areas of EELS acquisition. .... 62

Figure 51. STEM images of 2D  $\text{ReSe}_2$  product grown with 1, 2 and 3 sccm  $\text{H}_2$  condition. Tiny clusters are shown in all (a-c) 1 sccm  $\text{H}_2$   $\text{ReSe}_2$ , (d-f) 2 sccm  $\text{H}_2$   $\text{ReSe}_2$ , (g-i) 3 sccm  $\text{H}_2$ . The 3 sccm  $\text{H}_2$  sample contains significantly less cluster aggregates than 1 and 2 sccm growth conditions. Scale bar = (a,d,g) 200 nm, (b,e,h) 5 nm, (c,f,i) 2 nm. .... 63

Figure 52. STEM images for  $\text{Re}_6\text{Se}_8$  clusters on surfaces and edges of as-grown 2D  $\text{ReSe}_2$  flakes. Each dotted like bright spot corresponds to a single  $\text{Re}_6\text{Se}_8$  molecular cluster. Scale bars in (a-m) = 1 nm, scale bars in (n-p) = 10 nm. .... 63

**Figure 53.  $\text{Re}_6\text{Se}_8$  clusters and nucleation.** a-d, STEM image, DFT derived atomic model and STEM image simulation for  $\text{Re}_6\text{Se}_8$  clusters anchored on different edges of 2D  $\text{ReSe}_2$  through Se linkage atoms. e-h, STEM image, atomic model and STEM image





simulation for $\text{Re}_6\text{Se}_8$ clusters anchored on monolayer $\text{ReSe}_2$ surfaces and crystal nuclei for epilayers of 2D $\text{ReSe}_2$ with $\text{Re}_6\text{Se}_8$ clusters attached on edges. Scale bars = 1 nm. .64	
Figure 54. Reaction energy profile for selenization process along edges of $a$ (blue) and $b$ (red) by DFT calculations. Initial and final steps involve gas phase $\text{Re}_6\text{Se}_{12}$ cluster adsorbed on different edges to 2D cluster formation. ....	65
Figure 55. Stable $\text{Re}_6\text{Se}_8$ clusters and aggregates. a, STEM image, atomic model and image simulation for cluster aggregates. Chain-like structures are highlighted by red dashed lines and boxes in STEM images. b, Stability of single $\text{Re}_6\text{Se}_8$ cluster under e beam irradiation for 52 s. Rotation of cluster (center in white dashed box) is noted, corresponding atomic models for $\text{Re}_6\text{Se}_8$ cluster of each time are embedded in lower left corners. Scale bar = 1 nm.....	68
Figure 56. Structure of metal chalcogenides and transition metal dichalcogenides along $[1210]$ and $0001$ in $P6_3/mmc$ , $R3m$ , $P6m2$ , $R3m$ , and $P3$ symmetry. The red dashed polygons show the directions of each layer in MX.....	72
Figure 57. The structural change of 2H-InSe after mechanical deformation. a, The experimental workflow. b,c, XRD result of control group (before deformation) (b), and experimental group (with deformation) (c). The light blue dashed lines highlight the differences between (b) and (c). d,e, High resolution STEM-HAADF images in zone axis of $[0001]$ and $[1210]$ of the control group (d), and the experimental group (e), showing 2H and 3R stacking, respectively. Insets in (d,e), STEM simulation images. Scale bars: 1 nm.....	79
Figure 58. Raman spectra with corresponding optical images and a table of normalized peak intensity (%). The orange crosses in the optical images indicate the laser excited position.....	80
Figure 59. Example of stacking fault of 2R phase InSe in between 3R phase InSe. ....	80



Figure 60. Atomic structures near micro-cracks along [0001]. a, InSe. b, MoS <sub>2</sub> . c, MoTe <sub>2</sub> . Scale bars: (a-c) 5 nm. d, Corresponding low magnification of (c) highlighted by the red box.....	81
Figure 61. Typical low magnification STEM-HAADF images after deformation of InSe, MoS <sub>2</sub> and MoTe <sub>2</sub> .....	82
Figure 62. Cross-section HAADF-STEM images of a typical single layer (1L) micro-crack without dislocation along [1210]. Scale bars: 5 nm. The red dashed lines indicate the enlarged view, the layer stacking order is marked. ....	82
Figure 63. Cross-section HAADF-STEM images of post-deformation specimens. a,b, Phase boundaries (a) before and (b) after intralayer crack with phase transitions intermediate state 3R' phase. The white dashed boxes indicate the local 3R' InSe, the green dashed boxes model the sideview and the black dashed boxes show the corresponding projection view in (a&b). c, One micro-crack forms 1/3z edge dislocation. d, Interlayer and intralayer reconnection. Scale bars: 2 nm. ....	83
Figure 64. Strain analysis by geometric phase analysis of completely transformed 3R region, phase boundary and edge dislocation. Scale bars: 2 nm. ....	84
Figure 65. <i>In situ</i> TEM bending experiment of 2H-InSe. a-c, STEM-HAADF images (a) before, and (b,c) after <i>in situ</i> bending experiment. c, Enlarged view of red dashed box in (b). d, The line profiles of corresponding numbers in (c) for thickness estimation. e, Merged HRTEM image with respect to (b,c). An outermost fracture during <i>in situ</i> bending experiment is indicated by green dashed line (Supplementary Video 1) and a cross-layer joint of micro-cracks is highlighted by the yellow area. The yellow and red arrows track two dislocations in (a-c&e). ....	86
Figure 66. Second example of <i>in situ</i> TEM bending experiment of 2H-InSe. a,b, Another set of <i>in situ</i> bending experiment. Snapshots before (a) and after (b&c) <i>in situ</i> experiment	



with corresponding HRTEM image (c) indicated by red dashed box in (b). A pair of yellow dashed lines indicate the original position of the edges before vertical fracture in (c). Scale bars: 200 nm (a,b) and 10 nm (c). .....	87
Figure 67. Theoretical calculations. a-c, First-principles calculations of intralayer bonding strength and 1L phase transformation barrier. -pCOHP for intralayer bonding of (a) In-Se, and (b) Mo-S. The integrated areas and the integrated bonding strengths are marked in the light blue dashed boxes in (a&b). c, 1L phase transformation energy barrier for InSe (1H-to-1R') and MoS <sub>2</sub> (1H-to-1T) with schematics of the transition of chalcogen atoms. d, LAMMPS simulations of two steps phase transition of a 3L model for InSe (2H-to-3R'-to-3R) and MoS <sub>2</sub> (2H-to-1T-to-3R). .....	88
Figure 68. Relative gliding energy by molecular dynamics from LAMMPS. a-f, Relative gliding energy per atom of (a) MX, (b) MoX <sub>2</sub> and (c) WX <sub>2</sub> along 1010, and that of (d) MX, (e) MoX <sub>2</sub> and (f) WX <sub>2</sub> along 1210. Barrier values in (a-f) can be seen in Table 3. ....	90
Figure 69. Optical images and a table of estimated strain before and after compression and shear force. The measured peak force of compression is 2.45 N and the peak normal shear force is 3.63 N. The strain rate is ~0.5/s. ....	92
Figure 70. Schematic diagram of the mechanism of ultra-plasticity. ....	94
Figure 71. Modeling Ni-BDC by direct observations. a-c, <b>Ni-BDC images along zone axis [010]. A, ADF-STEM image. b, iDPC-STEM image. c, Contrast inverted dDPC-STEM. D, iDPC-STEM image along [001]. Scale bars: 2 nm. Insets, red boxes in (a-c) indicate the simulated images, and the orange dashed boxes in (a-d) show the enlarged the view of a benzene ring. The white dashed boxes in (a-c) demonstrate O-H on the Ni-O chain. E, Similar model of Ni-BDC from CCDC: 985792<sup>266</sup>. F, Edited crystal structure suggested by direct observation along [010] and [001].....</b>	100



Figure 72. Spatial resolution by using corresponding FFT in Figure 71b. ....	100
Figure 73. iDPC- and dDPC-STEM in Ni-BDC <sub>9</sub> ATA. Scale bars: 2 Å. White dashed circles highlighted the amino acid.....	101
Figure 74. GPA of the full field of view of Figure 73. Orange box highlighted the corresponding position of Figure 73. ....	102
Figure 75. Other amino acids examples acquired by iDPC- and dDPC-STEM. Field of views: 1.775 nm × 1.389 nm. ....	102
Figure 76. Notation of the orientation of the ATA ligands with example. Yellow atoms show the equivalent position under the same notation.....	103
Figure 77. Notation of O1 and O4 showing different Ni coordination.....	103
Figure 78. Line profiles extraction from the charge density map in experiment, Dr. Probe and VASP. Black, orange, and green arrows demonstrate how the line profiles are extracted for C-H, N-H, and O-H, respectively. ....	104
Figure 79. Box charts of the charge density, atomic distance, and charge density ratio. a, The charge density of C, N, or O. b, The charge density of H. c, The projected distance to H. d, The charge density ratio of C, N or O divided by H. ....	105



# List of Tables

Table 1. Wavelengths of electrons at commonly used accelerating voltages .....	28
Table 2. Exfoliation energy and formation energy .....	84
Table 3. Gliding barrier along <b>1010</b> and <b>1210</b> directions .....	90
Table 4. DFT calculated elastic constants ( $C_{ij}$ ), bulk modulus (B), shear modulus (G), Young's modulus (E), Poisson ratio ( $\nu$ ), Vickers hardness (Hv), and Anisotropy index ( $A^L$ ) of 3R-InSe, 2H-InSe, and 2H-MoS <sub>2</sub> . ....	92
Table 5. Table of counts and relaxed energy of different ATA orientation.....	103



# List of Publications

1. **Lok Wing Wong**, Dengrong Sun, Hok Yin Wong, Qingming Deng\*, and Jiong Zhao\*, “Quantitative dDPC-STEM for MOFs imaging and lower energy site prediction”, Preparing manuscript for **Nature Communications**.
2. **Lok Wing Wong**, Ke Yang, Wei Han, Xiaodong Zheng, Hok Yin Wong, Chi Shing Ben Tsang, Chun-Sing Lee, Shu Ping Lau, Thuc Hue Ly\*, Ming Yang\*, and Jiong Zhao\*, “On the Ultra-Plasticity in van der Waals Layered Materials”, Preparing manuscript for **Nature Materials**.
3. Haijun Liu<sup>#</sup>, Quoc Huy Thi<sup>#</sup>, Ping Man, Xin Chen, Tianren Chen, **Lok Wing Wong**, Shan Jiang, Lingli Huang, Tiefeng Yang, Ka Ho Leung, Tsz Tung Leung, Shan Gao, Honglin Chen, Chun-Sing Lee, Min Kan, Jiong Zhao\*, Qingming Deng\*, & Thuc Hue Ly\*, “Controlled Adhesion of Ice-Toward Ultraclean 2D Materials”, **Advanced Materials**, 2023, 2210503.
4. Wei Han, Xiaodong Zheng, Ke Yang, Chi Shing Tsang, Fangyuan Zheng, **Lok Wing Wong**, Ka Hei Lai, Tiefeng Yang, Qi Wei, Mingjie Li, Weng Fu Io, Feng Guo, Yuan Cai, Ning Wang, Jianhua Hao, Shu Ping Lau, Chun-Sing Lee, Thuc Hue Ly\*, Ming Yang\*, and Jiong Zhao\*, “Phase-controllable large-area two-dimensional In<sub>2</sub>Se<sub>3</sub> and ferroelectric hetero-phase junction”, **Nature Nanotechnology**, 2022, 18, 55-63.
5. Dengrong Sun, **Lok Wing Wong**, Hok Yin Wong, Ka Hei Lai, Lin Ye, Xinyao Xv, Thuc Hue Ly\*, Qingming Deng\*, and Jiong Zhao\*, “Direct Visualization of Atomic Structure in Multivariate MOFs for Guiding Electrocatalysts Design”, **Angewandte Chemie**, 2022, 62, 4, e202216008.
6. Sin-Yi Pang<sup>#</sup>, Weng-Fu Io<sup>#</sup>, **Lok-Wing Wong**, Jiong Zhao, and Jianhua Hao\*, “Direct and *in situ* growth of 1T' MoS<sub>2</sub> and 1T MoSe<sub>2</sub> on electrochemically synthesized MXene as an electrocatalyst for hydrogen generation”, **Nano Energy**, 2022, 103, 107835.
7. Ran Ding, Yongxin Lyu, Yuqian Zhao, Zehan Wu, Feng Guo, Weng Fu Io, Sin-Yi Pang, Jianfeng Mao, Man-Chung Wong, **Lok Wing Wong**, Cenqi Yan, Jiangsheng



- Yu, Jiong Zhao, Gang Li, and Jianhua Hao\*, “Revealing photovoltaic behavior in 2D hybrid perovskite ferroelectric single-crystalline microwire arrays for self-powered photodetectors”, **Materials Today Physics**, 2022, 28, 100867.
8. Xiaodong Zheng<sup>#</sup>, Wei Han<sup>#</sup>, Ke Yang<sup>#</sup>, **Lok Wing Wong**, Chi Shing Tsang, Ka Hei Lai, Fangyuan Zheng, Tiefeng Yang, Shu Ping Lau, Thuc Hue Ly\*, Ming Yang\*, and Jiong Zhao\*, “Phase and polarization modulation in two-dimensional In<sub>2</sub>Se<sub>3</sub> via in situ transmission electron microscopy”, **Science advances**, 2022, 8, 42, eabo0773.
9. Haiyan Jin<sup>#</sup>, **Lok Wing Wong**<sup>#</sup>, Ka Hei Lai, Xiaodong Zheng, Shu Ping Lau\*, Qingming Deng\*, and Jiong Zhao\*, “N-stabilized metal single atoms enabled rich defects for noble-metal alloy toward superior water reduction”, **EcoMat**, 2022, 5, 1, e12267.
10. Chun-Ki Liu<sup>#</sup>, Venkatesh Piradi<sup>#</sup>, Jiajun Song, Ziru Wang, **Lok-Wing Wong**, Eng-Hao-Louis Tan, Jiong Zhao, Xunjin Zhu\*, and Feng Yan\*, “2D Metal–Organic Framework Cu<sub>3</sub>(HHTT)<sub>2</sub> Films for Broadband Photodetectors from Ultraviolet to Mid-Infrared”, **Advanced Materials**, 2022, 34, 32, 2204140.
11. Fangyuan Zheng<sup>#</sup>, Deping Guo<sup>#</sup>, Lingli Huang<sup>#</sup>, **Lok Wing Wong**<sup>#</sup>, Xin Chen, Cong Wang, Yuan Cai, Ning Wang, Chun-Sing Lee, Shu Ping Lau, Thuc Hue Ly\*, Wei Ji\*, and Jiong Zhao\*, “Sub-Nanometer Electron Beam Phase Patterning in 2D Materials”, **Advanced Science**, 2022, 9, 23, 2200702.
12. Tsz-Lung Ho, Keda Ding, Nikolay Lyapunov, Chun-Hung Suen, **Lok-Wing Wong**, Jiong Zhao, Ming Yang, Xiaoyuan Zhou, and Ji-Yan Dai\*, “Multi-Level Resistive Switching in SnSe/SrTiO<sub>3</sub> Heterostructure Based Memristor Device”, **Nanomaterials**, 2022, 12, 13, 2128.
13. Congying Xiang, Min Shen, Chongze Hu, **Lok Wing Wong**, Hongbo Nie, Huasheng Lei, Jian Luo, Jiong Zhao\*, and Zhiyang Yu\*, “Atomistic observation of in situ fractured surfaces at a V-doped WC Co interface”, **Journal of Materials Science & Technology**, 2022, 110, 103-108.
14. Ping Kwong Cheng, Safayet Ahmed, Junpeng Qiao, **Lok Wing Wong**, Chun Fai Yuen, Ahmed Mortuza Saleque, Md. Nahian Al Subrilvan, Sumaiya Umme Hani, Mohammad, Ismail Hossain, Jiong Zhao, Qiao Wen, and Yuen Hong Tsang\*,



- “Nonlinear optical properties of two-dimensional palladium ditelluride (PdTe<sub>2</sub>) and its application as aerosol jet printed saturable absorbers for broadband ultrafast photonics”, **Applied Materials Today**, 2022, 26, 101296.
15. Huaping Jia, Zhiyong Li, Bingzhe Wang, Guichuan Xing, Yat Lam Wong, Hui Ren, Mingjie Li, Kwok-Yin Wong, Danyuan Lei, **Lok-Wing Wong**, Jiong Zhao, Wendong Zhang, Shengbo Sang\*, Aoqun Jian\*, and Xuming Zhang\*, “Plasmonic Nanohole Arrays with Enhanced Visible Light Photoelectrocatalytic Activity”, **ACS Photonics**, 2022, 9, 2, 652-663.
16. Xin Chen<sup>#</sup>, **Lok-Wing Wong**<sup>#</sup>, Lingli Huang, Fangyuan Zheng, Ran Huang, Shu Ping Lau, Chun-Sing Lee, Jiong Zhao\*, Qingming Deng\*, and Thuc Hue Ly\*, “Unveiling the Critical Intermediate Stages During Chemical Vapor Deposition of Two-Dimensional Rhenium Diselenide”, **Chemistry of Materials**, 2021, 33, 17, 7039-7046.
17. Lingli Huang, Tiefeng Yang, **Lok Wing Wong**, Fangyuan Zheng, Xin Chen, Ka Hei Lai, Haijun Liu, Quoc Huy Thi, Dong Shen, Chun-Sing Lee, Qingming Deng\*, Jiong Zhao\*, and Thuc Hue Ly\*, “Redox photochemistry on van der Waals surfaces for reversible doping in 2D materials”, **Advanced Functional Materials**, 2021, 31, 2009166.
18. Lingli Huang<sup>#</sup>, Fangyuan Zheng<sup>#</sup>, Qingming Deng<sup>#</sup>, Quoc Huy Thi<sup>#</sup>, **Lok Wing Wong**, Yuan Cai, Ning Wang, Chun-Sing Lee, Shu Ping Lau, Manish Chhowalla, Ju Li, Thuc Hue Ly\*, and Jiong Zhao\*, “In situ scanning transmission electron microscopy observations of fracture at the atomic scale”, **Physical Review Letters**, 2020, 125, 246102.
19. Lingli Huang<sup>#</sup>, Fangyuan Zheng<sup>#</sup>, Qingming Deng<sup>#</sup>, Quoc Huy Thi<sup>#</sup>, **Lok Wing Wong**, Yuan Cai, Ning Wang, Chun-Sing Lee, Shu Ping Lau, Thuc Hue Ly\*, and Jiong Zhao\*, “Anomalous fracture in two-dimensional rhenium disulfide”, **Science advances**, 2020, 6, 47, eabc2282.
20. Fangyuan Zheng, **Lok Wing Wong**, Jiong Zhao, and Thuc Hue Ly, “A Novel Class of Two-Dimensional Materials: Transition Metal Dichalcogenides”, **21st Century Nanoscience—A Handbook**, 2020, 4, 6-1-6-25.





21. Fangyuan Zheng, Lingli Huang, **Lok-Wing Wong**, Jin Han, Yuan Cai, Ning Wang, Qingming Deng\*, Thuc Hue Ly\*, and Jiong Zhao\*, “The Mobile and Pinned Grain Boundaries in 2D Monoclinic Rhenium Disulfide”. **Advanced Science**, 2020, 7, 22, 2001742.
22. Quoc Huy Thi<sup>#</sup>, **Lok Wing Wong**<sup>#</sup>, Haijun Liu, Chun-Sing Lee, Jiong Zhao\*, and Thuc Hue Ly\*, “Spontaneously ordered hierarchical two-dimensional wrinkle patterns in two-dimensional materials”, **Nano Letters**, 2020, 20, 11, 8420–8425.
23. **Lok-Wing Wong**, Lingli Huang, Fangyuan Zheng, Quoc Huy Thi, Jiong Zhao\*, Qingming Deng\*, and Thuc Hue Ly\*, “Site-specific electrical contacts with the two-dimensional materials”, **Nature communications**, 2020, 11, 1, 1-10.
24. Weng Fu Io, Shuoguo Yuan, Sin Yi Pang, **Lok Wing Wong**, Jiong Zhao, and Jianhua Hao\*, “Temperature-and thickness-dependence of robust out-of-plane ferroelectricity in CVD grown ultrathin van der Waals  $\alpha$ -In<sub>2</sub>Se<sub>3</sub> layers”. **Nano research**, 2020, 13, 7, 1897-1902.
25. Fangyuan Zheng, Wai Chung Lam, Ka Hei Lai, Lingli Huang, **Lok Wing Wong**, Yisong Zhang, Zhangyuan Yan, Chak Chung Sham, Quoc Huy Thi, Thuc Hue Ly\*, and Jiong Zhao\*, “Synchronized Structure and Surface Tension Measurement on Individual Secondary Aerosol Particles by Low-Voltage Transmission Electron Microscopy”, **Environmental Science & Technology Letters**, 2020, 7, 8, 560–566.
26. Sin-Yi Pang, Weng-Fu Io, **Lok-Wing Wong**, Jiong Zhao, and Jianhua Hao\*, “Efficient energy conversion and storage based on robust fluoride-free self-assembled 1D niobium carbide in 3D nanowire network”, **Advanced Science**, 2020, 7, 10, 1903680.
27. Ran Ding, Chun-Ki Liu, Zehan Wu, Feng Guo, Sin-Yi Pang, **Lok Wing Wong**, Weng Fu Io, Shuoguo Yuan, Man-Chung Wong, Michal Bartłomiej Jedrzejczyk, Jiong Zhao, Feng Yan, and Jianhua Hao\*. “A general wet transferring approach for diffusion-facilitated space-confined grown perovskite single-crystalline optoelectronic thin films”, **Nano Letters**, 2020, 20, 4, 2747–2755.
28. Fangyuan Zheng<sup>#</sup>, Quoc Huy Thi<sup>#</sup>, **Lok Wing Wong**, Qingming Deng\*, Thuc Hue



Ly\*, and Jiong Zhao\*, “Critical stable length in wrinkles of two-dimensional materials”, **ACS Nano**, 2020, 14, 2, 2137–2144.

# Co-first author

\* Corresponding author



# List of Abbreviations

0D	Zero-dimensional
2D	Two-dimensional
4D	Four-dimensional
$\alpha$	Convergence semi-angle
$\beta$	Collection semi-angle
ABF	Annular bright field
ABSF	Average background subtracting filtering
ACTEM	Aberration corrected transmission electron microscope
ADF	Annular dark field
AFM	Atomic force microscopy
APCVD	Atmospheric pressure chemical vapor deposition
ATA	2-amino-terephthalate
B	Bulk modulus
BDC	Benzene-dicarboxylate
BF	Bright field
CBED	Convergent beam electron diffraction
CCD	Charge-coupled device
CNT	Carbon nanotube
COHP	Crystal orbital Hamiltonian populations
COM	Center of mass
CP	Cauchy pressure
Cs	Spherical aberration
CTF	Contrast transfer function
CVD	Chemical vapor deposition
dDPC	Differentiated differential phase contrast
DF	Dark field
DFT	Density functional theory
DMF	Dimethylformamide
DPC	Differential phase contrast



E	Young's modulus
EDS	Energy-dispersive X-ray spectroscopy
EDX	Characteristic X-ray
EELS	Electron energy loss spectroscopy
ELF	Electron localization function
ELNES	Energy loss near edge structure
EM	Electron microscopy
EMPAD	Electron microscope pixel array detector
EXELFS	Extended energy loss fine structure
FEG	Field emission gun
FIB	Focused ion beam
FM	Frank-van der Merwe
FWHM	Full width half maximum
G	Shear modulus
GGA	Generalized gradient approximation
GPA	Geometric phase analysis
HAADF	High-angle annular dark field
HER	Hydrogen evolution reaction
HR	High-resolution
HRTEM	High-resolution transmission electron microscopy
Hv	Vickers hardness
iDPC	Integrated differential phase contrast
LAMMPS	Large-scale atomic/molecular massively parallel simulator
LDMs	Low-dimensional materials
LPCVD	Low-pressure chemical vapor deposition
MBE	Molecular beam epitaxy
MD	Molecular dynamics
MFP	Mean free path
MOCVD	Metal-organic chemical vapor deposition
MOFs	Metal-organic frameworks
N.A.	Numerical aperture
OER	Oxygen evolution reaction



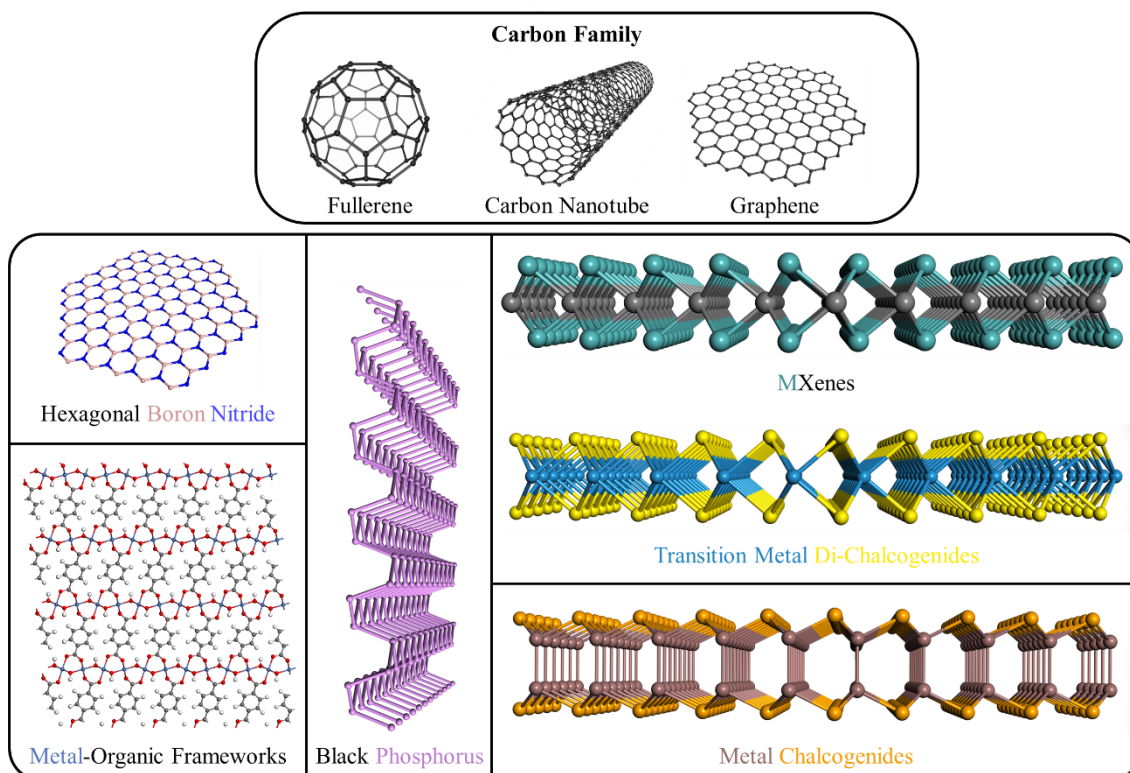
PAW	Projector augmented wave
PBE	Perdew-Burke-Ernzerhof
PMMA	Poly(methyl methacrylate)
PL	Photoluminescence
POA	Phase-object approximation
PR	Pugh's ratio
RT	Room temperature
SEM	Scanning electron microscopy
SNR	Signal-to-noise ratio
STEM	Scanning transmission electron microscopy
STM	Scanning tunnelling microscopy
TEM	Transmission electron microscopy
MCs	Metal chalcogenides
TMDCs	Transition metal dichalcogenides
VASP	Vienna ab initio Simulation Package
vdW	van der Waals
WPO	Weak phase-object
WPOA	Weak phase-object approximation
XPS	X-ray photoelectron spectroscopy
XRD	X-ray diffraction
Z	Atomic number



## Chapter 1. Introduction

In this thesis, aberration corrected transmission electron microscope (ACTEM) is mainly used to investigate the structure-property relationships. Studying TEM and its techniques is beneficial to explore the atomic structure of the specimens, especially for the emerging low-dimensional materials (LDMs) with excellent mechanical and chemical properties for future applications. Carbon is not only the most common element, but also the start of LDMs from zero-dimensional (0D) dots to two-dimensional (2D) sheet, including fullerene<sup>1,2</sup>, carbon nanotube (CNT)<sup>3-6</sup>, and graphene<sup>6-9</sup>. Their structures and properties can be discovered by using TEM.

The extraordinary mechanical and electrical properties of them provide abundant potential applications. Taking graphene as an example, graphene has the highest thermal conductivity at room temperature (RT) ( $3000 \text{ to } 5000 \text{ Wm}^{-1}\text{K}^{-1}$ )<sup>10</sup>, excellent Young's modulus ( $1.0 \pm 0.1 \text{ TPa}$ )<sup>11</sup>, distinguished carrier mobilities ( $\sim 2 \times 10^5 \text{ cm}^2\text{V}^{-1}\text{s}^{-1}$  at electron densities =  $2 \times 10^{11} \text{ cm}^{-2}$  at  $5 \text{ K}$ <sup>12</sup> &  $\sim 4 \times 10^4 \text{ cm}^2\text{V}^{-1}\text{s}^{-1}$  at electron densities =  $10^{12} \text{ cm}^{-2}$  at RT<sup>13</sup>), and highly flexible as well as optical transparent<sup>14</sup> etc. The applications of the above LDMs are very wide, including medications<sup>15-19</sup>, catalysis<sup>20-26</sup>, photovoltaic<sup>27-29</sup>, energy storage<sup>30-33</sup>, field effect transistor<sup>34-36</sup>, and materials enhancement<sup>37-39</sup> etc. The smaller and better characteristics raise continuous attention on LDMs' research. Beyond the carbon family, there are numerous groups of LDMs which perform their own strengths via the works as follows, including hexagonal boron nitride (h-BN)<sup>40</sup>, black phosphorus (BP)<sup>41</sup>, transition metal dichalcogenides (TMDCs)<sup>42-47</sup>, Metal chalcogenides (MCs)<sup>48,49</sup>, metal-organic frameworks (MOFs)<sup>50,51</sup>, and MXenes<sup>52,53</sup> etc. (Figure 1).



**Figure 1. Low-dimensional materials beyond carbon family.** The categories are divided by the number of atom thickness.

Although there are tremendous investigations about LDMs, there are still plentifully valuable research questions in synthesis, materials' properties, and their accurate structure needs to be unveiled. This thesis will be divided into six chapters.

In Chapter 1, functions and applications of TEM are introduced. Taking the advantages of TEM, structure-property relationships can be resolved more directly. The important research questions are conceived by literature reviews. The experimental methods and strategies of 3 projects are introduced here. Via studying the morphologies and properties by using TEM, the projects aim to study the research questions related to fundamental physics.

In Chapter 2, the evolution, principle and applications of TEM and its technique are studied in order to conduct the experiments wisely. The correct selection of data acquisition and analytic method is a key to study structure-property relationships. The



functions of ACTEM should be maximized to avoid the waste of specimens, the expensive machine, and the valuable experimental sessions.

In Chapter 3, the first project of studying the nucleation and growth kinetics of two-dimensional (2D) transition metal dichalcogenides (TMDCs) via 2D Rhenium diselenide ( $\text{ReSe}_2$ ). Through the synthesis parameters, high-angle annular dark field (HAADF)-scanning transmission electron microscopy (STEM), and electron energy loss spectroscopy (EELS), the atomic structure of octahedral  $\text{Re}_6\text{Se}_8$  clusters have been confirmed. The clusters attach mainly near the edges of the 2D  $\text{ReSe}_2$ , followed by the surface of that. Besides, the 2D  $\text{ReSe}_2$  and the clusters can be controlled by the flow rate of hydrogen during synthesis. The data suggests two steps growth during chemical vapor deposition (CVD). Via density functional theory (DFT) calculations, the growth directions and growth kinetics of the 2D  $\text{ReSe}_2$  also supported the experimental data. This project provides insights to the controllable synthesis in terms of thickness and morphology in TMDCs.

In Chapter 4, the second project is about the exceptional plasticity of indium selenide ( $\text{InSe}$ ). Phase transition plays an important role in this plasticity, confirmed by both atomic projection and cross-section views, with comparison with other vdW materials. The gliding barrier and surface absorption enhancements by  $\beta$ -to- $\gamma$  phase transition was confirmed by the molecular dynamics (MD) simulations, and the  $\gamma'$  phase was found that acts as middle stage for this kinetic phase transition. In terms of the  $\text{MoS}_2$  and  $\text{MoTe}_2$ , phase transition is absent under the similar strain. Hence, the plasticity of  $\text{InSe}$  is better since the mechanisms of crack propagations and strain relaxation are different.





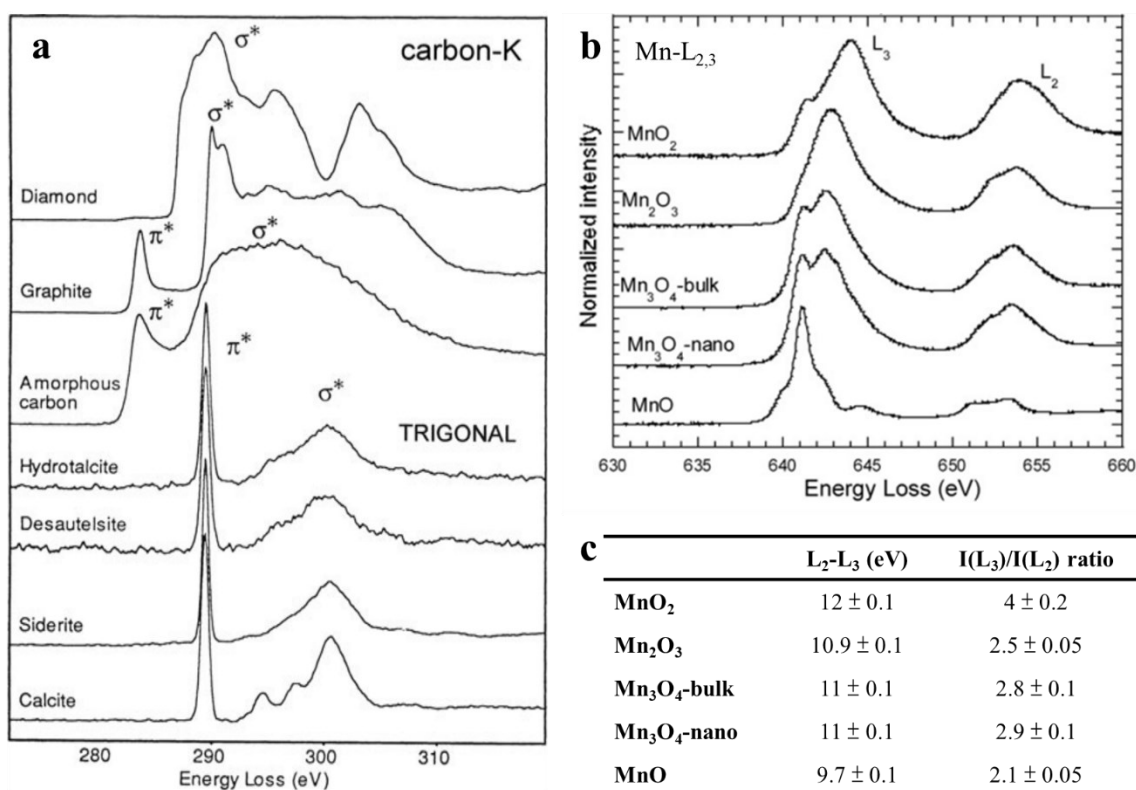
In Chapter 5, the third project aims to quantify different bonding of hydrogen, including C-H, N-H and O-H bonds via integrated differential phase contrast (iDPC)-STEM imaging technique. The further mixed ligands orientation has been successfully predicted by statistic dDPC-STEM measurements that the lower energy site has a generally high value of charge density.

In Chapter 6, the conclusion and outlook will be stated. TEM is one of the powerful tools to explore structure-property relationship in material science. By using TEM, certain research questions have been unveiled in Chapter 3 to Chapter 5. There are still tremendous unknown and interesting questions and mechanisms, that waiting scientists to explore.

### 1.1. Applications of transmission electron microscopy

Other than the well-known atomic structure imaging, EELS is a widely used to collect chemical information in LDMs, due to the higher efficiency, wider range of detectable elements, and higher SNR in light elements compared with EDS. Typical results of EELS spectra of C-K edge and Mn-L<sub>2,3</sub> are shown in Figure 2. In terms of C-K edge (Figure 2a), the fingerprints of different type of carbon and minerals containing carbon can be seen with different shape of sharp  $\pi^*$  peak and broad  $\sigma^*$  peak<sup>54</sup>. Diamond is sp<sup>3</sup> hybridization contains only  $\sigma$  bonds, that is why the spectrum of diamond has no  $\pi^*$  peak. A sharp with broad  $\pi^*$  peak of sp<sup>2</sup> hybridized graphite demonstrates it has regular  $\pi$  bonds. The continuously broadening  $\pi^*$  and  $\sigma^*$  peaks can be found in amorphous carbon. The probability of energy loss of both peaks demonstrates almost normal distribution that agrees the random nature of it. For the trigonal system, all minerals here contain CO<sub>3</sub> and the  $\pi^*$ -to- $\sigma^*$  peaks distances are the very similar. Comparing the rhombohedral siderite and octahedral calcite,  $\sigma^*$  peak is split to 3 peaks.

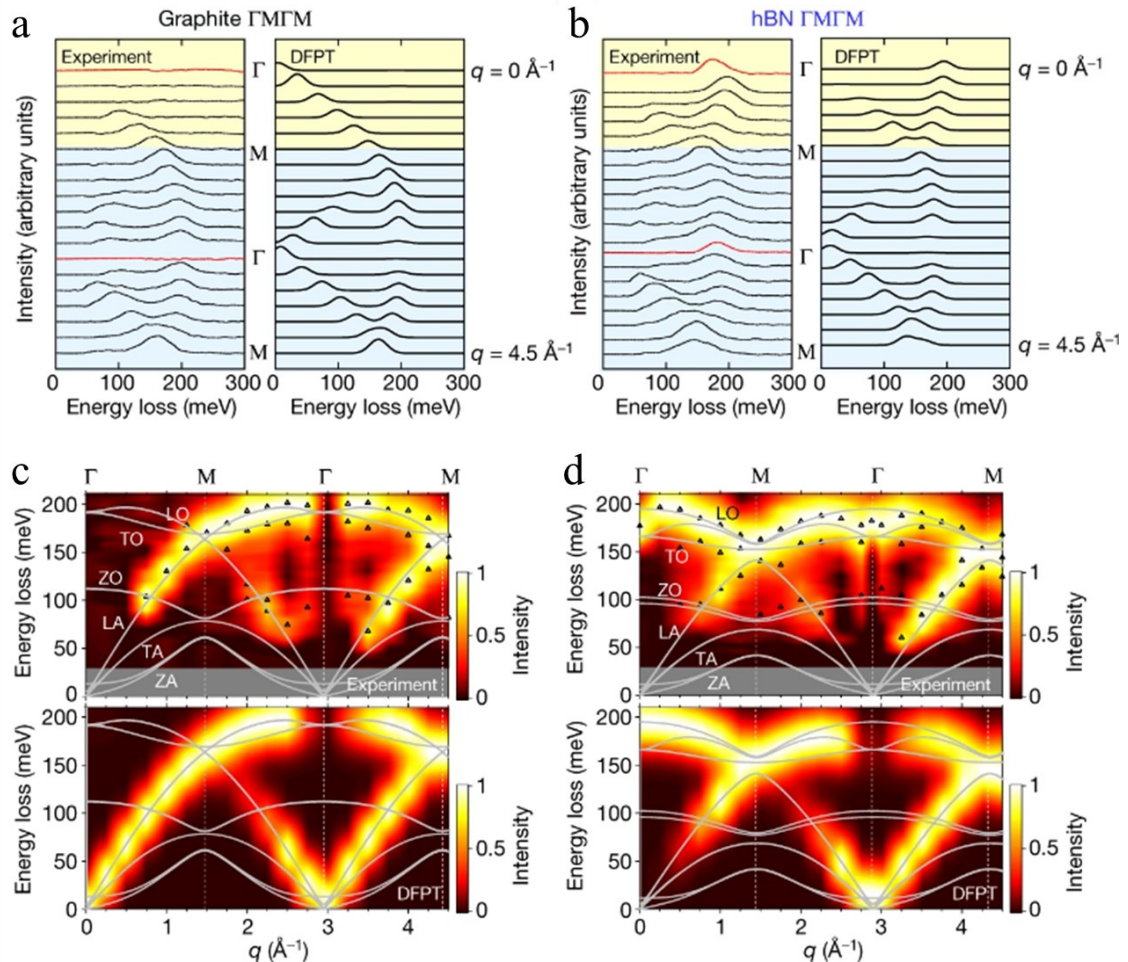
In terms of the Mn-L<sub>2,3</sub> edge (Figure 2b&c), this example demonstrates the white-line features of different valence and coordination Mn<sup>55</sup>. Their results suggest that integration L<sub>2,3</sub> peaks ratio of Mn<sup>4+</sup>, Mn<sup>3+</sup> and Mn<sup>2+</sup> is 4, 2.5, and 2.1, respectively. The L<sub>2,3</sub> peak-to-peak distance of them is 12 eV, 10.9 eV, and 9.7 eV, respectively. For the Mn<sub>3</sub>O<sub>4</sub>, this material contains both Mn<sup>3+</sup> and Mn<sup>2+</sup> ions and that is why there is a double L<sub>3</sub> peak. More EELS spectra formation can be checked and compared with the EELS atlas<sup>56</sup> and the chemical information can be analyzed.



**Figure 2. Typical background subtracted and deconvoluted EELS spectra of C-K edge and Mn-L<sub>2,3</sub> edge. a,** EELS spectra of C-K edge from different C and different minerals containing C<sup>54</sup>. **b,c, (b)** EELS spectra of different valence and coordination number of Mn with the corresponding (c) Table about L<sub>2,3</sub> peak distances and L<sub>2,3</sub> integrated peak ratio<sup>55</sup>.

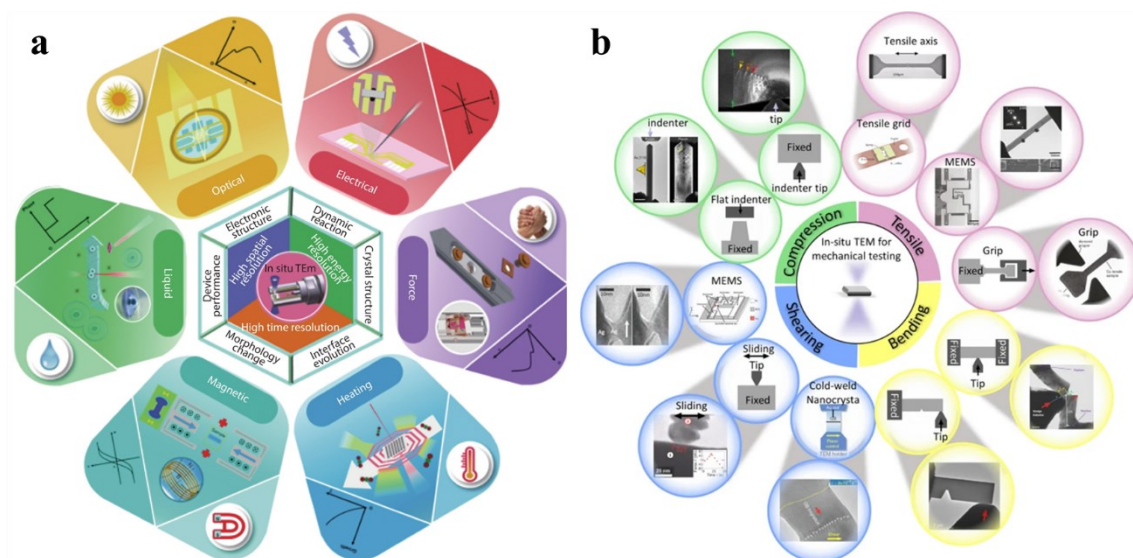
Senga *et al.* has demonstrated a phonon study on graphite and h-BN by EELS from 1<sup>st</sup> Brillion zone to 2<sup>nd</sup> Brillion zone along the  $\Gamma$ M $\Gamma$ M direction (Figure 3)<sup>57</sup>. The momentum-resolved vibrational mode conducted by EELS well matched the results of DFT simulations (Figure 3c,d). The band structure can be experimentally proved by

experiment via EELS. Although this technique is fascinating, this requires extremely stable system and high specifications of TEM, such as double monochromators, and long acquisition time (up to few days).



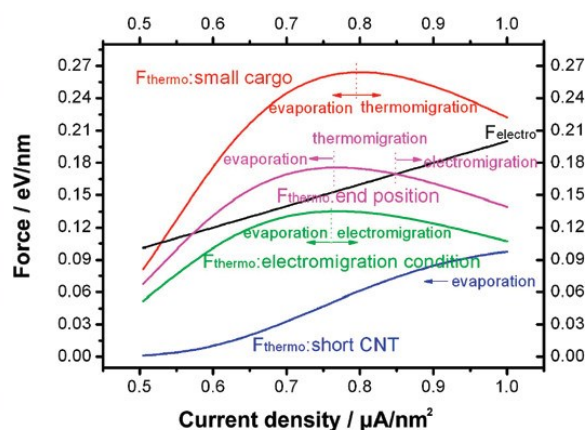
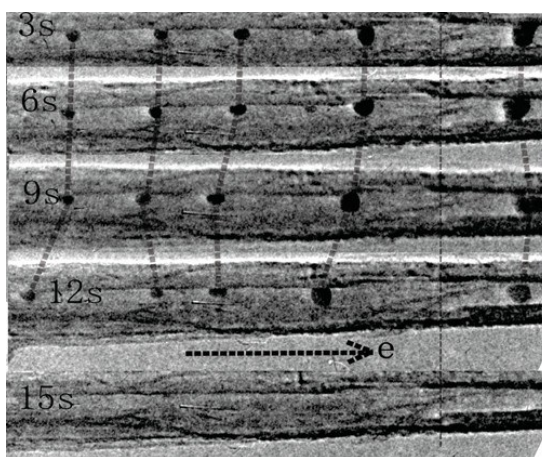
**Figure 3. Phonon dispersion of graphite and h-BN resolved by EELS spectra. a,b,** Series of phonon EELS spectra of (a) graphite, and (b) h-BN. **c,d,** Momentum intensity maps with DFT simulation results of (c) graphite, and (d) h-BN<sup>57</sup>.

Using *in situ* techniques, the process of deformations, synthesis, or catalysis etc. can be recorded and studied via direct observations in real time (Figure 4a)<sup>58</sup>. Li *et al.* has a good summary of recent *in situ* mechanical studies (Figure 4b)<sup>59</sup>. The majority mechanical studies were conducted by Gatan 654/671 straining holder, or Nanofactory<sup>TM</sup> holder. In Nanofactory<sup>TM</sup> holder, it can provide not only mechanical strain, but also electrical bias. Hence, there numerous multi-purposes holder.



**Figure 4. A summary of *in situ* TEM.** **a**, Overview of *in situ* TEM<sup>58</sup>. **b**, Recent progress of mechanical studies via *in situ* TEM. The images contribution as follows: compression<sup>60,61</sup>, tensile<sup>62-64</sup>, bending<sup>65,66</sup>, and shearing<sup>67,68</sup> were arranged by Li *et al.*<sup>59</sup>.

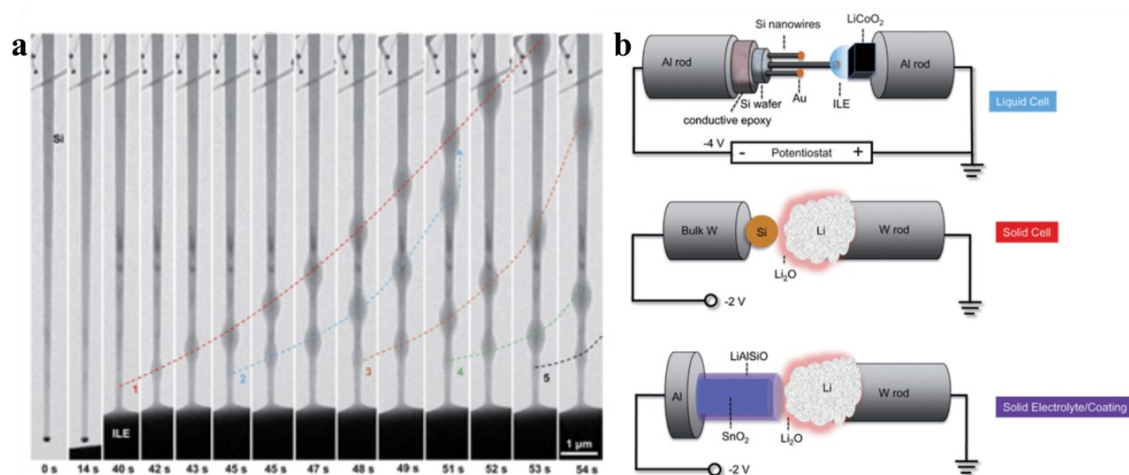
An excellent example using Nanofactory™ holder about mass transportation driven by bias inside multiwall CNT was conducted (Figure 5)<sup>69</sup>. Fe nanoparticles, and Fe rods were inside the multiwall CNT as cargos. Via the accurate piezoelectric driven probe, the W tip can apply bias to the CNT. This study differentiated there are three mass transportation mechanisms: thermal evaporation, thermo-migration and electromigration driven by thermal gradient force, and electromigration force. The cargos follow the different mechanisms under different size of cargos, current density, length of the CNT, and position of the cargos are summarized in (Figure 5).



**Figure 5. Mass transportation mechanisms by electrical bias in multiwall CNT<sup>69</sup>.**



The transport of Li ion has been also recorded by using Nanofactory™ holder (Figure 6a)<sup>70</sup>. A Si wire was attached to the Li ion liquid electrolyte/LiCoO<sub>2</sub> Without any bias, the Li ion flowed to the Si anode. Different anodes were also studied (Figure 6b).



**Figure 6. Electrochemical studies of Li ion batteries<sup>70</sup>.** **a**, Serial images of Li ion transportation cropped from a video from 0 to 54 s. **b**, Different type of anode materials.

The resolution of liquid cell *in situ* holder is suffered for a while due to a very thick silicon nitride supporting film for safe and stable liquid flow. A recent developed graphene liquid chip is shown in Figure 7a-e<sup>71</sup>. The design of double cells might provide an opportunity to study the reaction process in atomic scale. This idea was conceived by the work of Yuk *et al.*<sup>72</sup> in 2012. A graphene liquid cell scheme is shown in Figure 7f. Two graphene grids were combined that encapsulate certain liquid, and they demonstrated the possibility of atomic resolution in a liquid cell.

Differential phase contrast (DPC)-STEM can provide projected electric field and charge density information<sup>73</sup>. The projected total charge density of an interstitial unit cell of Y<sub>5</sub>Si<sub>3</sub> electride was investigated (Figure 8). In electrides, the loosely bounded electrons act as anions, localize at interstitial sites<sup>74</sup>. The anionic electron column of the electride can be identified and quantified by projected charge density map. Although the line profiles are well matched, the inhomogeneity of experimental results have been noticed,

**a**  $\Delta f = -42$  nm (c) 0 nm (d) 28 nm (e)

t-FLG (3–5 layer)  
t-hBN ( $\approx 30$  nm)  
MoS<sub>2</sub> (1–3 layer)  
b-hBN ( $\approx 30$  nm)  
b-FLG (3–5 layer)  
SiN support

**b**

**c**  $\Delta f = -42$  nm

**d**  $\Delta f = 0$

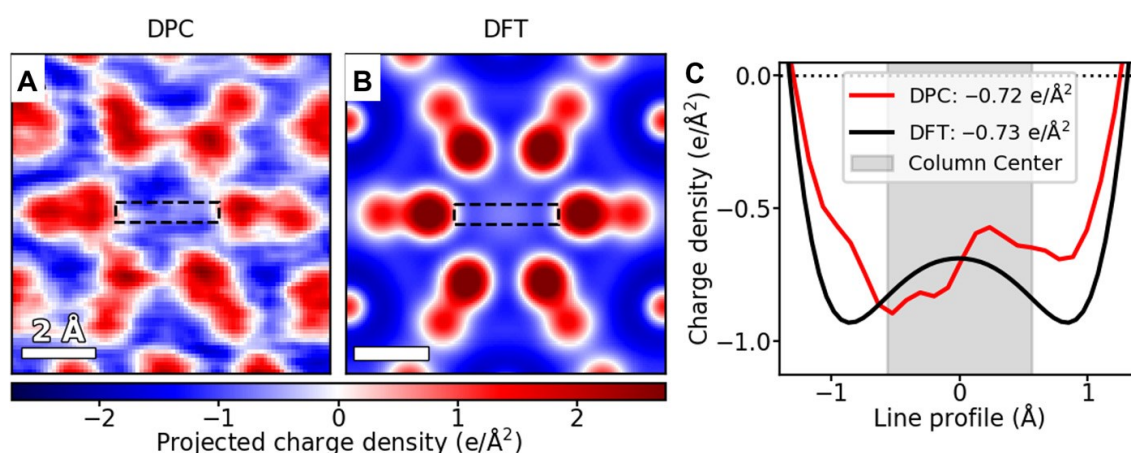
**e**  $\Delta f = 28$  nm

**f** Graphene  
Encapsulated solution

**g** 20.54 sec 24.96 sec 59.80 sec 62.4 sec 64.22 sec

$\bar{1}11$  T200  
T111 200  
T111  
Z.A. = [011]

**Figure 7. Graphene liquid cell design and performance.** **a**, Scheme of double liquid cell. **b**, A HAADF-STEM image of the homemade liquid cell. Scale bar: 2  $\mu\text{m}$ . **c-e**, HAADF-STEM images of defocus (**c**) -42 nm, (**d**) 0 nm, and (**e**) 28 nm. Scale bars: 5 nm. Images from (**a-e**) are reproduced from Ref. <sup>71</sup>. **f**, A scheme of graphene liquid cell. **g**, Serial images of Pt nanocrystal with a twin boundary under irradiation. Scale bar: 2 nm. Images from (**f,g**) are reproduced from Ref. <sup>72</sup>.



**Figure 8. Comparison between experimental and theoretical projected charge density. a, Experiment. b, DFT simulation. c, Line profile of the black dashed line in (a&b). Images (a-c) are reproduced from Ref. <sup>73</sup>.**



## 1.2. Synthesis kinetics in two-dimensional materials

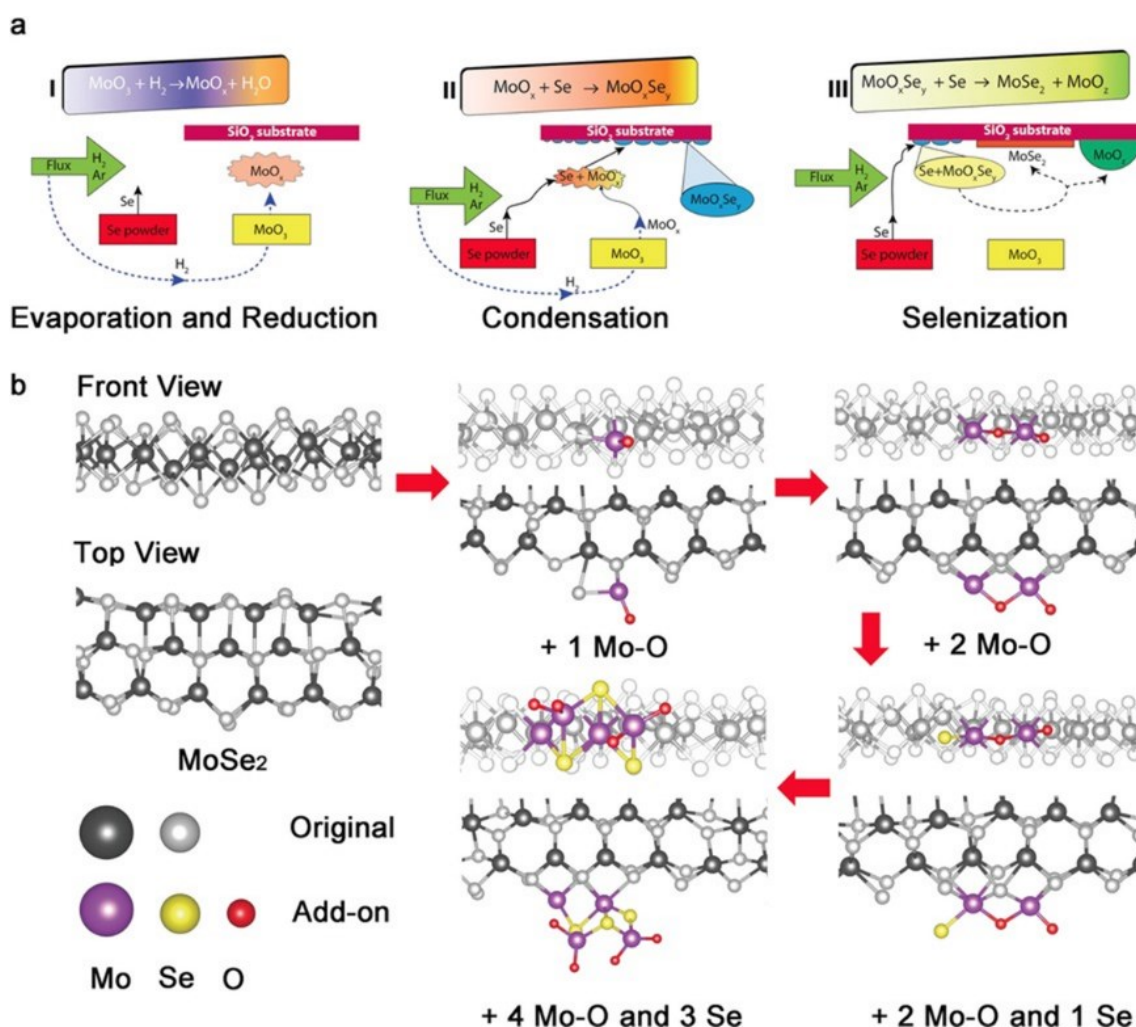
In the synthesis of 2D materials, there are two main categories: top-down and bottom-up approaches<sup>75,76</sup>. In simple words, top-down approach is to directly break the van der Waals (vdW) attraction of bulk samples by using either mechanical or chemical method. The first graphene is mechanically exfoliated from graphite by using Scotch tape method in 2004<sup>7</sup>. The quality of mechanical exfoliation is good, and the cost as well as the required technique are low. However, uniformity, productivity and the nanosheet size are low, that is inapplicable in industry. To increase the productivity, the ball milling method is used to exfoliate large numbers of layered materials simultaneously, the quality and uniformity are still poor<sup>77</sup>.

In terms of the chemical method, ultrasonication-based exfoliation is the most common way to peel off the layered structure into single layer because it is efficient<sup>78,79</sup>. With the assist of ion intercalation or ion exchange before the agitation normally ultrasonication, the lower power can be applied to the bulk to obtain higher quality single layer materials. Although the productivity is much higher than mechanical exfoliation, the quality, uniformity, and scalability are still hardly controllable.

The bottom-up method normally can be divided into two main categories: chemical vapor deposition (CVD), and molecular beam epitaxy (MBE), which demonstrate more promising way to fabricate uniform, high quality and large scale 2D materials, since the desired chemical environments are prepared for the growth from gas phase atoms to 2D materials<sup>80-85</sup>. MBE performs higher precision but with higher cost and longer fabrication duration due to the requirement of ultrahigh vacuum. Via tremendous trials and errors in precursors' ratio, gas flux, carrier gas, substrates, pressure, growth temperature, and growth duration etc., and improving the understanding of the

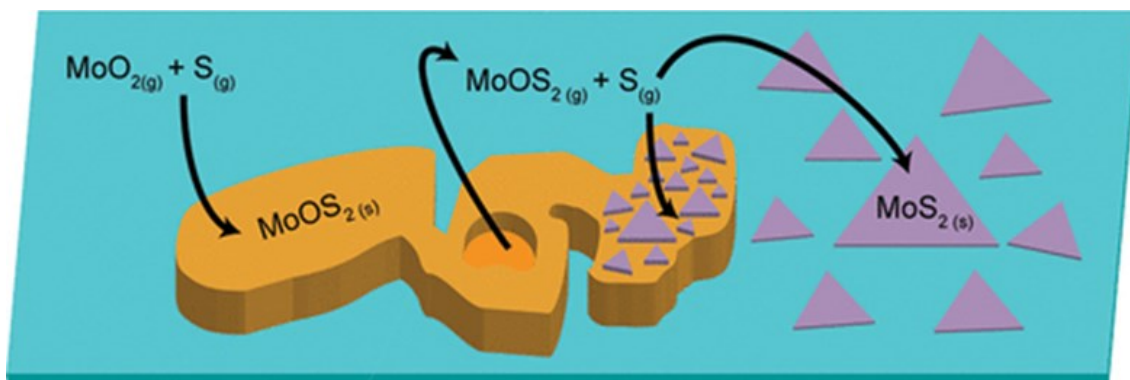


mechanisms of 2D growth, CVD is also controllable to fabricate wafer-scale for part of 2D materials to achieve commercial fabrication<sup>81-83</sup>. There are still a lot of challenges in the morphology control in 2D-TMDCs<sup>86</sup>.



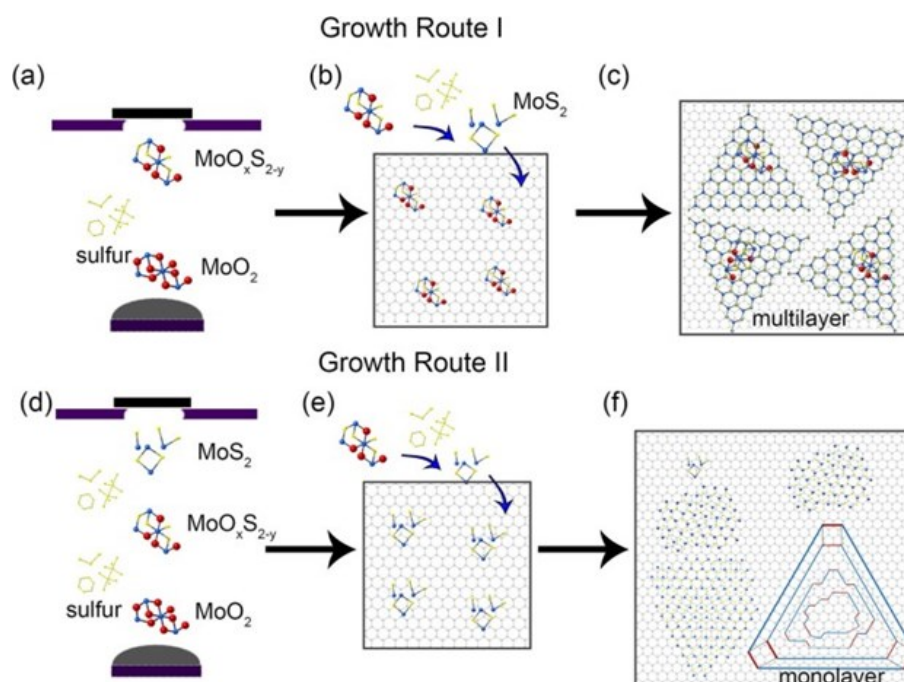


formed by the selenization of  $\text{MoO}_x$  is randomly distributed on the substrate. The further selenization assisted by the aligned nanoparticle  $\text{MoO}_2$  forms the single-layer  $\text{MoSe}_2$ . On the other hand, Pondick *et al.* suggested another three-step growth model (Figure 10)<sup>88</sup>. The vaporized reactants, gas phase S and  $\text{MoO}_2$ , form  $\text{MoOS}_2$  intermediate island on the substrate. The further evaporation and sulfurization of the intermediate finally gradually synthesizes the  $\text{MoS}_2$  monolayer.

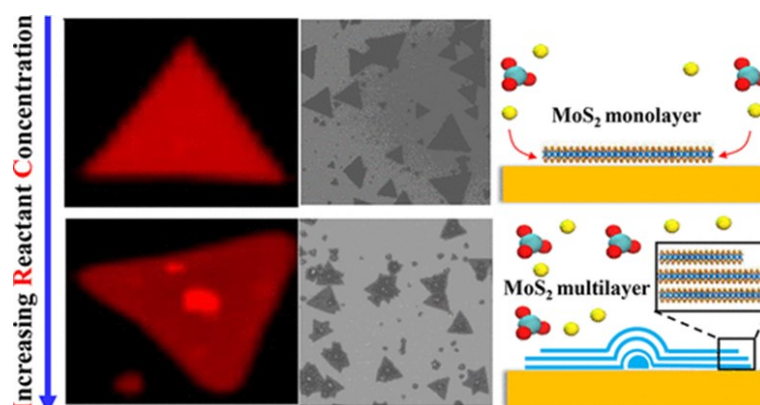


**Figure 10. Scheme of the three-step growth model.** The vaporized reactants form a  $\text{MoOS}_2$  island. Then, the further vaporization and sulfurization forms  $\text{MoS}_2$  monolayer<sup>88</sup>.

Different from the previous two articles, Zhu *et al.*<sup>89</sup> and Zhou *et al.*<sup>90</sup> also provided few-layer growth dynamics that are because of the high concentration of reactants (Figure 11 & Figure 12). Zhu *et al.* suggested the appropriate concentration leads the formation of single-layer or few-layer  $\text{MoS}_2$  from the sufficient sulfurization of  $\text{MoO}_x\text{S}_{2-y}$  nanoparticle nuclei on the substrate. The excess concentration of reactants leads the aggregation of  $\text{MoO}_x\text{S}_{2-y}$  nuclei on the surface and hence, multilayer  $\text{MoS}_2$  and the fullerene-like particles are formed. Slightly different from the previous one, Zhou *et al.* recommended the optimal reactants concentration facilitating reduction of  $\text{MoO}_{3-x}$  to  $\text{MoS}_{2-x}$  nuclei. It is also beneficial to the epitaxial growth to form single-layer  $\text{MoS}_2$ . On the contrary, high concentration leads the rapidly aggregation of  $\text{MoO}_{3-x}\text{S}_y$  nanoparticles nuclei. The insufficient sulfurization of these nuclei becomes a cap-like structure that facilitates the few-layer growth.



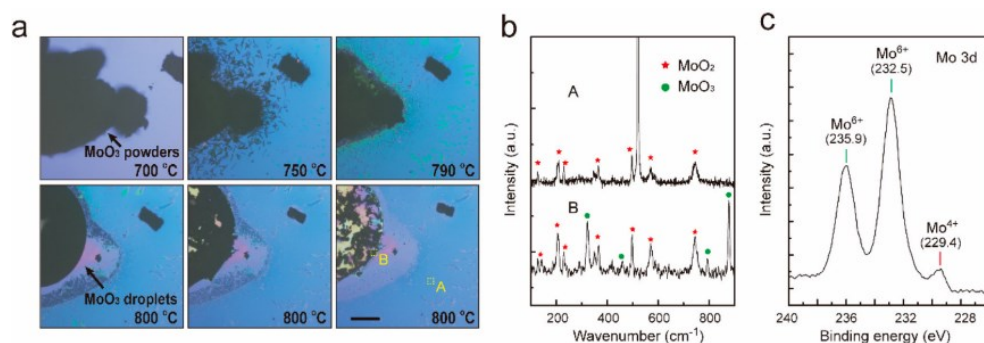
**Figure 11. Schematics of nucleation and growth kinetics of MoS<sub>2</sub>. a-c, high and (d-f) low concentration of reactants by controlling the gas flux<sup>89</sup>.**



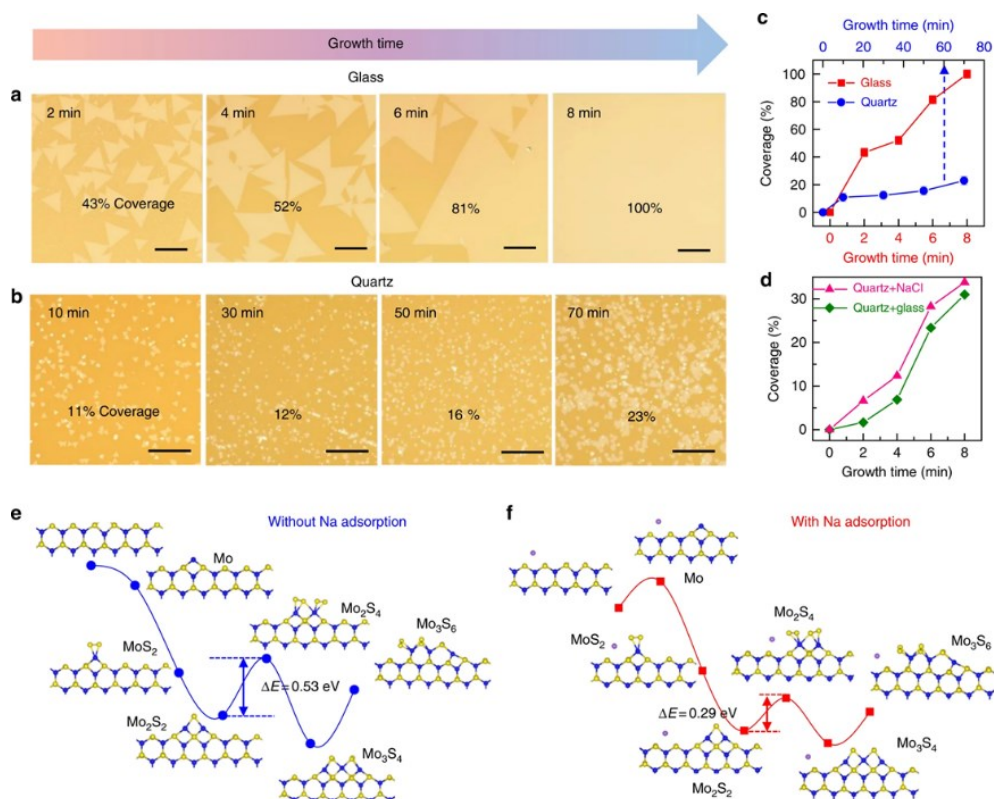
**Figure 12. Schematics of nucleation and growth kinetics of MoS<sub>2</sub> in low and high concentration of reactants by controlling the gas flux and temperature<sup>90</sup>.**

Although there is a *in situ* optical investigation of synthesis, the growth kinetics and the subsequent reactions are still uncertain (Figure 13)<sup>91</sup>. They proposed MoO<sub>2</sub> serves as the intermediate for the nucleation and mass transport confirmed by ex situ Raman spectroscopy and X-ray photoelectron spectroscopy (XPS). In a case of wafer scale MoS<sub>2</sub> monolayer, a soda-lime glass was applied as a substrate, that the sodium atoms assisted the atom-by-atom epitaxially growth (Figure 14)<sup>83</sup>. The sodium adsorption is energy favorable for this epitaxial growth confirmed by DFT calculations. However, other report

of wafer scale TMDCs monolayer is absent by using similar method. The growth kinetics are still required to experimentally confirm for later optimal and general purpose.



**Figure 13. Optical images with spectroscopy.** **a**, *In situ* images during growth and the deposition of MoO<sub>2</sub> on a SiO<sub>2</sub>/Si substrate. Scale bar is 80  $\mu$ m. **b**, Ex situ Raman spectra of the marked areas in (a), and **c**, Ex situ XPS spectrum of the deposited MoO<sub>2</sub> film. **Figure 13** is reproduced from Ref. <sup>91</sup>.



**Figure 14. Substrate effect in terms of coverage and energy comparison.** **a**, Serial images of soda-lime glass from 2 to 8 mins. **b**, Serial images of quartz glass from 10 to 70 mins. Scale bars are 100  $\mu$ m in (a) and 50  $\mu$ m in (b). **c**, MoS<sub>2</sub> coverage comparison between soda-lime glass and quartz. **d**, MoS<sub>2</sub> coverage comparison between NaCl coating quartz and downstream positioned quartz. **e,f**, DFT calculated epitaxial growth energy diagram, (e) without, and (f) with sodium adsorption. **Figure 14** is reproduced from Ref. <sup>83</sup>.



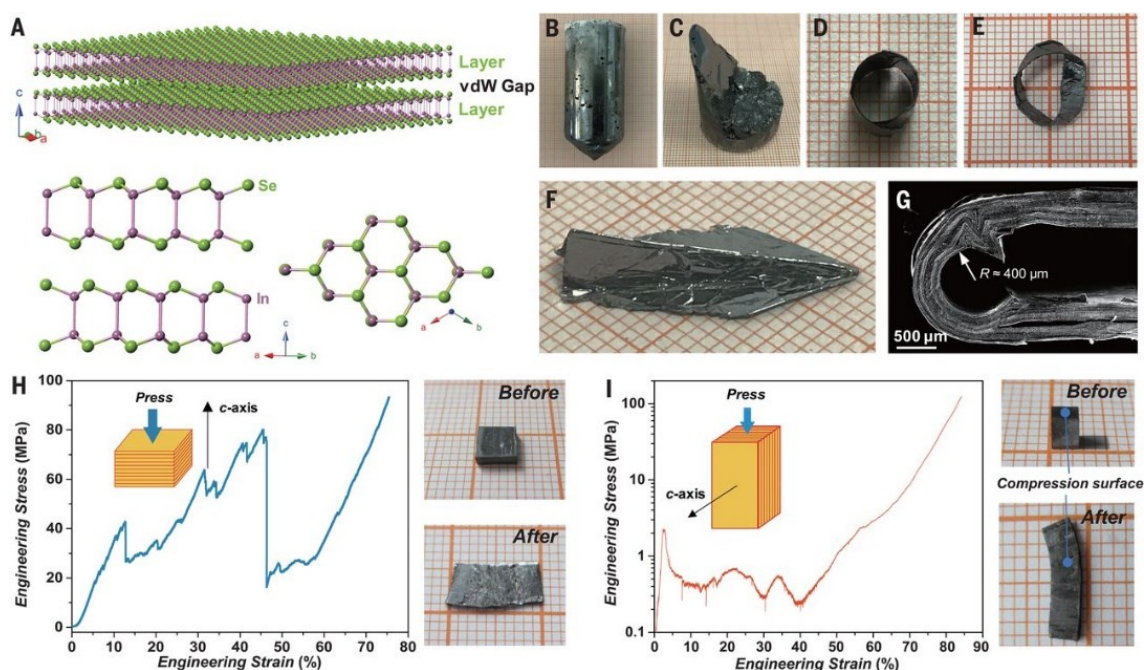
To date, the studies of intermediate species are still insufficient to provide a general growth kinetics in TMDCs. In order to unveil the intermediate species and growth kinetics, the experiments are designed to produce more intermediate products. During the trials and errors session, the ReSe<sub>2</sub> is found that is ungrowable without H<sub>2</sub> gas flow, and H<sub>2</sub> gas is a good reducing agent. The gradually increase of the H<sub>2</sub> gas flux provide different morphology of the ReSe<sub>2</sub> thin film with different size of unknown agglomeration. Via atomic imaging by STEM and EELS, the agglomeration formed by clusters are confirmed, which is octahedral Re<sub>6</sub>Se<sub>8</sub>. The HAADF-STEM can provide sufficient  $Z^2$  contrast to recognize the Re and Se atoms, and EELS is efficient to collect signals from the thin specimen to analyze its chemical information. The best option is to ex situ control the synthesis morphology due to the fact that it is unable to work *in situ* in this stage. The intermediate species can be well kept by changing synthesis parameters, mainly duration and carrier gas flux. Hence, the growth dynamics can be understood by the middle stage.

### 1.3. Unexpected plasticity in vdW materials

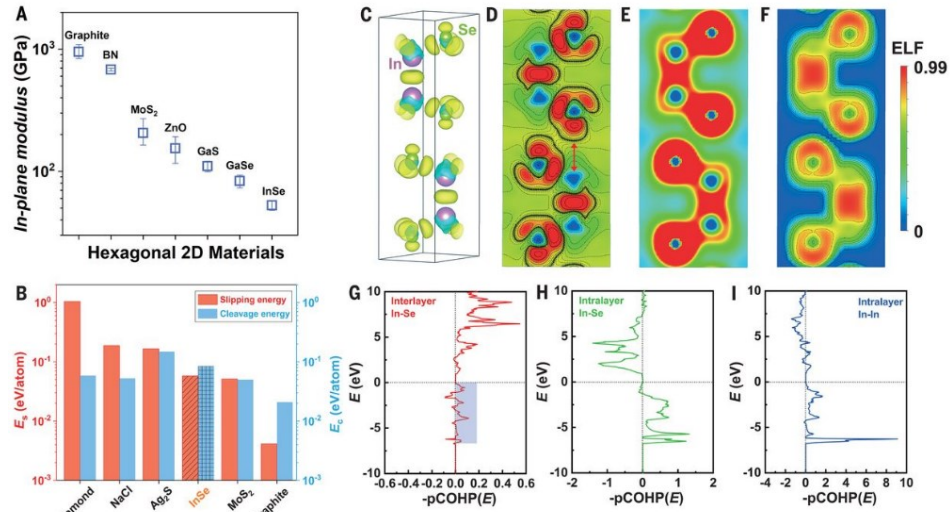
VdW layered materials always give us an impression that is extremely brittle, for example graphite. However, in 2020, a single crystal indium selenide (InSe) has been reported which perform exceptional plasticity in Science, that even can do origami (Figure 15)<sup>92</sup>. Due to the limitation of the instrument, the compressional strain along both in-plane and out-of-plane is at least 80%. Via the analyzing the bonding strength, and the mechanical properties by DFT calculations, they believe the extraordinary plasticity of  $\beta$ -InSe is from a sufficiently large cleavage, provided by the long-range coulombic In-Se interlayer interaction and Se-Se vdW attractions, with a relatively low slipping energy (Figure 16). They proposed the prediction of brittle or ductile by a deformability factor, that is proportional to the cleavage energy and anti-proportional to the slipping energy



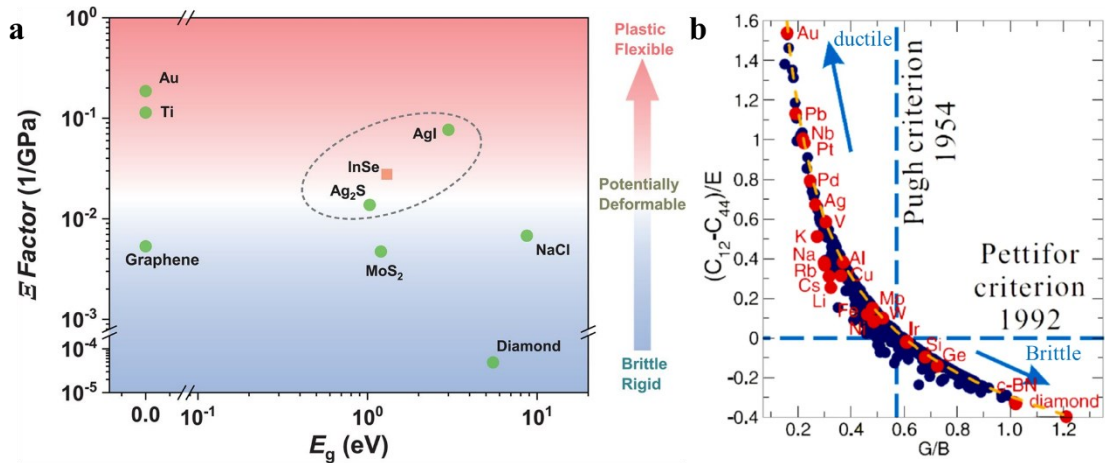
and Young's modulus along basal plane (Figure 17a), which was developed from Rice-Thompson criteria<sup>93</sup>, that suggested when the ratio of the product of shear modulus ( $G$ ) and the distance of Burger's vector ( $\vec{b}$ ) to surface energy ( $E_{Sur}$ ) is larger than 7.5 to 10, the metals would occur a complete fracture by expansions of a sharp cracks, except for the face-centered cubic and certain borderline body-centered metals. On the contrary, if the ratio is smaller than 7.5 to 10, the metals are ductile. Rudenko *et al.* calculated a low Rice-Thompson's ratio of InSe which is approximately 3.2, due to the low shear modulus<sup>94</sup>. However, if we follow this assumption, all of the slipping 2D materials, which is low shear modulus would behave ductile. Although Rice updated the ratio with an unstable stacking energy, which is directly proportional to the product of shear modulus and the square of Burger's vector, the prediction of the ratio was very similar<sup>95</sup>.



**Figure 15. The exceptional plasticity of InSe.** A, Structure of  $\beta$ -InSe. B, An image of an as-grown  $\beta$ -InSe crystal, and C, its cleavage surface. D-F, The origami of the  $\beta$ -InSe crystal. G, Cross section scanning electron microscopy (SEM) image of a folded  $\beta$ -InSe. H,I, Compression engineering stress-strain experiment along (H) out-of-plane, and (I) in-plane direction. Figure 15 is reproduced from Ref. <sup>92</sup>.



**Figure 16. Mechanical and chemical properties of  $\beta$ -InSe.** **A**, Comparison of intralayer modulus in the perspective of hexagonal 2D inorganic semiconductors. **B**, DFT calculated slipping energy and cleavage energy in comparisons with other materials. **C-I**, Calculated differential charge density (**C**) in perspective view, (**D**) along  $\langle 1\bar{2}10 \rangle$ , (**E**) charge density, (**F**) electron localization function (ELF), crystal orbital Hamiltonian populations (COHP) for (**G**) interlayer In-Se bonding, (**H**) intralayer In-Se bonding and (**I**) Intralayer In-In bonding<sup>92</sup>.



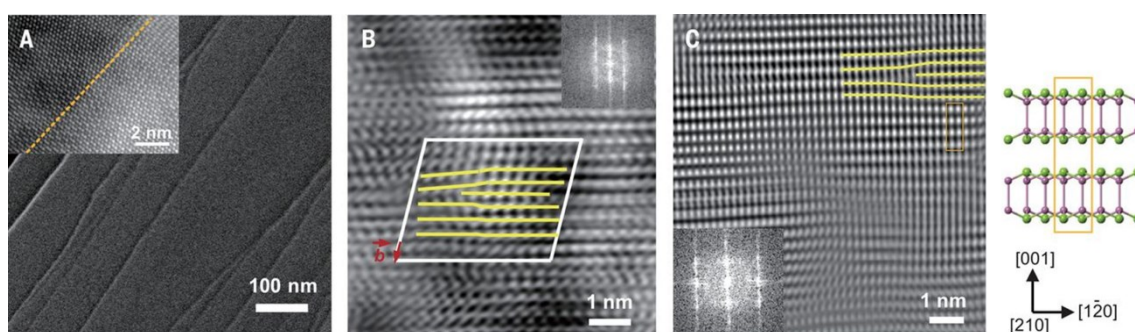
**Figure 17. Different prediction of the materials which is ductile or brittle.** **a**, Deformability factor<sup>92</sup>. **b**, Pugh-Pettifor criterion<sup>96</sup>. Blue vertical dashed line is 0.57.

The prediction of ductile or brittle is different from Pugh's criterion<sup>97</sup> and Pettifor's criterion<sup>98-100</sup>. The Pugh's criterion stated that the brittle materials have a generally high shear-to-bulk moduli ratio, and the ductile materials have a small ratio<sup>97</sup>. On the other hand, the Pettifor's criterion has indicated, the Cauchy pressure (CP), the difference between two elastic constants  $C_{12}$  and  $C_{44}$  ( $CP = C_{12} - C_{44}$ ), has a relationship with bonding characteristics<sup>98-100</sup>. The ductile materials generally have non-directional

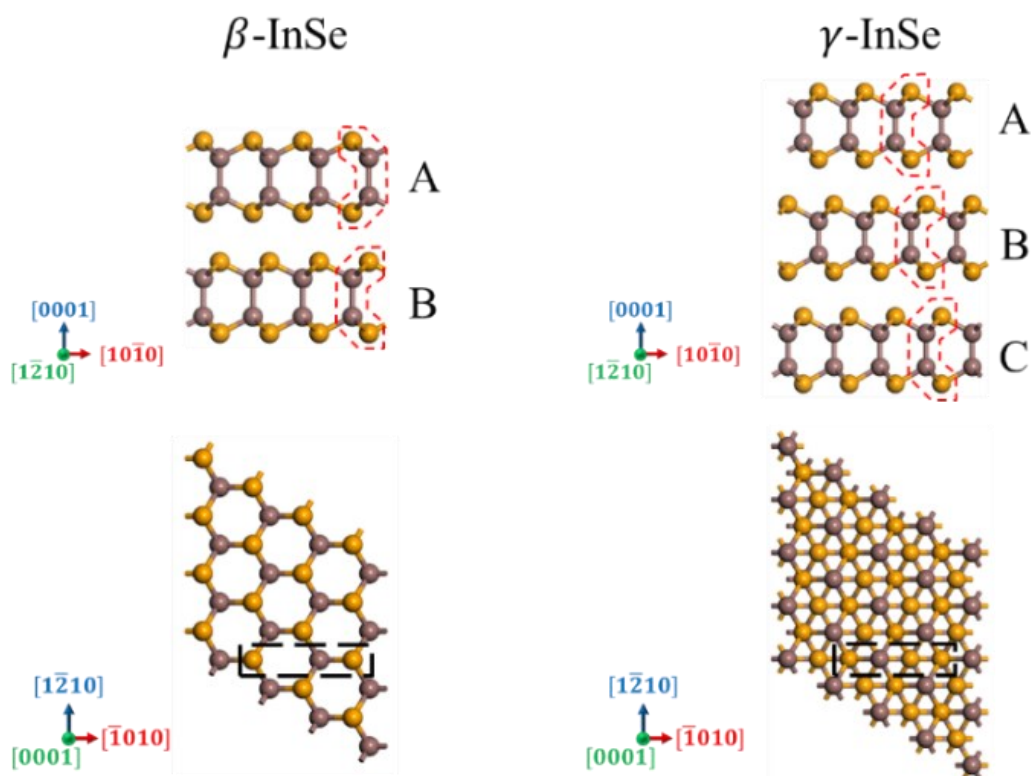


metallic bonds with  $CP > 0$ , and the brittle materials generally have directional covalent bonds with  $CP < 0$ . Senkov and Miracle have gathered total 332 species, including compounds and metals elucidate the Pugh-Pettifor relationships for Cubic crystalline (Figure 17b)<sup>96</sup>. Which is the better prediction about the brittle or ductile nature of a material? After comparing all the models, one thing that we can confirm that low shear modulus is commonly good indicator of the ductility.

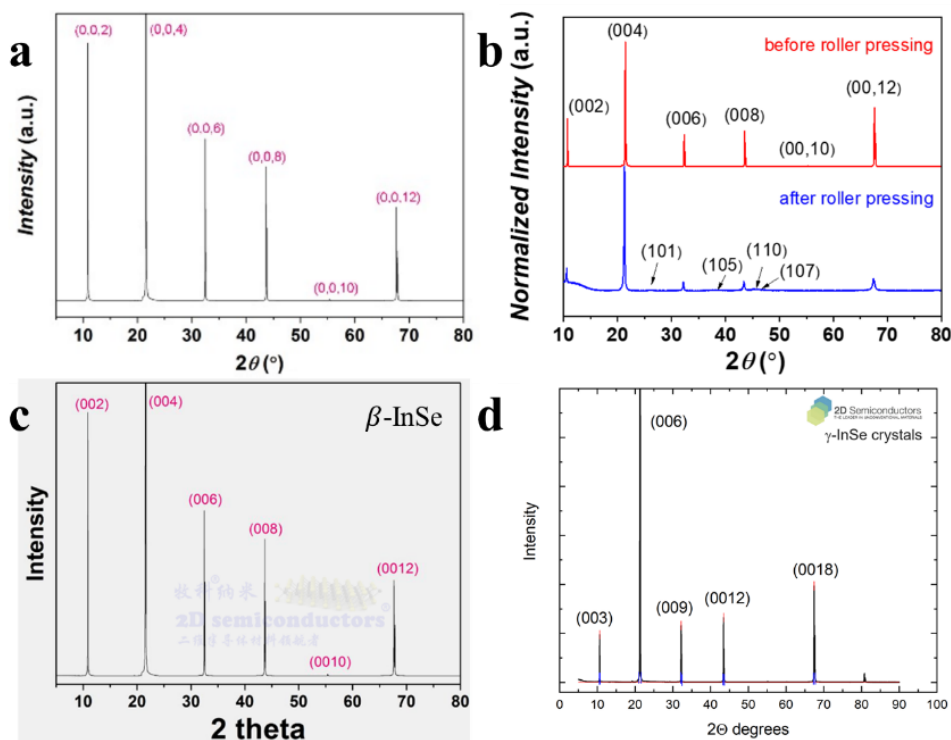
Although they have built the deformability model via the bonding strengths, and energies about cleavage and slipping, the plasticity mechanism of InSe still remains some questions. How is the microcrack propagation stopped? What slows down the structural fracture? Why the microcracks tend to propagate along basal plane rather than edge plane? The overlooked phase transition contributions of InSe seems to play an important role in the plasticity. In their ADF-STEM atomic image (Figure 18a), there are 4 atomic columns for a unit of  $\langle 10\bar{1}0 \rangle$  direction ( $\sim 7 \text{ \AA}$ ) rather than 3, that indicates the structure of InSe is  $\gamma$  phase rather than  $\beta$  phase (Figure 19). Although the stacking fault was stated, the stacking order or phase was also undistinguishable in Figure 18b-c. On the other hand, the inconsistency of X-ray diffraction (XRD) data in terms of peaks ratio (3<sup>rd</sup> to 5<sup>th</sup> peaks) also indicate the present of phase transition (Figure 20).



**Figure 18.** ADF-STEM images of a deformed InSe. **A**, Atomic image, and the slipping steps along  $[0001]$ . **B,C**, Cross section view along **(B)**  $\langle 12\bar{1}0 \rangle$ , and **(C)**  $\langle 10\bar{1}0 \rangle$ <sup>92</sup>.



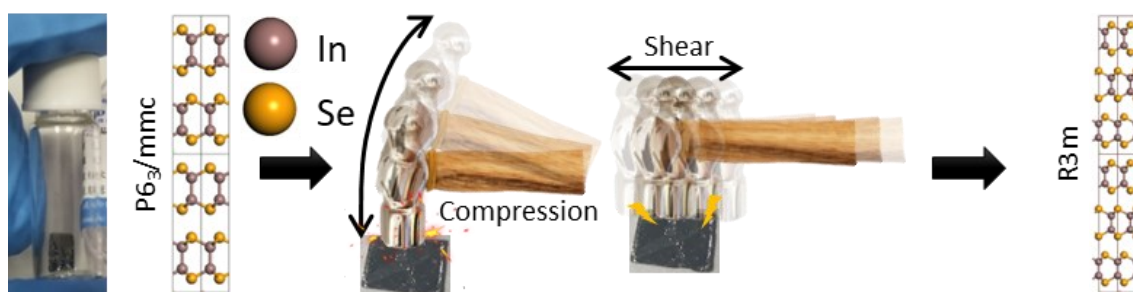
**Figure 19.** Atomic structure of  $\beta$ - and  $\gamma$ -InSe along  $\langle 1\bar{2}10 \rangle$  and  $[0001]$ . The red dashed lines indicate the difference of stacking order and the black dashed lines show a unit of  $\langle 10\bar{1}0 \rangle$  direction.



**Figure 20.** XRD  $\theta$ - $2\theta$  experiments. **a**, XRD pattern of a cleaved InSe surface. **b**, XRD data of InSe before and after roller pressing<sup>92</sup>. **c,d**, XRD patterns of commercial products of (c)  $\beta$  phase InSe<sup>101</sup> and (d)  $\gamma$  phase InSe<sup>102</sup>.



In order to study the full mechanism of the plasticity of InSe, clean cracks and phase transition are created by gentle and discrete compression and shear force via a small hammer as a scheme in Figure 21. XRD and Raman will be conducted to have a preliminary sample check. Further, focused ion beam (FIB), atomic scale HAADF-STEM, and *in situ* TEM will be used to study the cross-section view, projection view, and micro-view with other 2D materials such as MoS<sub>2</sub> to unveil the mechanism of the superior plasticity of InSe.

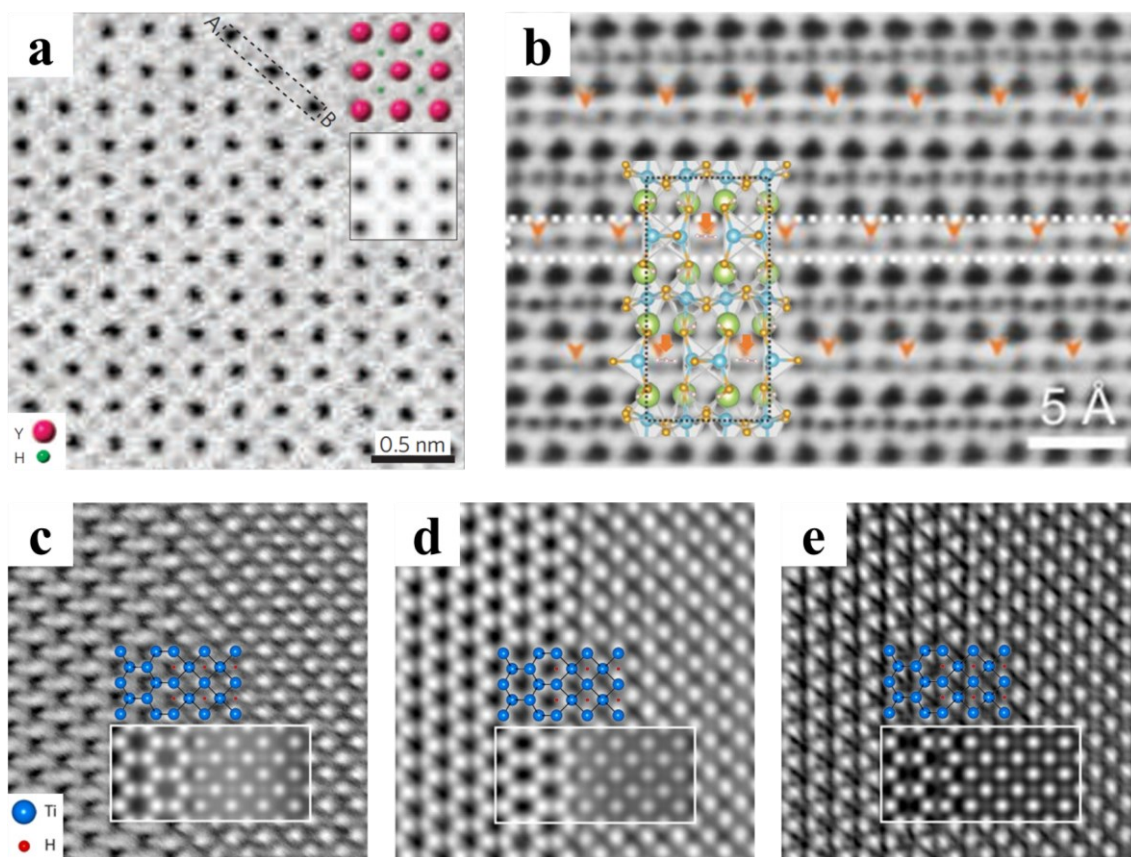


**Figure 21. Experimental scheme of the external force onto the  $\beta$ -InSe single crystal.**

#### **1.4. Quantitative charge density study of hydrogen bonds in MOFs**

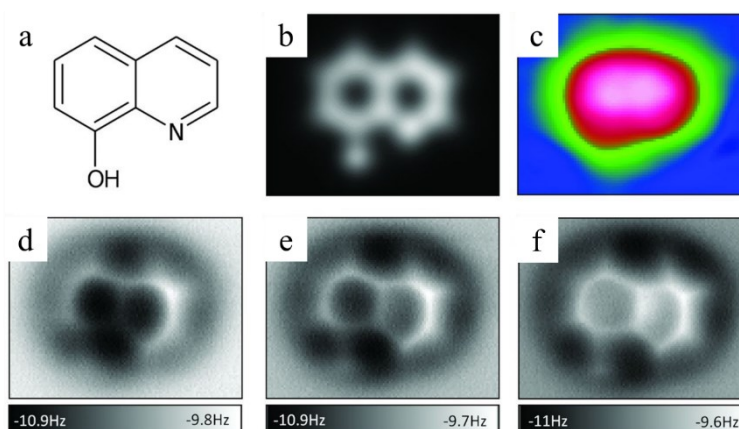
Imaging light elements, especially for hydrogen, is a difficult project. Via the development of technology, there are two approaches that can locate hydrogens: STEM<sup>103-105</sup> and non-contact AFM<sup>106,107</sup>. Annular bright field (ABF)-STEM and integrated differential phase contrast (iDPC)-STEM have demonstrated how to capture hydrogen atoms via certain relatively stable inorganic compounds (Figure 22)<sup>103-105</sup>. Figure 22a presents the earliest hydrogen captured by ABF-STEM in YH<sub>2</sub> in 2011. Via controllable ionic liquid gating, SrCoO<sub>2.5</sub> crystal was protonated as H<sub>x</sub>SrCoO<sub>2.5</sub><sup>105</sup> as shown in Figure 22b. They found that the hydrogen concentrations increased dramatically when the doping  $x$  from 1 to 2. Also, the H-H dimers can be stored in between the tetrahedral sites without changing the chemical state of Co<sup>2+</sup> ion. The compensation of the hydrogen doping is through bandgap enlargement and lattice expansion, that prevent

magnetization. This experiment has demonstrated the potential of energy storage and bandgap engineering. Similar viewpoint of Graaf *et al.*<sup>103</sup>, high volumetric density hydrogen can be safely stored in metals for energy storage. In their ABF-, iDPC-, and differentiated differential phase contrast (dDPC)-STEM images in Figure 22, iDPC-STEM demonstrated the highest signal-to-noise ratio (SNR) along the atomic columns of Ti and H, but the contrast is slightly better in some area of dDPC-STEM image. Although ABF-, iDPC, and dDPC-STEM demonstrated the possibility of hydrogen atoms, atomic scale organic molecule imaging is still challenging due to the weakly scattering nature of light elements and the irradiation sensitive problems.



**Figure 22. Hydrogen acquired by STEM.** a-b, ABF-STEM image of a,  $\text{YH}_2$ <sup>104</sup> and b, protonated  $\text{H}_x\text{SrCoO}_{2.5}$ <sup>105</sup>. H-H dimers are indicated by orange arrows in (b). c-e,  $\alpha$ -Ti to  $\gamma$ -TiH interface images taken by (c) contrast inverted ABF-STEM, (d) iDPC-STEM, and (e) contrast inverted dDPC-STEM<sup>103</sup>. Field of view: 3.5 x 3.5 nm in (c-e). The boxes in (a,c-e) display the simulated images.

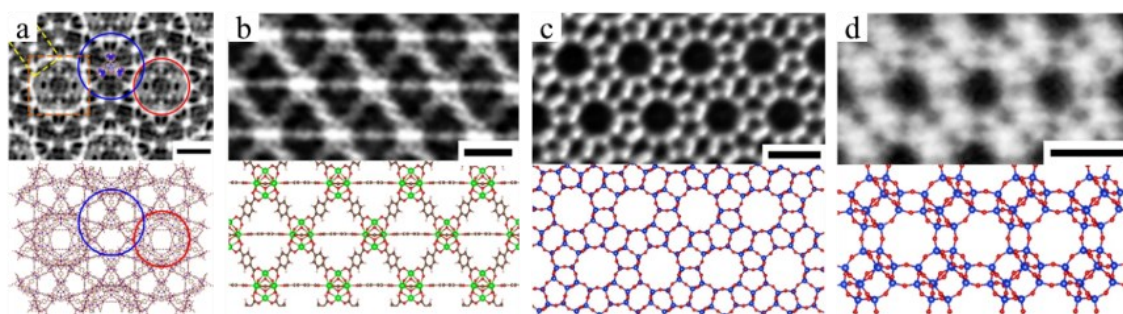
Non-contact AFM uses CO molecule decorated tip as a probe to image organic molecules (Figure 23)<sup>106</sup>. A single 8-hydroxyquinoline molecule suspended on Cu (111) can be successfully imaged. However, this technique requires not only high vacuum ( $\sim 10^{-8}$  Pa), but also ultralow temperature ( $\sim 5$  K) and long acquiring time ( $\sim 10$  mins)<sup>106,108</sup>. Comparing with STEM, it is possible to acquire the organic molecules with room temperature (RT), and shorter acquisition time (in several seconds). It is more meaningful if the biomolecules and organic compounds can be studied in RT, because most of the applications are under RT. It is excited to improve the imaging or data processing techniques of TEM in order to conduct more investigations about organic compounds.



**Figure 23. Images of a single 8-hydroxyquinoline on Cu (111).** **a**, Theoretic structure. **b**, DFT simulated electron density maps. **c**, Scanning tunnelling microscopy (STM) topography image. **d-f**, Constant-height AFM frequency shift images with respect to the Cu substrate. The height above the Cu substrate is **(d)** 30 pm, **(e)** 10 pm, and **(f)** 0 pm<sup>106</sup>.

Recently, zeolites like ZSM-5 and SAPO-34, and metal-organic frameworks (MOFs) such as MIL-101 and UiO-66 have been reported to use iDPC-STEM to identify the structures<sup>109-111</sup> (Figure 24). Compared with the single organic molecules or biomolecules, MOFs provide an opportunity to study the electrocatalysis due to the flexibly porous structure by combining the metal/metal clusters and organic ligands, that creates large number of catalytic sites<sup>112</sup>. It is capable of identifying the MOFs to get certain experience and idea before challenging the atomic scale single biomolecule by

using TEM. In order to further improve this alternative energy conversion technology, the structure has to be clearly studied, and hence the hydrogen evolution reaction (HER) or oxygen evolution reaction (OER) via MOFs can be optimized by strategically changing the structure of frameworks.



**Figure 24. Examples of zeolites and MOFs images by using iDPC-STEM. a, MIL-101. b, UiO-66. c, ZSM-5. d, SAPO-34. Scale bars: 1 nm (a,d), 3 nm (b,c)<sup>110</sup>.**

This idea was conceived by the recent experiments<sup>50</sup>. It was found that the structure of Ni-benzene-dicarboxylate (Ni-BDC) is slightly different from the theoretical model. The images and the further DFT relaxed models will be discussed in Chapter 5. The identifications of the MOFs' structures are beneficial to the predictions, experimental strategic planning, and performance optimizations. Surprisingly, the hydrogen on the benzene ring and metal/metal clusters were also observed. It is also a good opportunity to quantitatively study the different bonding of hydrogen.

## 1.5. Summary

In this chapter, the synthesis problems about the intermediate species and growth kinetics, the uncertainties of the mechanism in plasticity in 2D materials, and the flexibly complex structure of MOFs have been indicated.

In this thesis, the three different topics have been studied by resolving the structures via different TEM techniques. In the synthesis kinetics and intermediate species, HAADF-STEM and EELS-STEM can be used for acquiring the atomic structure and the



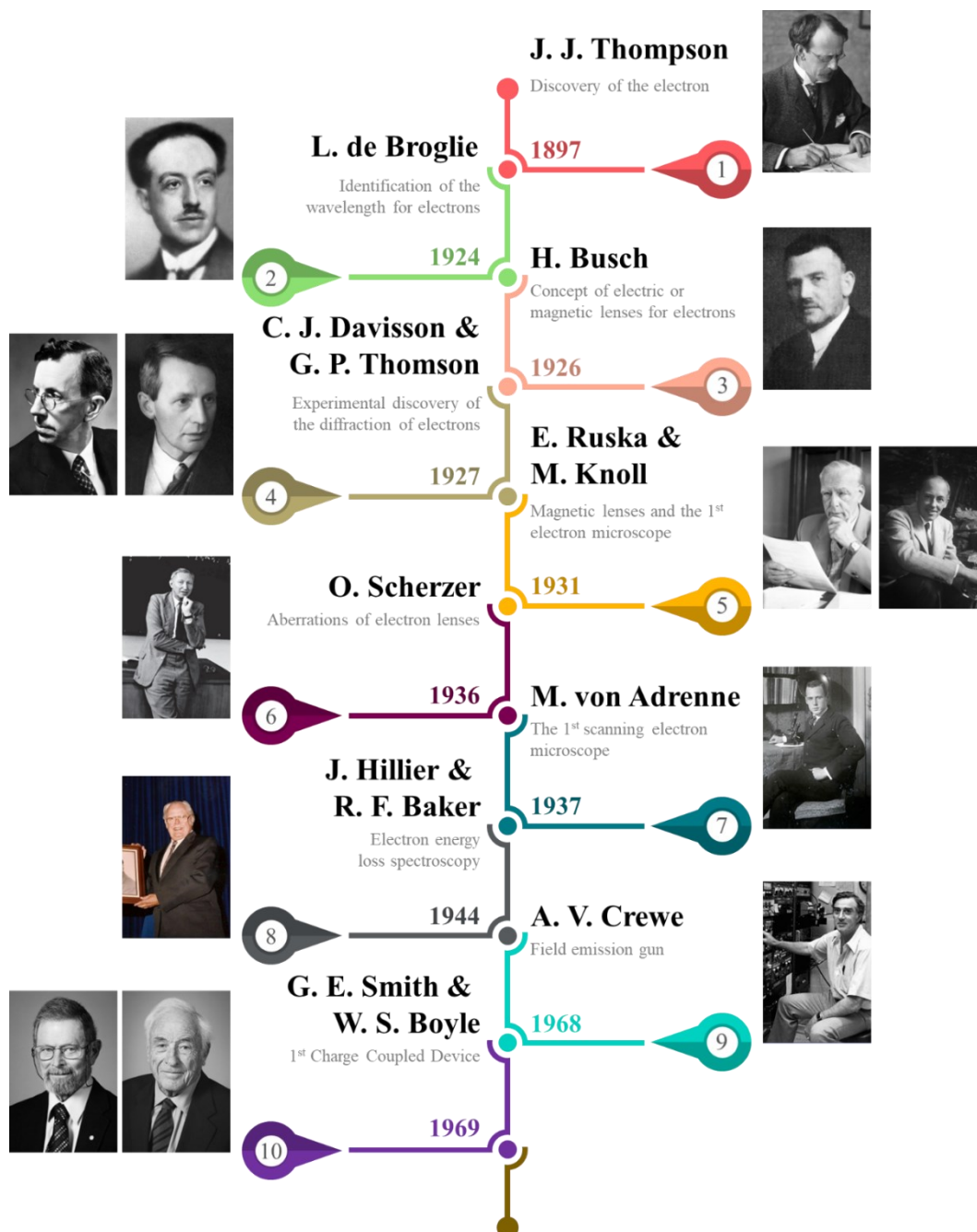
compositions of the unknown species. In the study of the mechanism of plasticity, the sample preparation strategy and the *in situ* experiments can explore the mechanisms of the plastic material. Finally, the ability of imaging hydrogen via iDPC-STEM is utilized to acquire MOFs to study the possible applications.

In the next chapter, the working principle of TEM with the related techniques, such as EELS will be also introduced. By understanding the working principle, advantages, and the limitations of TEM, the experimental designs, the use of TEM, and the data analysis are like a hot knife through butter. The preparations such as TEM specimens are also included in the next chapter.





## Chapter 2. TEM: History, Principle and Experiment Preparations



**Figure 25. History of electron microscopy.** The images are reproduced from Ref. <sup>113</sup>, <sup>114</sup>, <sup>115</sup>, <sup>116,117</sup>, <sup>118,119</sup>, <sup>120</sup>, <sup>121</sup>, <sup>122</sup>, <sup>123</sup>, and <sup>124,125</sup> for timeline 1-10, respectively (top to bottom and left to right (if there are two images in the same row)).

In material science, structure-properties relations are always emphasized. As Francis Crick said: “If you want to understand function, study structure.”<sup>126</sup>. Furthermore,



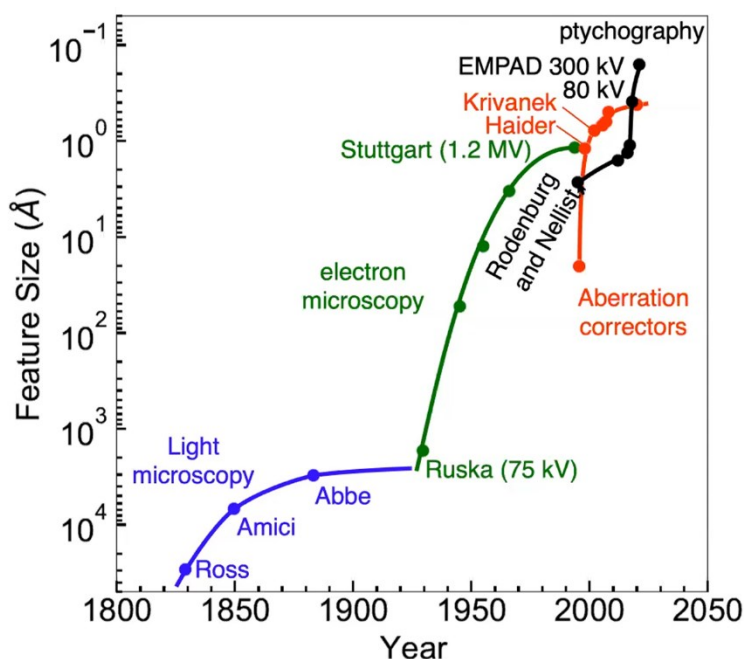
the most valuable study of the structure must be the atomic structure. In order to achieve this goal, many physicists have investigated electron microscopy (EM) which can surpass the resolution of optical microscope, which is widely used to observe microstructure even now.

The investigation of electron microscopy was inspired by the discovery of the electron by Joseph John Thompson<sup>113</sup> in 1897<sup>127</sup>, and the identification of the wavelength of electrons by Louis de Broglie<sup>114</sup> in 1924<sup>128</sup>. Then, the electron diffraction has been experimentally conducted by Clinton Joseph Davisson<sup>116</sup> and George Paget Thomson<sup>117</sup> in 1927<sup>129</sup>. With the idea of lenses for electrons controlled by magnetic or electric field by Hans Busch<sup>115</sup> in 1926<sup>130</sup>, Ernst Ruska<sup>118</sup> proved the magnetic coil can act as an electron lens mathematically and experimentally in 1929, and then Ernst Ruska and Max Knoll<sup>119</sup> built the first electron microscope in 1931<sup>131</sup>. Otto Scherzer<sup>120</sup> has published that electron lenses have unavoidable aberrations that limits the resolution in 1936<sup>132</sup>, and then the spherical and chromatic aberrations have been experimentally corrected, that was demonstrated by cylindrical lenses in 1947<sup>133</sup>. However, the spatial resolution of EM was actually improved by aberration-corrected since 1990s<sup>134</sup>. In 1937, Manfred von Ardenne<sup>121</sup> developed 1<sup>st</sup> high-resolution (HR) scanning EM (SEM)<sup>135</sup>, and the scanning probe technology was also applied to transmission EM (TEM). That becomes nowadays scanning TEM (STEM). In terms of the study of chemical analysis with TEM, James Hillier<sup>122</sup>, and R. F. Baker established the foundation of electron energy loss spectroscopy (EELS)<sup>136</sup>. In 1968, Albert Victor Crewe<sup>123</sup> has built the 1<sup>st</sup> field emission gun (FEG)<sup>137</sup>, which provided brighter with higher resolution, benefitted by the refocused small probe size<sup>138</sup>. The invention of charge-coupled device (CCD)<sup>139</sup> in 1969 by George Elwood Smith<sup>125</sup> and Willard Sterling Boyle<sup>124</sup> started the digitizing images and spectra. Other



than the improvement of hardware, digital data can be deconvoluted to get the higher quality results. The short EM history is summarized in Figure 25.

With the development of personal computer, 4D-STEM technique such as electron microscope pixel array detector (EMPAD)<sup>140</sup> and reconstruction algorithm<sup>141,142</sup>, the resolving power of electron microscopes can be improved by ptychography (Figure 26), that reached the highest resolution that resolves the Sc-O separation around 23 pm<sup>143</sup>, that is the new world record of the spatial resolution. The resolution can be even beyond the Abbe diffraction limit, and now the resolution is limited by thermal vibration of the atoms<sup>144</sup>.



**Figure 26. The evolution of spatial resolution in microscopy.** This image is reproduced from the lecture video of David A. Muller<sup>145</sup>.

## 2.1. Introduction to transmission electron microscopy

After the brief introduction of the development history and resolution revolution of (S)TEM, the more details of the fundamental physics of (S)TEM with its techniques will be introduced below. Resolving power or spatial resolution always is the most





concerned parameters of a microscope. Via Abbe diffraction limit<sup>144</sup>, and Rayleigh criterion<sup>146</sup>, both of them indicated the wavelength of the source, light, restricted the resolution of microscope. The equations are denoted as follows respectively,

$$d_{min} = \frac{\lambda}{2n\sin\beta} \quad \text{eq. 1}$$

$$\theta_{min} = \frac{0.61\lambda}{n\sin\beta} \quad \text{eq. 2}$$

where  $d_{min}$  is the minimum resolvable distance,  $\lambda$  is the wavelength of the source,  $n$  is the refractive index (for air and vacuum,  $n = 1$ ),  $\beta$  is the half of collection angle,  $\theta_{min}$  is the minimum resolving angle.

The discovery of the electron<sup>127</sup> and the wave nature of electrons<sup>128</sup>, people found that the wavelength of electrons can be far lower than that of photons by using the same energy around a 1000 times. That is why people to build EM to explore atomic world because of the higher resolution limit. The equations are denoted as follows respectively,

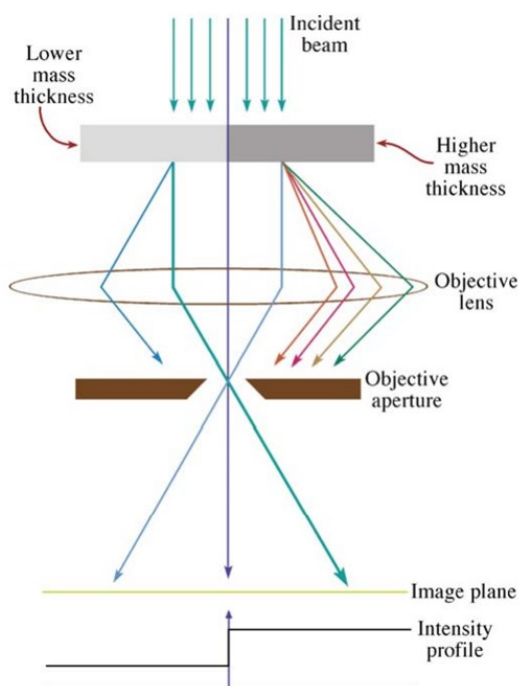
$$\lambda_e = \frac{h}{\sqrt{2m_e eV \left(1 + \frac{eV}{2m_e c^2}\right)}} \quad \text{eq. 3}$$

$$\lambda_p = \frac{hc}{E_p} \quad \text{eq. 4}$$

where  $\lambda_e$  is the wavelength of electron,  $h$  is the Planck constant,  $m_e$  is the rest mass of electron,  $c$  is the speed of light,  $eV$  is the energy for the acceleration energy,  $\lambda_p$  is the wavelength of photon, and  $E_p$  is the energy of photon. The commonly used accelerating voltages with the corresponding electron wavelengths are listed in Table 1.

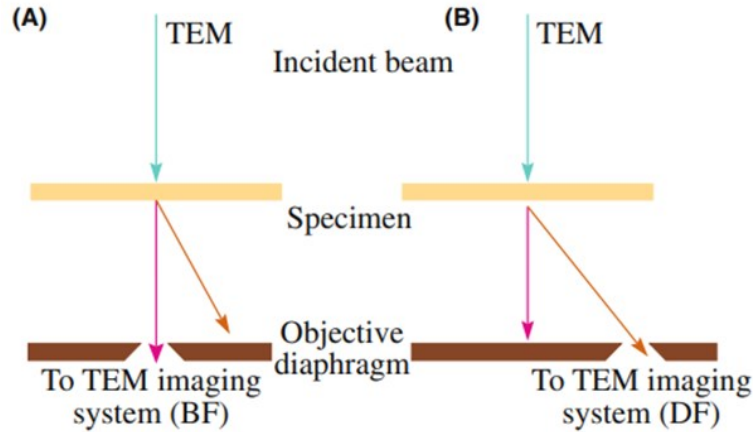
**Table 1. Wavelengths of electrons at commonly used accelerating voltages**

Accelerating voltage (kV)	30	60	80	120	200	300
$\lambda_e$ (pm)	6.997	4.877	4.185	3.355	2.511	1.970



**Figure 27. Schematic diagram of mass-thickness contrast in BF image.** The left part represents lower atomic number or thinner specimen, and the right part represents higher atomic number or thicker specimen. This figure is reproduced from Ref. <sup>147</sup>.

In conventional TEM, the imaging contrast is mainly contributed by mass-thickness contrast, diffraction contrast, and phase contrast. In mass-thickness contrast, in simple words, the heavier element and thicker specimen scatter more electrons, and hence the positions with weaker transmitted signals appear darker in the same image (Figure 27). Diffraction contrast changes with different diffraction signals, which follows Bragg's law<sup>148</sup>, passes through objective aperture. It depends on the signal is selected by the objective aperture in reciprocal space. If the selected diffraction spot is the direct beam, it is called bright field (BF) imaging (Figure 28). If another diffraction spot is selected, it is called dark field (DF) imaging. If there are two different crystals or one crystal with two grains, or even one crystal with empty space and supporting film, the diffraction contrast is brighter for the selected diffraction spot with respect to the crystal or the the orientation of the grain.



**Figure 28. Schematic diagram of BF and DF imaging.** This figure is reproduced from Ref. <sup>147</sup>.

Phase contrast plays an important role in high-resolution (HR)TEM. The ray propagations in HRTEM involve more diffraction beam via a large objective aperture or even removing it. That means more interference from the crystal structure is transmitted. In order to collect HR image, thin specimens are required, since they are weak phase-object (WPO), which weakly scatter electrons. As a result, when electron beam interacts with the object, only a small phase shift of electron beam occurs without changing its amplitude. The phase shift is caused by the interaction between the incident beam and the potential field of specimen projected in the z-direction. After considering the absorption of the specimen, the specimen transfer function in phase-object approximation (POA) is generally denoted as<sup>147,149</sup>,

$$T(\vec{r}) = \exp[i\sigma_e V_t(\vec{r}) - \mu(\vec{r})] \quad \text{eq. 5}$$

where  $\sigma_e$  is the elastic interaction constant,  $V_t(\vec{r})$  is the potential field of specimen projected in the z-direction, and  $\mu(\vec{r})$  is the absorption function. This formula also assumes the incident wave amplitude is unity.

The specimen transfer function ( $T(\vec{r})$ ) can be further simplified if the specimen is very thin, i.e. < several nanometers. The absorption function can be negligible and the



$V_t(\vec{r})$  is  $\ll 1$ . The Taylor's expansion can be applied, neglecting higher-order terms (too small) and the specimen transfer function can be rewritten as,

$$T(\vec{r}) = 1 + i\sigma_e V_t(\vec{r}) \quad \text{eq. 6}$$

This is called WPO approximation (WPOA). For a very thine specimen, the linear relationship between specimen transfer function and the potential of the specimen is shown. The contrast transfer function (CTF) is the product of the aperture function, the envelope function, and the aberration function. Only the aberration function involves phase, and the source is assumed as coherent. So, the other terms such as the aperture function ( $A(\vec{k})$ ), and the envelope function ( $E(\vec{k})$ ) are close to 1. In HRTEM, the CTF in WPOA can be simplified as,

$$\begin{aligned} CTF(\vec{k}) &= A(\vec{k})E(\vec{k})e^{-i\chi(\vec{k})} \\ &\approx e^{-i\chi(\vec{k})} = \cos\chi(\vec{k}) + i\sin\chi(\vec{k}) \end{aligned} \quad \text{eq. 7}$$

where,

$$\chi(\vec{k}) = \frac{\pi}{2} (C_s \lambda_e^3 \vec{k}^4 + 2\Delta f \lambda_e \vec{k}^2) \quad \text{eq. 8}$$

where  $C_s$  is the spherical aberration coefficient,  $\lambda_e$  is the wavelength of electron,  $\vec{k}$  is the vector in frequency space. The image wavefunction is the convolution between the specimen transfer function and the CTF as follows,

$$\begin{aligned} \psi_{imag}(\vec{k}) &= T(\vec{k})CTF(\vec{k}) \\ &= [\delta(\vec{k}) + i\sigma_e V_t(\vec{k})][\cos\chi(\vec{k}) + i\sin\chi(\vec{k})] \\ &= \delta(\vec{k}) - \sigma_e V_t(\vec{k})\sin\chi(\vec{k}) + i\sigma_e V_t(\vec{k})\cos\chi(\vec{k}) \end{aligned} \quad \text{eq. 9}$$



where  $\delta(\vec{k})$  is Dirac delta function. The specimen transfer function in real space can be denoted as,

$$\begin{aligned}\psi_{imag}(\vec{r}) &= 1 - \sigma_e V_t(\vec{r}) * \mathcal{F}[\sin\chi(\vec{r})] \\ &\quad + i\sigma_e V_t(\vec{r}) * \mathcal{F}[\cos\chi(\vec{r})]\end{aligned}\quad \text{eq. 10}$$

So, the image intensity is,

$$\begin{aligned}I_{imag}(\vec{r}) &= \psi_{imag}(\vec{r})\psi_{imag}(\vec{r})^* \\ &= 1 - 2\sigma_e V_t(\vec{r}) * \mathcal{F}[\sin\chi(\vec{r})] \\ &\quad + \{\sigma_e V_t(\vec{r}) * \mathcal{F}[\sin\chi(\vec{r})]\}^2 \\ &\quad + \{\sigma_e V_t(\vec{r}) * \mathcal{F}[\cos\chi(\vec{r})]\}^2\end{aligned}\quad \text{eq. 11}$$

The last two terms are negligible, because  $\sigma_e^2$  is too small. Thus, the intensity can be simplified as,

$$I_{imag}(\vec{r}) = 1 - 2\sigma_e V_t(\vec{r}) * \mathcal{F}[\sin\chi(\vec{r})] \quad \text{eq. 12}$$

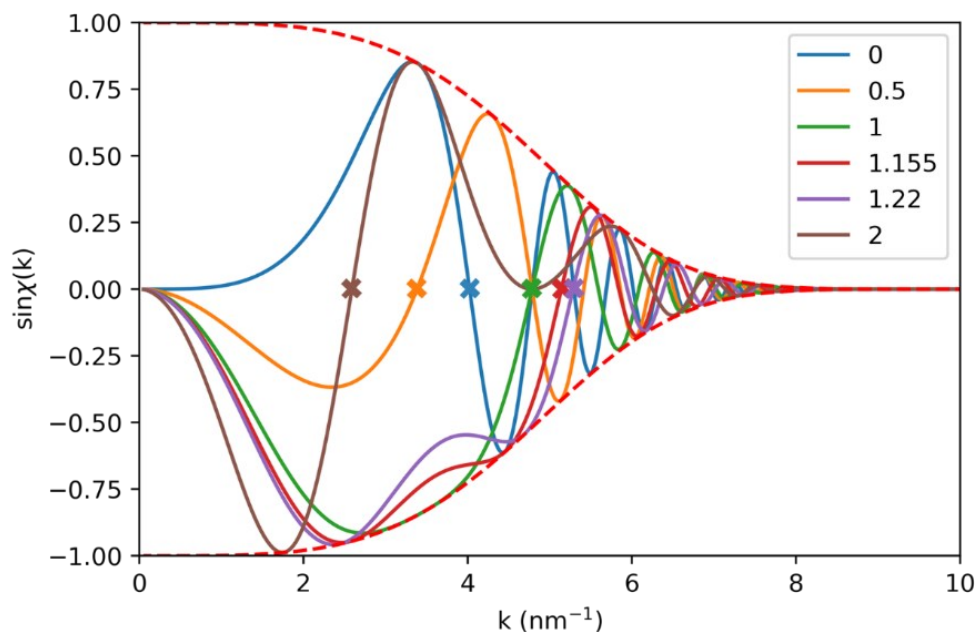
The actual contrast of the image is dependent of the variable part, that means,

$$C(\vec{r}) = 2\sigma_e V_t(\vec{r}) * \mathcal{F}[\sin\chi(\vec{r})] \quad \text{eq. 13}$$

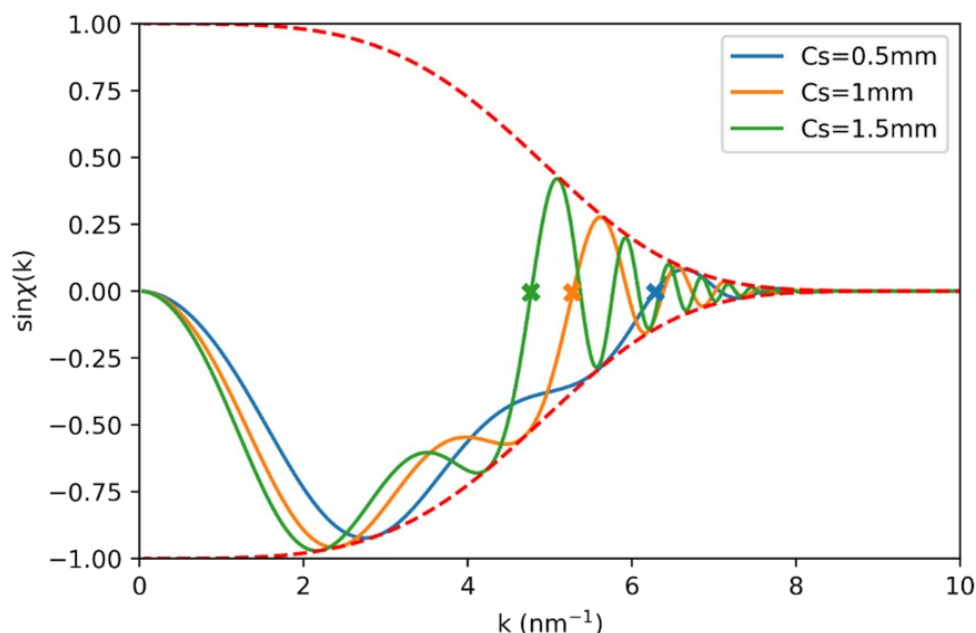
The contrast is mainly dependent of  $\sin\chi(\vec{r})$ , which is also the modified CTF. When the  $\sin\chi(\vec{r}) = -1$ , the band of CTF is the broadest and there are fewest zeros in comparison with other CTF. In a fixed spherical aberration  $C_s$  and the electron wavelength  $\lambda_e$ , the optimal defocus values can be found when  $d\chi/d\vec{r} = 0$  and  $\chi = -0.5(8N + 3)(\pi/2)$  the broadest passband at  $N = 0$ . After solving the equations, the optimal defocus value is:

$$\Delta f_{sch} = -\left(\frac{3}{2}C_s\lambda_e\right)^{\frac{1}{2}} \approx 1.22(C_s\lambda_e)^{\frac{1}{2}} \quad \text{eq. 14}$$

which is called Scherzer defocus<sup>150</sup>. The negative defocus means under focus that is the always defocus side people choose, because the ray is focused after passing through the object. In this condition, image solely represents the object, and the structure projection can be easily related to the image contrast. In a more competitive explanation, the CTF of  $-(C_s\lambda_e)^{\frac{1}{2}}$  can be plotted with coefficient under 300 keV accelerating voltage, convergence semi-angle ( $\alpha$ ) = 0.1 mrad, and  $C_s = 1$  mm (Figure 29). The purple line can reach the higher point resolution after comparing all 1<sup>st</sup> x-intersect, marked by the crosses. On the other hand, when the defocus is 0 (blue line), the contrast is reverse before its first x-intersect compared with purple line. That is called contrast reversal that is common when the conditions are changed, that imply the lattices can be dark or bright in the image. With the development of  $C_s$  correction technique, the point resolution can be further improved when the  $C_s$  value decreases under Scherzer defocus (Figure 30).



**Figure 29. Contrast transfer function with different coefficient of  $-(C_s\lambda_e)^{1/2}$  under 300 keV accelerating voltage,  $\alpha = 0.1$  mrad, and  $C_s = 1$  mm.**



**Figure 30. The impact of spherical aberration on contrast transfer function under Scherzer defocus.**

## 2.2. Introduction to scanning transmission electron microscopy

STEM utilizes convergence beam as a probe to scanning the region of interest by a scanning coil. The scattering between the electron probe and specimen is collected by different detector for further processing, including annular detector, energy-dispersive X-ray spectroscopy (EDS), EELS, 4D-STEM, and integrated differential phase contrast (iDPC). In terms of annular detector, the semi-collection angle ( $\beta$ ) of annular bright field (ABF) detector, annular dark field (ADF) detector, and high-angle annular dark field (HAADF) detector are normally  $< 10$  mrad,  $10 < \beta < 50$  mrad, and  $> 50$  mrad, respectively.

ABF image is mainly contributed by transmitted electron and scattering electron, that is beneficial to image light elements because of channeling effect<sup>151</sup>. The channeling effect is different from light elements and heavy elements. The scattering angle of light elements is small, and the scattering angle of heavy elements is large. Since most of the signals is from transmitted beam and scattering, the HRABF images would have a white background with the dark atoms, and the heavier atoms are darker (Figure 31).



ADF image is mainly contributed by diffraction beam followed Bragg's law, that provides solely diffraction contrast. In HAADF, the main contribution is from the incoherent scattering electrons for high scattering angles from the least dispersive and the most bounded states, for instance, 1s orbital<sup>152</sup>. The contribution of thickness to incoherent scattering is less, and the most interferences are averaged. Hence, the contrast of HAADF is mainly contributed by square of atomic number. Besides, the probe size reaches sub-Angstrom scale that provides high spatial resolution with high energy resolution. However, the imaging time is normally longer than TEM, that means much poor temporal resolution. Most importantly, atomic STEM images can be directly compared with the atomic model and crystal structure. In HRTEM, the exit wave reconstruction or image simulations needs to be computed to compare with the crystal structure.

The scattering is coherent in small scattering angle, for example BF. According to the reciprocity theorem<sup>152</sup>, the imaging principle of STEM is almost equivalent to that of TEM (Figure 32). In the mathematical description, the wavefunction after interaction between the probe and specimen in STEM can be denoted as,

$$\psi_i(\vec{r}) = e^{i\sigma_e V_t(\vec{r})} * \mathcal{F}^{-1} \left[ e^{-i\chi(\vec{k})} \right] \quad \text{eq. 15}$$

Here, the probe amplitude distribution function  $P(\vec{r})$  is introduced,

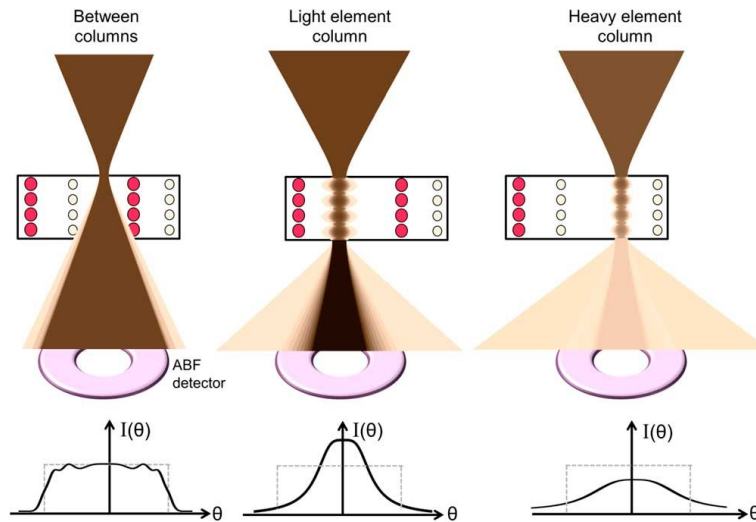
$$P(\vec{r}) = \mathcal{F}^{-1} \left[ e^{-i\chi(\vec{k})} \right] = \int e^{2\pi i \vec{k} \cdot \vec{r}} e^{-i\chi(\vec{k})} d\vec{k} \quad \text{eq. 16}$$

Hence, the bright field image intensity under WPOA in STEM is,

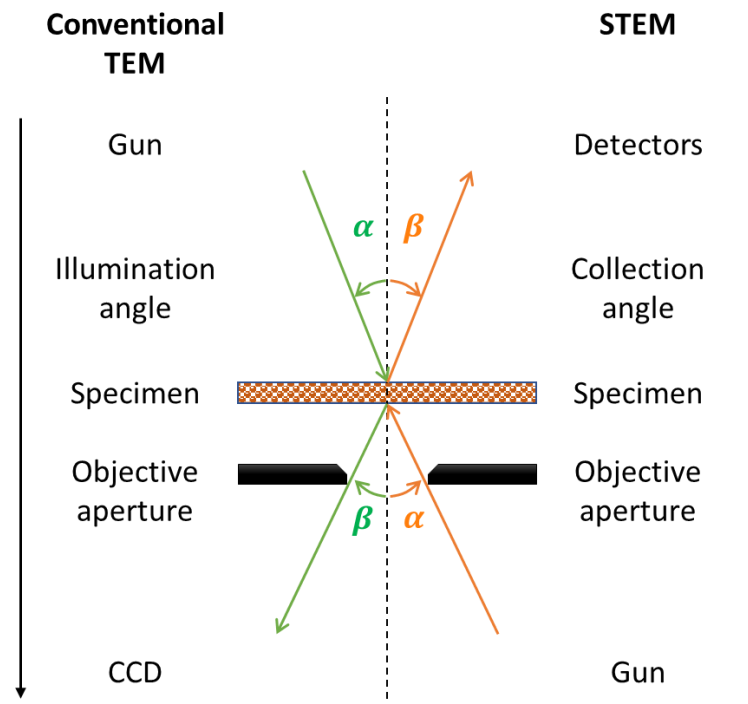
$$I_{BF} = |T(\vec{r}) * P(\vec{r})|^2 \quad \text{eq. 17}$$

that the square after convolution enlarges the intensity difference, and the contrast is still defined by the phases of the transfer function.





**Figure 31. Scheme of the imaging contrast of HRABF caused by channeling effect.** This image is reproduced from Ref. <sup>151</sup>.



**Figure 32. The scheme of reciprocity theorem between Conventional TEM and STEM for zero-loss images.**

When the scattering angle is larger, the image contrast becomes amplitude dominant rather than phase dominant. Assuming all of the scattering to be collected by the annular detector, the probe amplitude distribution function needs to consider the center of the probe in the scan coordinate ( $\vec{r}_0$ ). The wavefunction of the phase object is re-written as,



$$\psi_i(\vec{r}, \vec{r}_0) = T(\vec{r})P(\vec{r} - \vec{r}_0) \quad \text{eq. 18}$$

Then, the exit wave is,

$$\psi_i(\vec{k}_{all}) = \int e^{-2\pi i \vec{k}_{all} \cdot \vec{r}} T(\vec{r})P(\vec{r} - \vec{r}_0) d\vec{k}_{all} \quad \text{eq. 19}$$

where  $\vec{k}_{all}$  is all scattering angles. The image intensity can be integrated,

$$\begin{aligned} I(\vec{r}_0) &= \int \left| \int e^{-2\pi i \vec{k}_{all} \cdot \vec{r}} T(\vec{r})P(\vec{r} - \vec{r}_0) d\vec{r} \right|^2 d\vec{k}_{all} \\ &= \iiint T(\vec{r})P(\vec{r} - \vec{r}_0) T(\vec{r}')^* P(\vec{r}' - \vec{r}_0)^* e^{-2\pi i \vec{k}_{all} \cdot (\vec{r} - \vec{r}')} d\vec{r} d\vec{r}' d\vec{k}_{all} \\ &= \iint T(\vec{r})P(\vec{r} - \vec{r}_0) T(\vec{r}')^* P(\vec{r}' - \vec{r}_0)^* \delta(\vec{r} - \vec{r}') d\vec{r} d\vec{r}' \quad \text{eq. 20} \\ &= \int |T(\vec{r})|^2 |P(\vec{r} - \vec{r}_0)|^2 d\vec{r} \\ &= |T(\vec{r}_0)|^2 * |P(\vec{r}_0)|^2 \end{aligned}$$

As a result, the intensity variations of STEM image can be seen. The phase of the specimen and the probe are leveled before convolution. Thus, the image is no longer contrast reversal with focus in ADF-STEM. The contrast transfer function of TEM and STEM can be illustrated in Figure 33, that shows the difference between the phase dominant transfer function and intensity dominant transfer function under similar conditions<sup>153</sup>. The spatial resolution of STEM is much high than that of TEM under similar conditions without contrast reversal in different defocus.

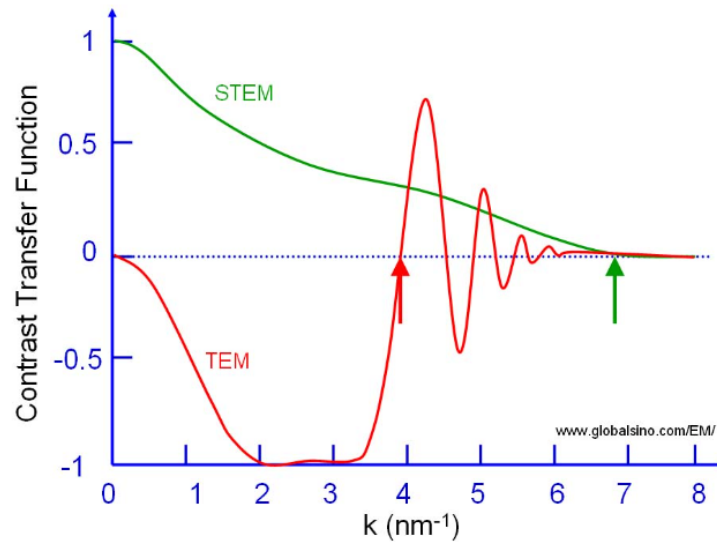
In scanning probe and the equations above, the resolution of STEM mainly depends on the probe size, and one simple way is to change the convergence semi-angle ( $\alpha$ ). The total probe size ( $d(\alpha)$ ) is the root summation square of the effective probe size ( $d_g \propto \alpha^{-1}$ ), the Cs broadening ( $d_s \propto \alpha^3$ ), and the diffraction limit ( $d_d \propto \alpha^{-1}$ ). There two terms are anti proportional to  $\alpha$  and one term is proportional to  $\alpha^3$ , so there should

be the optimal values for both  $d$  &  $\alpha$ . Scherzer provided the minimum probe size ( $d_{min}$ ) at the optimum convergence semi-angle ( $\alpha_{opt}$ ) as follows<sup>150,154</sup>,

$$d_{min} = 0.43C_s^{1/4}\lambda^{3/4} \quad \text{eq. 21}$$

$$\alpha_{opt} = (4\lambda/C_s)^{1/4} \quad \text{eq. 22}$$

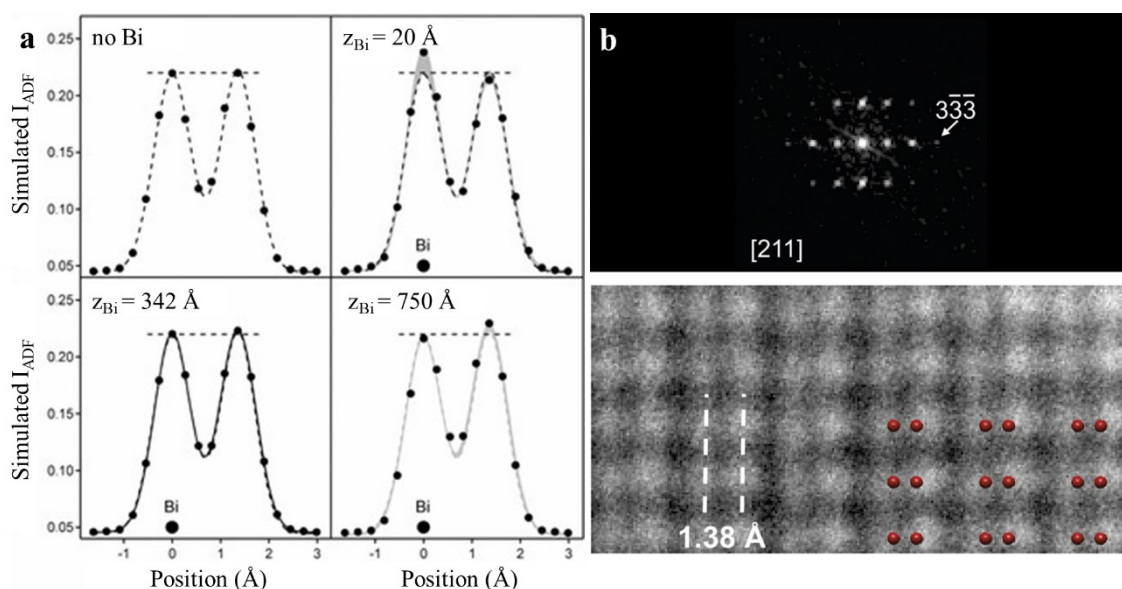
For 300 keV accelerating voltage with 0.05 mm  $C_s$ , the  $d_{min} = 60.08 \text{ pm}$  at the  $\alpha_{opt} = 19.92 \text{ mrad}$ .



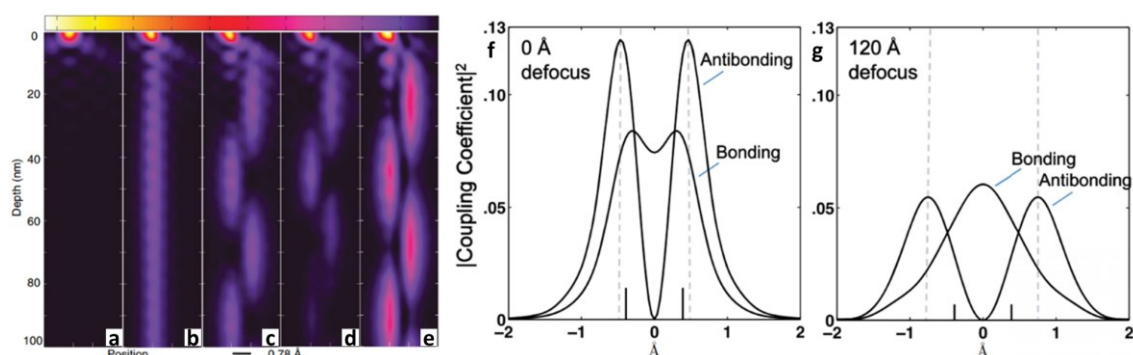
**Figure 33. Typical CTF of TEM and STEM under similar conditions.** This illustrate is reproduced from Ref. <sup>153</sup>.

Although STEM takes many advantages such as higher spatial resolution, and less post imaging processing, the images may be suffered by channeling effect if the thickness of specimen is too large. For example, a signal appears in the wrong atomic column<sup>155</sup>. a  $\langle 110 \rangle$  Silicon contains a single Bi atom at different depths (Figure 34). At depths 342 and 750 Å, the intensity of ADF-STEM fails to represent the actual Bi atom position. Another example is the adjacent Si atomic column broadening along  $\langle 211 \rangle$  (Figure 34e)<sup>156</sup>. The projection distance of  $\langle 211 \rangle$  adjacent Si should be 0.78 Å, but the measured distance is about 1.38 Å. The convergence probe is coupling with the eigenstates of the Si. The anti-bonding state separation is larger than the bonding state, and this time the probe is well

coupling with the anti-bonding state (Figure 35). The hopping of the electron probe is the reason why the Bi atom appear in the wrong position. As usual, the very thin specimens are always the best approach to study atomic structure with WPOA without other shortcoming problems.



**Figure 34. Examples of channeling effect in STEM.** **a**, Simulations of Cs-corrected ADF-STEM images of a  $\langle 110 \rangle$  Silicon with 758 Å thick contains a single Bi atom: no Bi, a Bi atom at depth = 20 Å, 342 Å, and 750 Å<sup>155</sup>. **b**, ADF-STEM image of Si along  $\langle 211 \rangle$  with corresponding FFT image<sup>156</sup>.



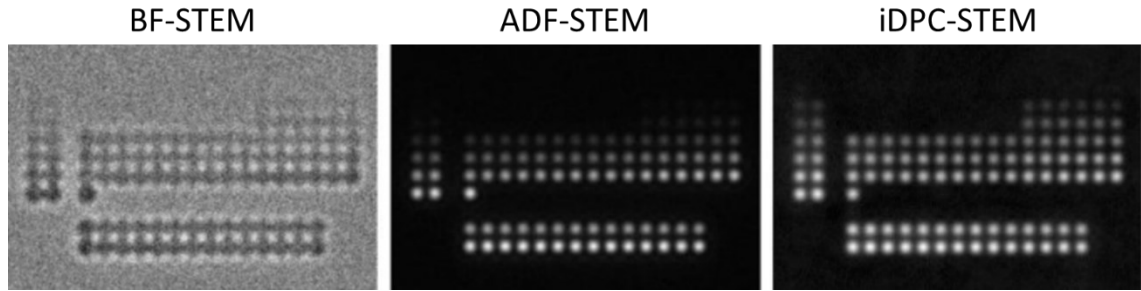
**Figure 35. The channeling effect affected electron probe coupling.** **a-d**, Multislice approach of the probability of propagation of an electron probe in different depth **(a)** in free space, **(b)** along a single isolated atomic column, **(c)** along two atomic columns, and **(d)** along two atomic columns with a full lattice. **e**, Same condition of **(d)** but using analytic tight-binding approach. **f,g**, The coupling amplitudes of the antibonding and bonding states at **(f)** 0 Å defocus, and **(g)** 120 Å defocus<sup>156</sup>.



### 2.3. Introduction to integrated differential phase contrast

iDPC is an imaging technique which is developed from 4D-STEM by using linearity approach<sup>157</sup>, since a set of 1024 x 1024 pixels 4D-STEM data requires over 2 TB storage for a total 1048576 convergent beam electron diffraction (CBED) patterns with 16/32 bits dynamic range. That is a huge challenge not only for data storage and acquisition duration, but also for data analysis<sup>158</sup>. Instead of using a pixelated detector, iDPC acquires images by a segmented BF or/and ADF detector to determine the center of mass (COM) of the deflected probe, center of the CBED pattern, caused by the scattering. Normally, iDPC imaging requires at least 4 segmented ADF detector, and there are 8 segments and 16 segments for more accurate calculations.

In comparisons between BF-STEM, ADF-STEM, and iDPC-STEM, the images of atom number from 1-103 single atoms were simulated by Dr. Ivan Lazić *et al.*<sup>157</sup> (Figure 36). Different from the contrast of ADF-STEM proportional to approximately  $Z^2$ , the contrast of iDPC-STEM is proportional approximately to  $Z$ . Thus, more light elements can be seen with heavy elements in the same picture. However, the drawback is the contrast between similar atomic number in iDPC-STEM is barely distinguishable. Although BF-STEM can also show the light elements, the signal-to-noise ratio (SNR) is worse than iDPC-STEM. Due to the fast enough acquisition time,  $Z$ -contrast, and potential-electric field-charge density distribution relations utilization, low dose imaging can be achieved to capture dose sensitive materials. For example, low atomic number elements<sup>159</sup>, even Hydrogen<sup>103</sup>, metal-organic frameworks (MOFs)<sup>109,110</sup>, perovskite<sup>160</sup>, and virus<sup>161</sup>.



**Figure 36.** The simulated image contrast of single atoms from  $Z = 1-103$  for BF-, ADF-, and iDPC-STEM<sup>157</sup>.

Assuming the probe is much smaller than the feature size, the specimen potential can be smoothly distributed and can be described by linearity. Due to the conservative of electrostatic field, the specimen potential can be related to electrostatic field<sup>157</sup>,

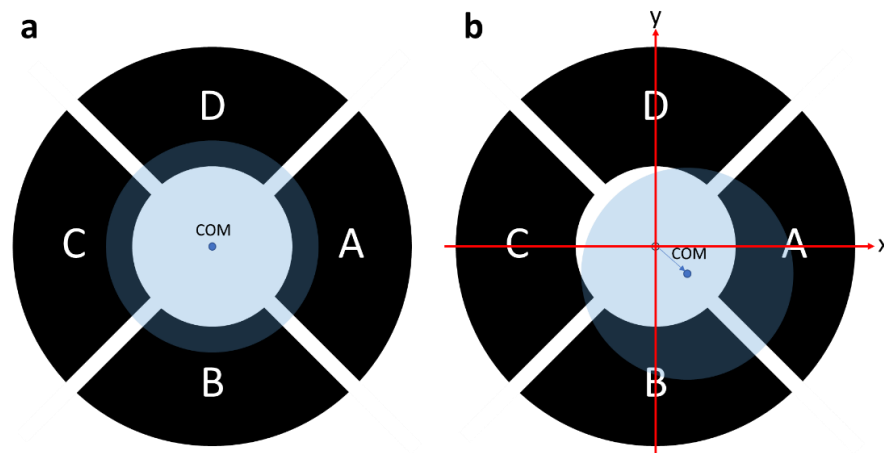
$$\vec{E}(\vec{r}) = -\nabla V(\vec{r}) \quad \text{eq. 23}$$

Using 4 segmented ADF detector as an example (Figure 37), where the COM is moved, the electrostatic field measured by the segmented detector can be denoted as,

$$-E_x = \partial V / \partial x = A - C \quad \text{eq. 24}$$

$$-E_y = \partial V / \partial y = B - D \quad \text{eq. 25}$$

Via the asymmetric scattering signals hitting to the segmented detector, the center of mass can be estimated. The further signal processing can further extract the useful information such as electric field, and charge density.



**Figure 37.** Schematics of the determination of COM. **a,b**, the incident beam interacts (a) without specimen potential and (b) with specimen potential.



Due to the symmetry and linearity, the imaginary part is independent of the position of the probe ( $\vec{r}_0$ )<sup>157</sup>. The intensity of differential phase contrast (DPC) can be written as,

$$I^{DPC}(\vec{r}_0) = -\frac{l_c \lambda_e}{2\pi} \left( |P(\vec{r})|^2 \star \sigma \vec{E}(\vec{r}) \right) (\vec{r}_0) \quad \text{eq. 26}$$

where  $l_c$  is the camera length. The image intensity is from the cross-correlation between the intensity of the probe and the electric field. Considering the electrostatic field and the intensity of iDPC,

$$\begin{aligned} \nabla I^{iDPC}(\vec{r}_0) &= I^{DPC}(\vec{r}_0) = \frac{l_c \lambda_e}{2\pi} \left( |P(\vec{r})|^2 \star \sigma \nabla V(\vec{r}) \right) (\vec{r}_0) \\ I^{iDPC}(\vec{r}_0) &= \frac{l_c \lambda_e}{2\pi} \left( |P(\vec{r})|^2 \star \sigma V(\vec{r}) \right) (\vec{r}_0) \end{aligned} \quad \text{eq. 27}$$

Also, the relationship between specimen potential, electrostatic field, and charge density distribution ( $\rho(\vec{r})$ ) can be described by Gauss's law and Poisson Equation<sup>162</sup>.

$$\nabla^2 V(\vec{r}) = \Delta V(\vec{r}) = -\nabla \cdot \vec{E}(\vec{r}) = -\frac{\rho(\vec{r})}{\epsilon_0} \quad \text{eq. 28}$$

where  $\epsilon_0$  is the permittivity in free space. So, the intensity of dDPC is,

$$\begin{aligned} I^{dDPC}(\vec{r}_0) &= \nabla^2 I^{iDPC}(\vec{r}_0) = \nabla I^{DPC}(\vec{r}_0) \\ &= -\frac{l_c \lambda_e}{2\pi} \left( |P(\vec{r})|^2 \star \frac{\sigma \rho(\vec{r})}{\epsilon_0} \right) (\vec{r}_0) \end{aligned} \quad \text{eq. 29}$$

Thus, the study of electric field, magnetic field, potential difference, and charge density distribution can be achieved by using iDPC-STEM.

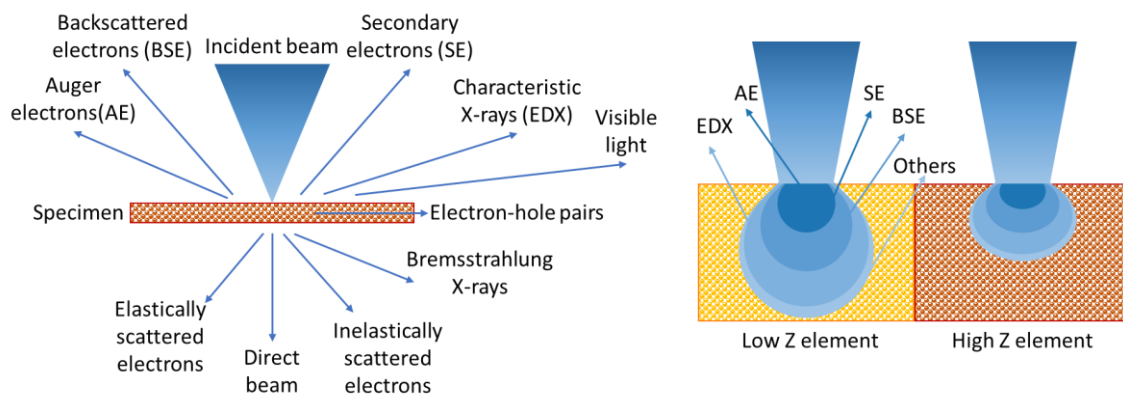
## 2.4. Introduction of energy dispersive x-ray spectroscopy

Other than imaging, STEM can simultaneously collect composition data to achieve mapping. As mentioned before, the electrostatic interaction between the high

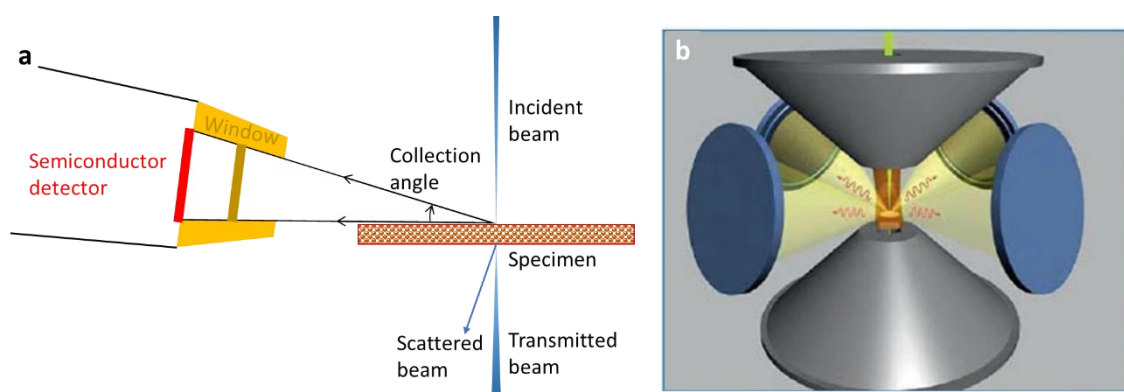




energy incident beam and specimen generates different kinds of signals, for example characteristic X-ray (Figure 38). Each element has their unique spectrum of characteristic X-ray likes fingerprint. The high energy incident beam causes the excited electron from low energy state to high energy state, that make an electron-hole in the inner shell. The characteristic X-ray is emitted by filling the electron from outer shell (high energy state) to inner shell (low energy state)<sup>163</sup>. This characteristic X-ray contains photon energies. These photon energies can be collected semiconductor detectors, such as lithium-drifted silicon or germanium detector, and converted to voltage pulse intensities. A conventional EDS uses several micrometers beryllium (Be) window, which is high transmissivity to X-ray, before the semiconductor-based detector to protect the detector without condensation and contamination (Figure 39a). The drawback of this thick window is that the light elements, before Na ( $Z < 11$ ), are filtered<sup>153</sup>. If the Be window is replaced as the atmospheric thin window (several hundred nanometers) or windowless, the detectable element is down to Li ( $Z = 3$ ). However, the required interaction volume of low  $Z$  elements is larger than high  $Z$  elements, that means the thickness is required sufficient thick for detecting low  $Z$  elements (Figure 38). However, the efficiency of EDS is still too low. In order to increase the efficiency, four symmetric Si drifted detectors with larger collection angle are designed to collect characteristic X-ray simultaneously (Figure 39b). Atomic EDS mapping can be achieved for thick and stable specimen<sup>164-166</sup>. Although the insufficient efficiency and low energy resolution, EDS is still a powerful tool to monitor synthesis, catalysis, and failure analysis.



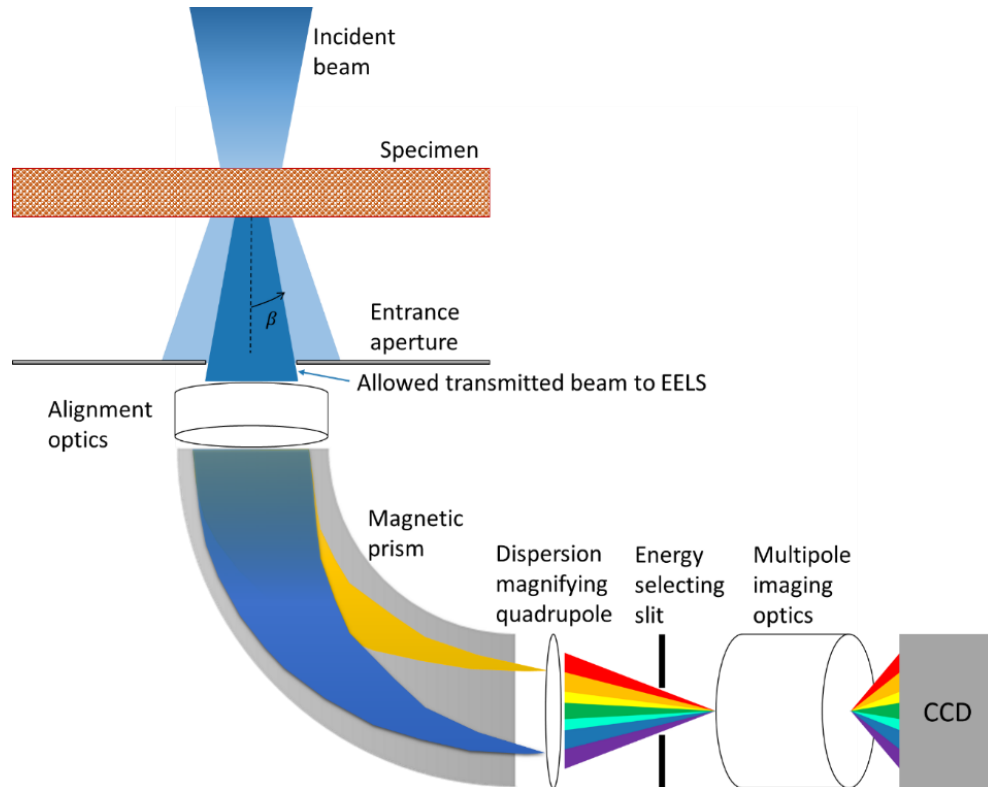
**Figure 38. Signals generated by the interactions between a high-energy electron beam with a thin specimen.**



**Figure 39. Schematics of EDS. a, A conventional EDS. b, Latest model of the four silicon drift detectors. b is reproduced from Ref. <sup>165</sup>.**

## 2.5. Introduction to electron energy loss spectroscopy

EELS has a higher collection efficiency and energy resolution in comparison with EDS. In addition, EELS is also allowed to distinguish majority elements including Hydrogen, which is recorded in EELS atlas, a standard EELS spectrum for the most elements<sup>56</sup>. As mentioned in 2.4, the Coulomb interactions between incident beam and specimen generate many signals, and those signals can be mainly classified as two categories: elastic and inelastic scattering. Both of their direction of momentum is changed, and the energy is transferred. However, elastic scattering is considered as no energy loss during collision, so EELS mainly utilizes inelastic scattering to achieve structural analysis, including valence state, and composition analysis<sup>56</sup>.



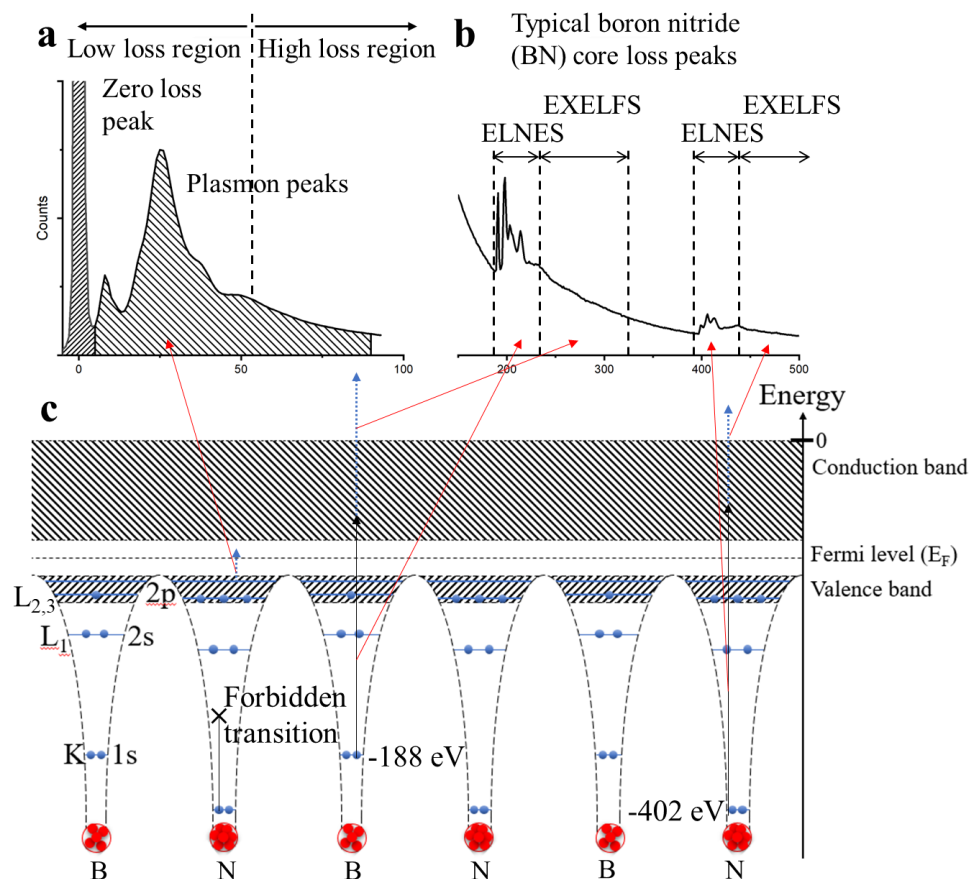
**Figure 40. Schematic of electron energy loss spectroscopy with beam propagations.**

The configuration of EELS is shown in Figure 40. The scattered transmitted beam after passing through an entrance aperture (several millimeters) propagates to the magnetic prism. The electrons are rotated under magnetic field, and the radius of curvature  $R$  is denoted as<sup>167</sup>,

$$R = \left( \frac{m_0 v_e}{qB} \right) \left( 1 - \frac{v_e^2}{c^2} \right)^{-\frac{1}{2}} \quad \text{eq. 30}$$

where  $m_0$  is the rest mass of an electron,  $v_e$  is the velocity of an electron,  $q$  is the elementary charge,  $B$  is the magnitude of magnetic field, and  $c$  is the speed of light. According to eq. 30, the different velocity of electron caused by the different energy loss would undergo a different radius of curvature, thus undergo a different angular deflection. As a results, the beam is eventually focused. Then, the beam can be imaged by a CCD after passing through the dispersion magnifying quadrupole, energy selecting slit, and multipole imaging optics (mixed with quadrupole and sextupole lenses).

Figure 41 shows the contributions of the excitation energies by using boron nitride (BN) as an example, which extracted from EELS atlas. Zero loss is contributed by direct beam and elastic scattering. The main function of zero loss peak is calibration. The desired zero loss peak is sharp and narrow. The sharpness of peak indicates the direct beam is well aligned with the center of entrance aperture, and the full width half maximum (FWHM) is the indicator of the energy resolution. Via dual-EELS, both zero loss and core loss can be simultaneously measured. Hence, the drift of spectra during measurement can be realigned and the zero loss can be also used to remove the contribution of plural scattering for thick specimen.



**Figure 41. Schematics of EELS.** **a**, The region of low loss and high loss region, including the zero loss peak and plasmon peaks. **b**, A typical core loss peaks for boron nitride (BN). **c**, An example energy band diagram of BN with the contributions of different excitation to the spectra in (a,b), including plasmon, energy loss near edge structure (ELNES), and extended energy loss fine structure (EXELFS). The scale of energy in (c) is non-linear.



In the low loss region (normally 0-50 eV), other than zero loss, there are plasmon contribution. The plasmon contribution in EELS is from the excitation from valence band to conduction band. By using the log ratio of the integration of zero loss and plasmon contribution, the specimen thickness ( $t$ ) can be estimated by EELS called log-ratio method<sup>167</sup>,

$$t/\lambda_{MFP} = \ln (I_P/I_0) \quad \text{eq. 31}$$

where  $\lambda_{MFP}$  is the effective mean free path (MFP) of inelastic scattering,  $I_P$  is the integration of the plasmon, and  $I_0$  is the integration of zero loss peak. The integration range is set in a reasonable range (normally up to 100 eV is sufficient for plasmon integration). This method is valid for  $0.1 < t/\lambda_{MFP} < 5$ . If the log-ratio is too small or too large, in other words, the specimen is too thin or too thick, the other estimation methods are required. Further, thickness map can be conducted.

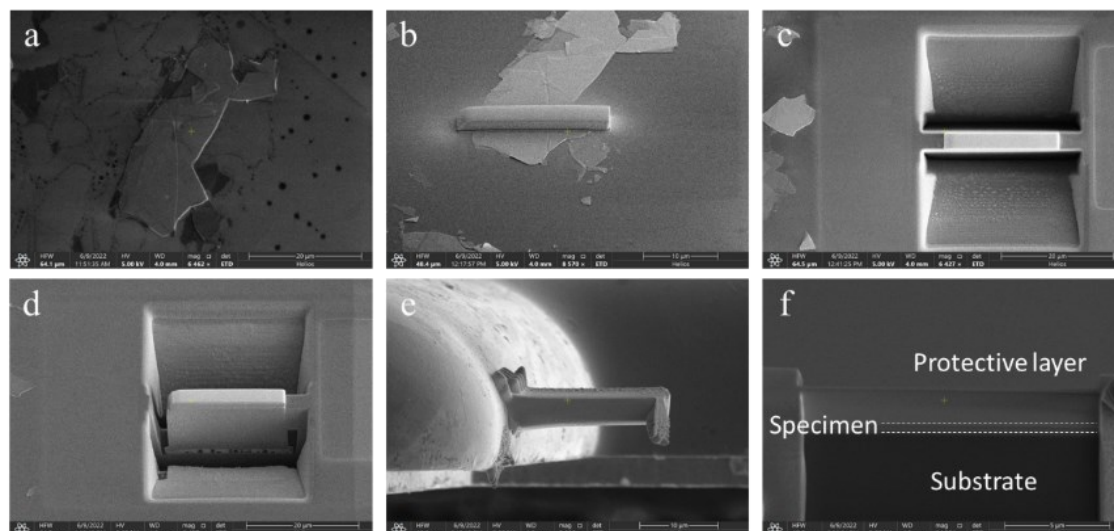
When the energy loss is larger than 50 eV, this is called high loss region or core loss region. In terms of energy loss near edge structure (ELNES), the signals are from the excitation of K, L, M, N shells to the conduction band (Figure 41b-c). Those transitions follow selection rules<sup>168</sup>. ELNES provides informative characteristic properties of the specimen, including identification of elements<sup>56</sup>, chemical state<sup>54,169</sup>, type of bonding<sup>54</sup>, and spinning<sup>170</sup> etc. In the perspectives of extended energy loss fine structure (EXELFS), the signals are caused by the ejection of the low kinetic energy electrons. EXELFS is capable for short-range order structural analysis for both crystalline and amorphous, for instance interatomic distances<sup>171</sup>. Due to the signals of EXELFS are weak and the data analysis is complex, this technique is rarely used.



## 2.6. Specimen preparations

The specimens mainly prepared by CVD and mechanical exfoliations. For CVD specimens, it is now impossible to grow the 2D materials directly onto the TEM grid. The common substrate such as copper, mica, and sapphire etc. are used to grow the 2D materials. Then, poly(methyl methacrylate) (PMMA) transfer method<sup>172</sup> was implemented to transfer the specimen onto the TEM grid. The PMMA first acts as the supporting and protective layer coated on the specimen. Then, the chosen etchant that can etch the substrate without damaging the specimen. After that, TEM grid is used to pick up the floating PMMA/specimen. Finally, the specimen on TEM grid can be collected by cleaning the PMMA by acetone. For the mechanical exfoliated specimen, the specimens were transferred by thermal release tape method<sup>173</sup>. The thermal release tape was directly attached onto an exfoliated specimen, followed by transferring it onto TEM grid. Finally, a heater was applied to remove the thermal release tape.

The cross-section specimens were prepared by focused ion beam (FIB) method<sup>174</sup>. A practice was recorded by using Helios 5 CX in Figure 42. A metal nanoparticles protective layer was first deposited on to the target position (Figure 42a-b). Then, digging two symmetric big holes on both sides of the specimen that made sure the substrate could be cut by Ga ion beam and a handle of the specimen was left (Figure 42c-d). The specimen was transferred to a half grid by a tungsten tip that connected to the protective layer on the specimen by deposition. The connection between the tip was removed by Ga ion beam after the specimen was attached on the half grid by deposition (Figure 42e). The final product is shown in Figure 42f. The thinning specimen can be done by Ga ion beam (thickness < 100 nm). The further optimal thinning specimen can be done by Fischione NanoMill 1040 (thickness < 20 nm).



**Figure 42. FIB procedure of a practice.** **a**, Locating specimen. **b**, Deposition of protective layer. **c**, Digging two big holes by Ga ion beam. **d**, Leaving a handle on a side. **e**, Transferring the specimen to half grid. **f**, The low magnification image of the cross-section specimen.

## 2.7. *In situ* AFM tip preparations

The tungsten tip used in *in situ* experiment for Nanofactory<sup>TM</sup> holder was made by the chemical etching method<sup>175</sup>. 1 M NaOH solution with 6 V direct current was used to prepare tungsten tip. The etched tips were collected by dropping either into ethanol or onto a container.

## 2.8. Summary

In this chapter, the milestone of TEM, principle with mathematics derivation, and specimens as well as tools preparations have been introduced briefly. There are still lots of techniques can be discussed, for example, 4D-STEM. However, it does not apply in this thesis. In the following chapters, the experimental results will be demonstrated to solve the research questions, raised from Chapter 1.





## Chapter 3. Unveiling the Nucleation and Growth Kinetics of Rhenium Diselenide

In this chapter, the critical research question of chemical vapor deposition (CVD) of the two-dimensional (2D) Rhenium diselenide ( $\text{ReSe}_2$ ) has been resolved: what are the intermediate reactants and species during CVD growth? Many atomistic simulations (Density functional theory (DFT), Molecular dynamics (MD), Monte Carlo, etc) have given different viewpoints/routes of the chemical reactions for 2D growth in previous investigations. Experiment results are particularly crucial to validate the simulated growth mechanisms. Unfortunately, up to now, all the experiments failed to provide unambiguous, direct, and atomic-scale insights and evidences for the intermediate growth species in the CVD chamber (atmosphere) as well as on the growth substrates, during the 2D transition metal dichalcogenides (TMDCs) growth.

Via high-angle annular dark-field (HAADF)-scanning transmission electron microscopy (STEM) and electron energy loss spectroscopy (EELS), the direct observation in atomic scale has been achieved as follows: (1) The intermediate metal chalcogenide molecular clusters attached the growth fronts. (2) The crystal nuclei as small as sub-1 nm in size. (3) The cluster agglomerates which retard uniform 2D growth.

The significances of these findings as follows: (1) Atomic insights into growth unveiled will direct further selection of precursors and promoters. (2) Function of  $\text{H}_2$  environment is rationalized, the need of  $\text{H}_2$  is related to the reduction of agglomeration of growth clusters and enhancement of product quality. (3) It is known the atomic defects in



as-grown 2D layer can easily anchor molecular clusters (even for single cluster) and serve as nuclei for epilayer growth, interrupting the layer-by-layer (2D) growth.

### 3.1. Introduction

Two-dimensional (2D) transition metal dichalcogenides (TMDCs) hold promise for new generation semiconductor device applications<sup>176</sup>. Due to the superior growth speed and relatively low cost, chemical vapor deposition (CVD) is the most common synthesis method in the semiconductor industry at present<sup>177-179</sup>. However, as the greatest challenge in CVD growth of 2D TMDCs, inaccessibility of accurate thickness control and perfect layer-by-layer growth, is retarding further technological advances<sup>180</sup>. Although the thickness of 2D TMDCs can be controlled in CVD synthesis<sup>181</sup>, and a number of precursors, including the metal oxides and chalcogenides for atmospheric pressure/low-pressure CVD (APCVD/LPCVD)<sup>182</sup>, the metalorganics for metal-organic CVD (MOCVD)<sup>183</sup>, space-confined method of TMDCs under graphene on Au quantifoils<sup>184</sup>, solvent evaporation techniques<sup>185</sup>, and different temperatures/pressures/substrates have been deployed in the CVD of 2D TMDCs in previous works<sup>86</sup>, the control on the morphology of 2D TMDCs remain unresolved. The reaction sites, mass transportation pathways, and intermediate species involved in growth are still under hot debate<sup>91</sup>. Undoubtedly, the clarification of kinetic reaction mechanisms of CVD growth of 2D TMDCs will greatly benefit the synthesis, in terms of product quality and reproducibility, and will further influence widely the relevant application fields<sup>186</sup>.

Although the precursors of CVD of TMDCs, and the structures of 2D TMDCs are well known<sup>187</sup>, the reaction kinetics in vapor or on solid surfaces<sup>188</sup> in the CVD process are not well understood yet. Contradictory growth mechanisms have been proposed



previously, mostly through simulations, such as reactions on oxide surfaces<sup>189</sup>, intermediate  $\text{MO}_x\text{X}_y$  (M = transition metal, O = oxygen, X = chalcogenide) clusters<sup>89</sup>,  $\text{MX}_2$  clusters (M = transition metal, X = chalcogenide)<sup>190,191</sup>, etc. The above reaction paths could impose different energy barriers for nucleation and growth, which may lead to inhomogeneities, defects, and other nonequilibrium structures. To date, it remains difficult to achieve strict Frank-van der Merwe (FM) layer-by-layer growth of 2D TMDCs by CVD<sup>192</sup>, similarly for other atomically-thin 2D films<sup>193,194</sup>. In the case of 2D TMDCs, it has been noted the anchoring of the precursors from vapor is crucial for TMDCs growth<sup>195,196</sup>. The subsequent reactions and growth kinetics involve uncertain intermediate stages<sup>91</sup>. The speculated or simulated growth mechanisms need experimental verifications<sup>197,198</sup>. Owing to the ultrathin thickness of 2D layers and restrictions on the CVD facility, normally it is hard to experimentally probe the reactants or species in the ongoing CVD chambers. However, the intermediate stages during growth can be “frozen” and studied *ex situ*.

In this work, atomic-scale scanning transmission electron microscopy (STEM) to capture the intermediate clusters and cluster complexes during CVD growth of 2D rhenium diselenide ( $\text{ReSe}_2$ ) has been employed. These molecular clusters play critical roles in edge (growth front/reactive sites) growth as well as the nucleation process. Moreover, the agglomerated or linked cluster complexes are found, and they become even more stable than individual clusters and will retard/prohibit the completion of growth for 2D full films. In this regard, a reductive hydrogen atmosphere is helpful for full film growth as it can accelerate the rate control steps (selenization of the cluster) and suppress cluster agglomeration. In view of the stability and popularity of metal chalcogenide clusters ( $\text{M}_x\text{X}_{2x-n}$ , e.g.,  $\text{M}_6\text{X}_8$  and  $\text{M}_4\text{X}_6$ , M = Mo, W, Re; X = Se, Te)<sup>199-201</sup>, HAADF-



STEM direct observations suggested that the attachment, transport, and agglomeration of intermediate chalcogenide clusters are essential steps in CVD synthesis of 2D TMDCs.

### 3.2. Methodology

In this session,  $\text{ReSe}_2$  were prepared with a variable of hydrogen gas flow from 1-5 sccm during CVD growth. Before atomic characterizations, Photoluminescence spectroscopy, Raman spectroscopy and atomic force microscopy (AFM) were used to conduct preliminary structural analysis, including the size of by-products, cleanness, size, shape, thickness, and peak shift. At the end, atomic resolution STEM was applied to characterize the actual structure of the specimens. Combining with the results of DFT simulation, the structure and the growth kinetics can be summarized. The details of the experimental method are recorded in below.

#### 3.2.1. Rhenium diselenide preparations

All chemicals were utilized as received without further processing. Ammonium perrhenate ( $\text{NH}_4\text{ReO}_4$ , Sigma-Aldrich,  $\geq 99.999\%$ ) and selenium (Sigma-Aldrich,  $\geq 99.99\%$ ) were acting as precursors and c-face sapphires were used as substrate. A4 liquid Poly(methyl methacrylate) (PMMA) was employed as the transfer medium and potassium hydroxide solution (KOH, Honeywell,  $\geq 85\%$ ) was used for detaching. Acetone (AQA,  $\geq 99.5\%$ ) was used for PMMA removal after transfer. Ultrapure water was produced by a Milli-Q water purification system.

The  $\text{ReSe}_2$  flakes were grown on a c-face sapphire in an atmospheric CVD system with double heating zones. Initially, 1.5 mg of  $\text{NH}_4\text{ReO}_4$  was sprayed in the quartz boat in the center of the downstream zone and 10.0 mg of selenium source was placed in another quartz boat in the center of the upstream zone. A 1 cm  $\times$  1 cm c-face sapphire



facing downward toward crushed molecular sieves was placed above the Re source. Argon gas (300 sccm) was pumped into the quartz tube for 10 min prior to the beginning of the heating program. Then the upstream zone was heated up to 400 °C at 20 °C min<sup>-1</sup> and held for 10 min. Simultaneously, the downstream zone was heated at 34 °C min<sup>-1</sup> up to 700 °C and held for 10 min. During the growth, the argon gas flow was adjusted to 80 sccm and hydrogen gas flow was set at 1–5 sccm. Selenium vapor was carried by Argon and hydrogen gas onto the c-face sapphire substrate. Both zones cooled down naturally right at the completion of the heating program.

The c-face sapphire substrate with as-grown ReSe<sub>2</sub> was first spin-coated with 1–2 drops of PMMA at 800 r.p.m. min<sup>-1</sup> for 10 s followed by 3000 r.p.m. min<sup>-1</sup> for 1 min. Then the as-formed PMMA/ReSe<sub>2</sub> film was detached from the c-face sapphire substrate by floating on 75 °C 1 mol L<sup>-1</sup> KOH for 20–30 min. Subsequently, the PMMA/ReSe<sub>2</sub> film floated on ultrapure water for washing, 3 times, each time for 10 min. Next, the PMMA/ReSe<sub>2</sub> film was coated onto a Quantifoil TEM grid and after 2 h of natural drying, the PMMA film was carefully etched away by acetone vapor.

### 3.2.2. Topographical measurement

The as-grown ReSe<sub>2</sub> on the c-face sapphire substrate was first observed using an optical microscope (ZEISS Imager.A2m) under bright field, dark field, and polarization light of 70° and 110°, which illustrated ReSe<sub>2</sub> flake distribution and the inner subdomains of each flake. Then atomic force microscopy (HITACHI, AFM5300E) was applied to check the morphological information of ReSe<sub>2</sub>, employing an SI-DF40P2 silicon tip (Hitachi).



### 3.2.3. Optical characterizations

Photoluminescence (PL) spectroscopy (Renishaw, inVia confocal) was employed to detect the optical properties of as-grown ReSe<sub>2</sub>. The laser wavelength is 633 nm, with a grating of 1800 g/mm. The signals were collected under a 50X lens (0.75 N.A.) and the laser spatial resolution was around 1  $\mu$ m. The laser power is 0.6 mW and for each single spectrum measurement, the exposure time is 10 s.

The angle-resolved Raman measurement was conducted at an excitation wavelength of 785 nm with a grating of 1200 g/mm, under a 50X lens (0.75 N.A.). The polarized Raman setup includes a motorized half-wave plate, a half-wave plate, and a linear polarizer. The Raman signals were collected at 0 and 70° rotation of incident polarized light. Scattered light goes to the CCD through the half-wave plate and a linear polarizer.

### 3.2.4. Transmission electron microscopy and imaging simulations

The high-resolution TEM and STEM morphological images, high-resolution STEM-HAADF images, and EELS spectra were obtained using a JEM-ARM200F TEM instrument equipped with a CEOS spherical aberration (Cs) (probe) corrector working under 60 kV. The beam current is 0.3 pA/nm and the beam probe size is 1.5 Å. Average background subtracting filtering (ABSF) is applied to reduce the noise of STEM-HAADF images. The EELS acquisition is completed with the Gatan Quantum, beam probe size ca. 1.5 Å, convergence angle 29 mrad, collection angle 35 mrad, and exposure time 2 s are applied. The STEM-HAADF image simulations are completed using QSTEM software with the same set of conditions as STEM experiments. The defocus and the spherical



aberration are set as Scherzer focus and 1  $\mu\text{m}$ , respectively. The other settings remain default.

### 3.2.5. Density functional theory simulation

Spin-polarized density function theory (DFT) calculations are performed using the Vienna ab initio Simulation Package (VASP) program package<sup>202,203</sup> within the projector augmented wave (PAW)<sup>204</sup> to explore geometries and electronic properties of  $\text{ReS}_2$ . The exchange–correlation interactions are described with the generalized gradient approximation (GGA)<sup>205</sup> in the form of the Perdew, Burke, and Ernzerhof (PBE) functional<sup>206</sup>. The kinetic energy cutoff for the plane-wave basis set is chosen as 450 eV, and the distance of the vacuum layer is set to be more than 20 Å, which is sufficiently large to avoid interlayer interactions. The DFT-D3 scheme of Grimme for the vdW correction<sup>207</sup> is applied on 2D  $\text{ReSe}_2$ . The pristine slab contains 96 Re and 216 Se atoms. The electronic SCF tolerance is set to  $10^{-5}$  eV. Fully relaxed geometries and lattice constant are obtained by optimizing all atomic positions until the Hellmann–Feynman forces are less than 0.03 eV/Å with the  $\Gamma$  point sampling.

## 3.3. Results and discussion

In the following, results and discussion are divided into three parts: 2D  $\text{ReSe}_2$  morphology and characterization, Identification of RexSey molecular clusters, and Key reactions and intermediate steps involved in growth. In the first part, microscale images show the influence of the hydrogen flow rate to the cleanness, uniformity and size of the CVD grown  $\text{ReSe}_2$ . With the increasing hydrogen flow rate, the uniformity and cleanness are also improved. The PL peaks are shifted with the different conditions, and the size of clusters' agglomerations as well as the Raman peaks intensity of  $E_g$  like peaks are anti-

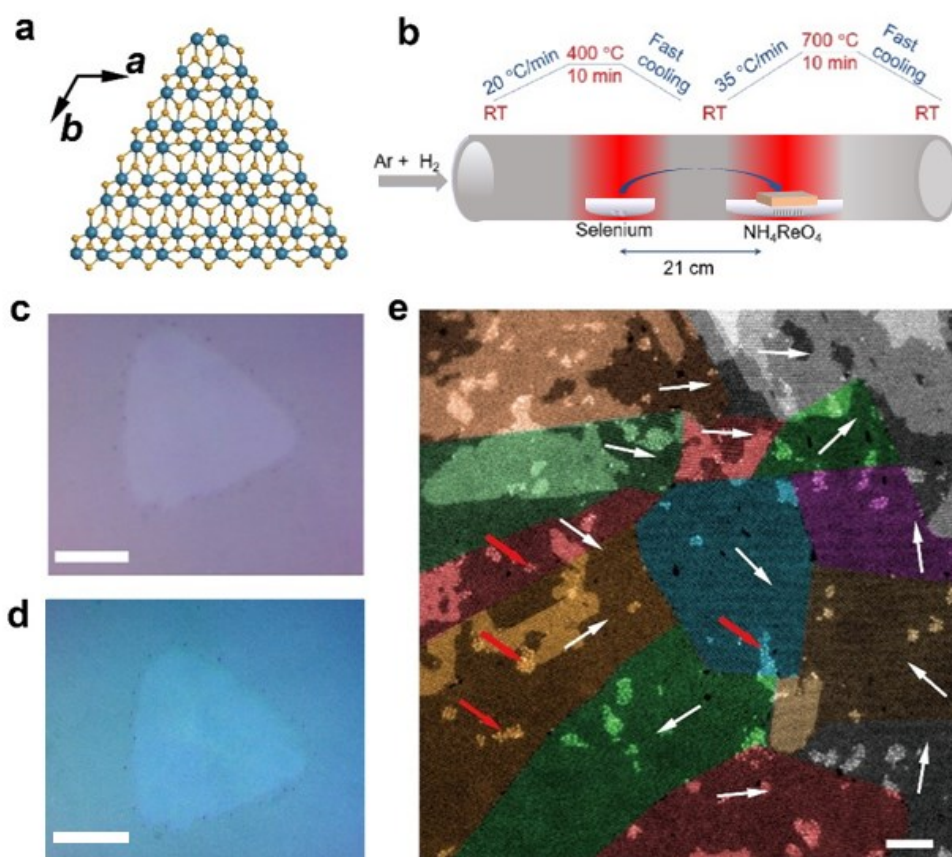




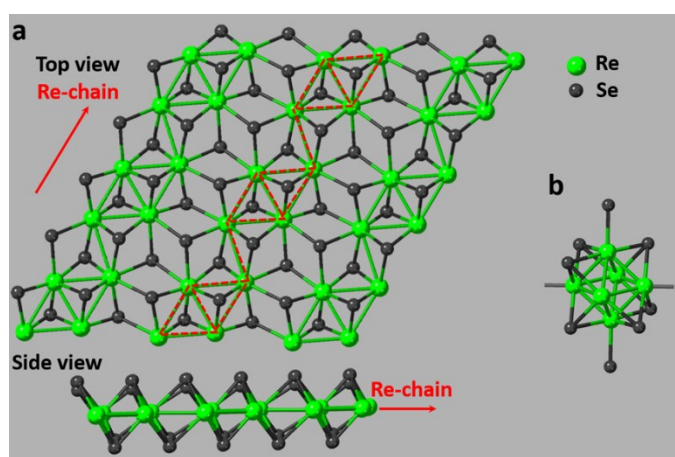
proportional to the hydrogen flow rate. In the second part, atomic HAADF-STEM images well display the structure of the clusters in different rotation, and EELS indicates the chemical formations differences between layered  $\text{ReSe}_2$  and  $\text{Re}_6\text{Se}_8$  clusters. In the third part, the summary of direct observations and theoretical calculations unveils the  $\text{Re}_6\text{Se}_8$  clusters as the intermediate species. The clusters are stable and mobile in atmosphere. The clusters tend to attach to the edge of  $\vec{a}$  directions rather than  $\vec{b}$  direction because that is more energy favorable in the attach step, and also the conversion step from  $\text{Re}_6\text{Se}_8$  clusters to 2D  $\text{ReSe}_2$ . Besides, hydrogen is the key to aid not only the reduction reactions of the clusters' formation, but also the conversion step in APCVD.

### 3.3.1. 2D $\text{ReSe}_2$ morphology and characterization

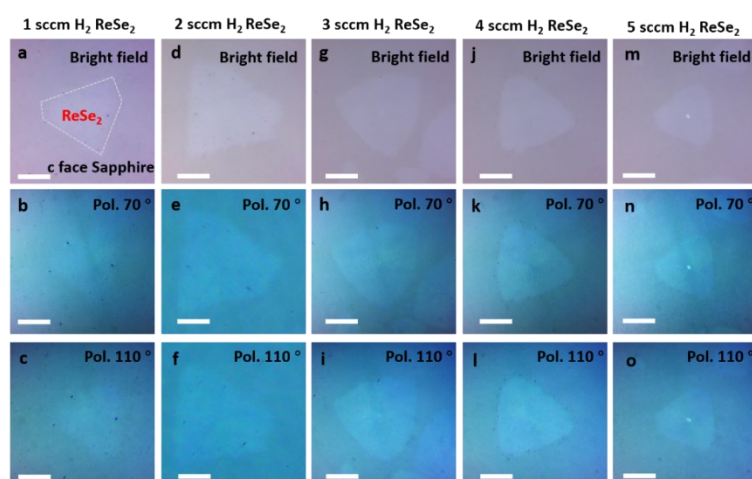
2D  $\text{ReSe}_2$  flakes (Figure 43a & Figure 44) in our experiments are grown on c-face sapphire by split-two-zone CVD (Figure 43b), using ammonium perrhenate ( $\text{NH}_4\text{ReO}_4$ ) and selenium (Se) as the source materials, and a synthesis temperature of 700 °C, refer the Experimental Section for details. As observed in the optical micrographs (Figure 43c,d & Figure 45) and TEM images (Figure 43e), typical 2D  $\text{ReSe}_2$  continuous flakes are synthesized, with thicknesses varying between 1–2 atomic layers (1L-2L). The obtained 2D  $\text{ReSe}_2$  is largely polycrystalline, formed by nanometer-sized grains. In Figure 43e, the crystal orientations (diamond Re chain,  $\vec{a}$  direction) for each grain are highlighted by white arrows. Some nanometer-sized nuclei for 2D  $\text{ReSe}_2$ , as well as aggregates consisting of atomic-scale clusters ( $< 1$  nm) are dispersed on the edges and the surfaces of 2D  $\text{ReSe}_2$  (e.g., follow the red arrows in Figure 43e).



**Figure 43. CVD Synthesis of 2D ReSe<sub>2</sub>.** **a**, Atomic models for 2D ReSe<sub>2</sub>, **a** and **b** crystal directions are highlighted, **a** is along Re diamond chain direction. Re atom (blue), Se atom (yellow). **b**, Scheme of split-zone CVD growth. **c,d**, Optical images (non-polarized and polarized) for as grown monolayer 2D ReSe<sub>2</sub> flake, showing anisotropic stripe patterns. Scale bars = 10 μm. **e**, TEM HAADF image for as grown 2D ReSe<sub>2</sub>. Different grains are false colored for contrast enhancement. Red arrows mark the cluster aggregates. White arrows mark the  $\vec{a}$  direction for each grain. Scale bar = 10 nm.



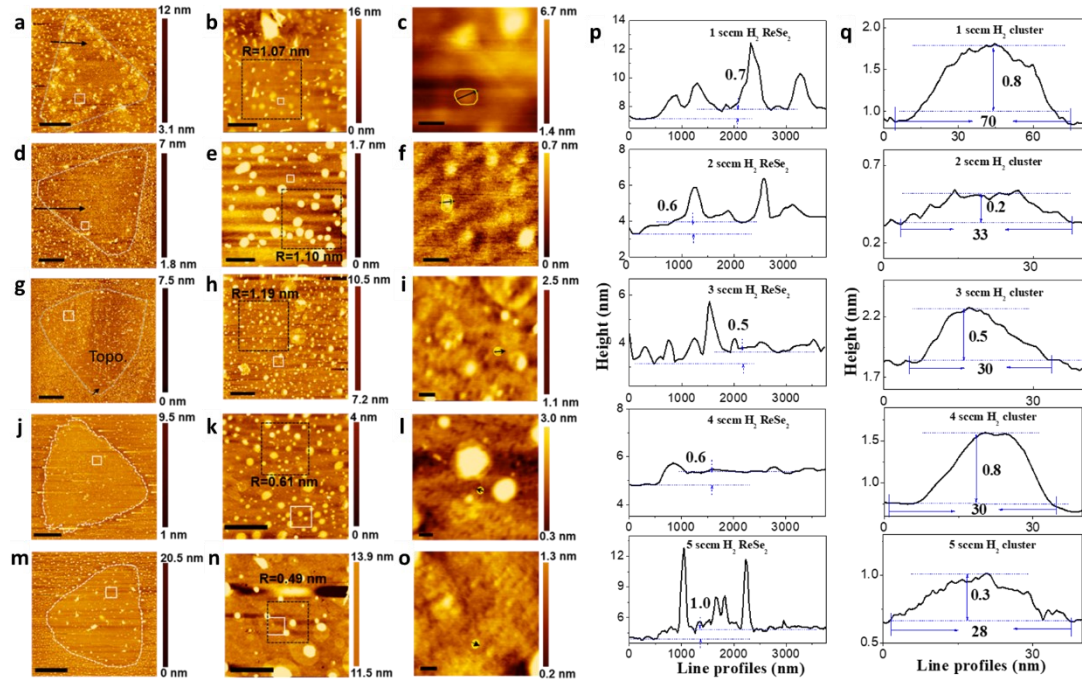
**Figure 44.** Crystal structures of **(a)** single layer ReSe<sub>2</sub> (top and side views) and **(b)** Re<sub>6</sub>Se<sub>8</sub> clusters. Re<sub>4</sub> rhenium chain is illustrated in red dashed lines<sup>208,209</sup>.



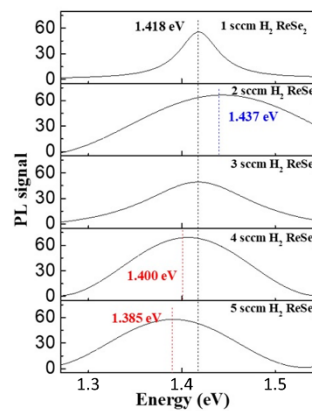
**Figure 45.** (a-c), (d-f), (g-i), (j-l) and (m-o) show bright field, 70° and 110° polarized light optical microscopic images of ReSe<sub>2</sub> grown with 1, 2, 3, 4 and 5 sccm H<sub>2</sub>. ReSe<sub>2</sub> subdomains have the sharpest contrast difference when the polarization angle of light is 70° and 110°. As the H<sub>2</sub> flow rate increased, the shapes kept as triangular with zigzag edges. Scale bars = 10 μm.

Different from mechanically induced grain boundaries in 2D ReSe<sub>2</sub><sup>210</sup>, the polycrystalline 2D layer here with incommensurate grain boundaries is apparently formed by merging of randomly nucleated crystallites. The nucleus densities of the first and second layers are comparable (*ca.* 10<sup>3</sup> μm<sup>-2</sup>). It is also noted that the free edges of the ReSe<sub>2</sub> flakes prevalently follow the diamond chain  $\vec{a}$  direction, irrespective of the first or second atomic layers. The anisotropic nature of 2D ReSe<sub>2</sub> gives rise to the particular stripe-like morphologies of ReSe<sub>2</sub> crystals, following the principle  $\vec{a}$  direction. More atomic force microscopy (AFM) and photoluminescence spectroscopy (PL) results of these 2D ReSe<sub>2</sub> flakes are presented in Figure 46-Figure 47. In general, the morphologies/thicknesses in our 2D ReSe<sub>2</sub> can be controlled by a few variables (temperature, growth duration, flow rates) in CVD process. In particular, the yielded surface roughness of 1L ReSe<sub>2</sub> can be significantly reduced by increasing H<sub>2</sub> gas flow during CVD synthesis (Figure 46). The enhanced uniformity in samples with increased H<sub>2</sub> also leads to higher strain levels retained in final 2D ReSe<sub>2</sub> samples (un-delamination

of flakes), evidenced by the PL peak shift (Figure 47) and drops of polarized Raman intensities (Figure 48).



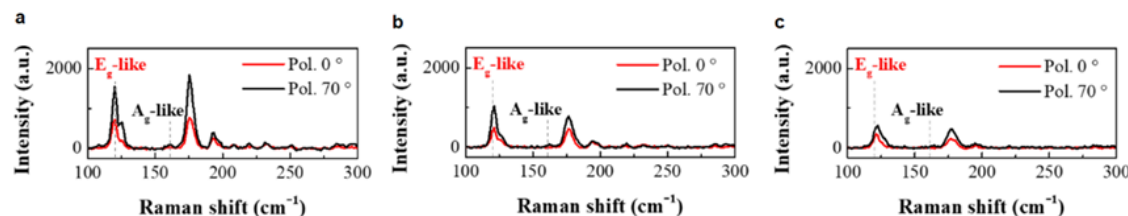
**Figure 46.** Atomic force microscopy images and profiles of 1L-ReSe<sub>2</sub> grown with 1-5 sccm H<sub>2</sub>. (a-c), (d-f), (g-i), (j-l), (m-o) show topographic images of 1-5 sccm H<sub>2</sub> grown ReSe<sub>2</sub>, tiny clusters sized 60 nm in diameter can be observed in all the samples. The surface roughness (R) decreased significantly from 1-3 sccm H<sub>2</sub> conditions (R~1 nm) to 4 sccm, (R~0.6 nm) and 5 sccm (R~0.5 nm) H<sub>2</sub> growth conditions. Scale bars = 10 μm (a,b,d,e,g,h,j,k,m,n), 50 nm (c,f,i,l,o). p, Height profiles of 1-5 sccm H<sub>2</sub> ReSe<sub>2</sub> single layers, corresponding to images (a,d,g,j,m). q, Height profiles of Re<sub>6</sub>Se<sub>8</sub> clusters on 1-5 sccm H<sub>2</sub> ReSe<sub>2</sub>, corresponding to images (c,f,i,l,o). The height of ReSe<sub>2</sub> flakes stayed the same and that of clusters remained similar as the H<sub>2</sub> flow rate changed from 1 sccm to 5 sccm.



**Figure 47.** PL spectroscopy of 1L-ReSe<sub>2</sub> grown with 1-5 sccm H<sub>2</sub> and transferred on suspended positions on TEM grid. The PL of 2 sccm H<sub>2</sub> ReSe<sub>2</sub> showed a 0.01 eV blueshifts compared with 1 sccm and 3 sccm H<sub>2</sub> ReSe<sub>2</sub>. The PL of 4 sccm and 5 sccm H<sub>2</sub>



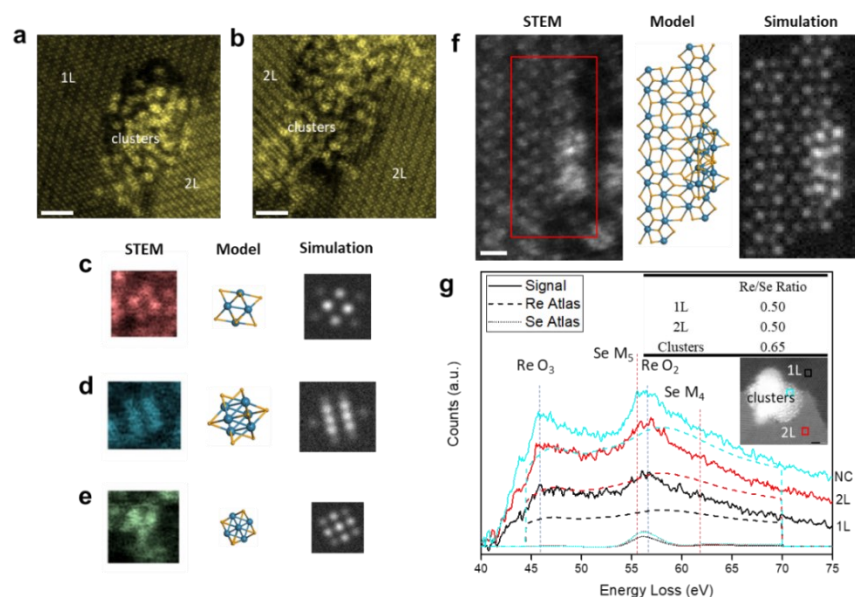
ReSe<sub>2</sub> showed a 0.01 eV and 0.02 eV redshifts compared with 1 sccm and 3 sccm H<sub>2</sub> ReSe<sub>2</sub>, which may also result from higher strains in the sample caused by more uniform morphology of flakes<sup>211</sup>.



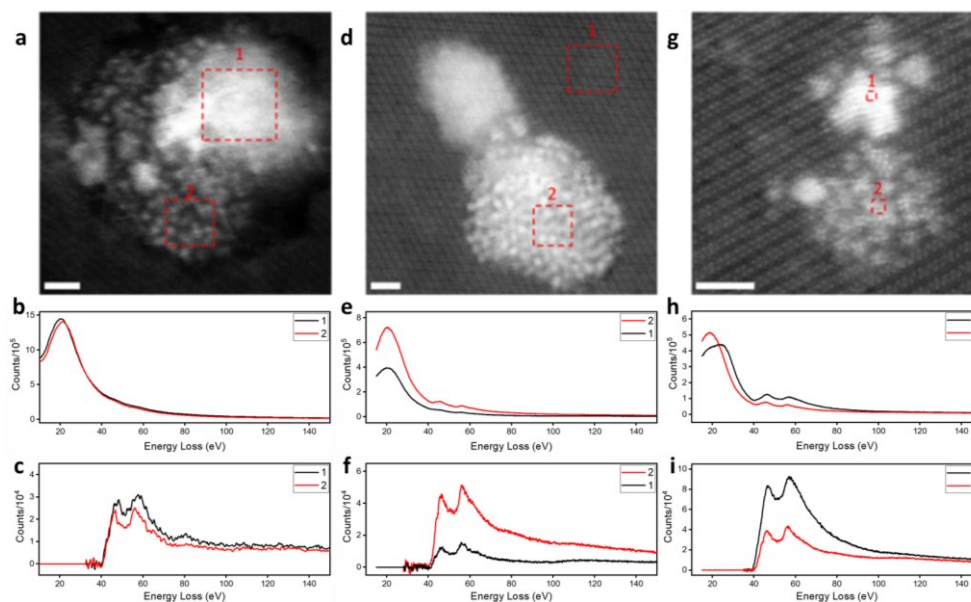
**Figure 48. Polarization angle-resolved Raman spectroscopy of ReSe<sub>2</sub> grown with 1, 2 and 3 sccm H<sub>2</sub>.** a-c, show polarized 0° and 70° Raman spectroscopy, descending in Raman intensity of most peaks between 100-300 cm<sup>-1</sup>. Raman single spectrum of 1, 2 and 3 sccm H<sub>2</sub> ReSe<sub>2</sub> show that the Raman intensity of 121 cm<sup>-1</sup> E<sub>g</sub>-like mode decreased at 2 sccm and 3 sccm H<sub>2</sub> ReSe<sub>2</sub>, which can be explained by the hindering of in-plane E<sub>g</sub>-like vibration caused by remaining strain at the flake-substrate interfaces, caused by better uniformity and reduced cluster aggregates by higher H<sub>2</sub> flow.

### 3.3.2. Identification of Re<sub>x</sub>Se<sub>y</sub> molecular clusters

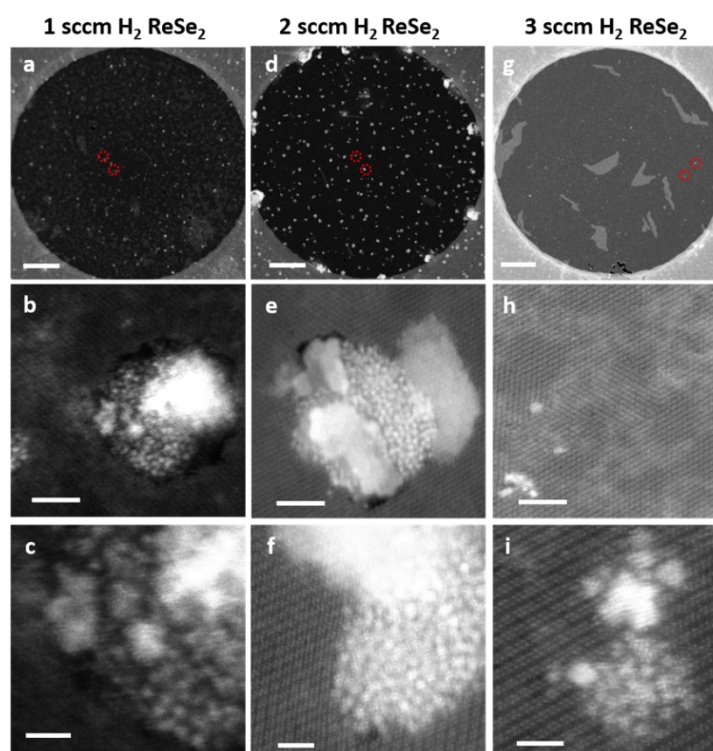
According to the initial precursors in our experiment, vaporized Re<sub>2</sub>O<sub>7</sub> and Se<sub>n</sub> (n = 3-8) molecules take the main portion in the atmosphere of CVD chamber (see 3.2.1). However, except for the monoclinic 2D ReSe<sub>2</sub> film as expected in our growth product, the high-resolution scanning TEM (STEM) (mainly through high angle annular dark field (HAADF) imaging) (Figure 49a-f) also reveals large quantity of Re<sub>x</sub>Se<sub>y</sub> clusters attached to the surfaces/edges of as-grown 2D ReSe<sub>2</sub> flakes. The atomic structures and chemical compositions of such clusters are verified with multislice STEM image simulations (Figure 49e-f) and atomic-scale electron energy loss spectroscopy (EELS) results (Figure 49g and Figure 50). In most of the cases, these Re<sub>x</sub>Se<sub>y</sub> clusters are attached to the edges of monolayer or bilayer ReSe<sub>2</sub>, while the atomic clusters residing away from edges can be attributed to the defective anchoring sites on van der Waals (vdW) surfaces of 2D ReSe<sub>2</sub> (Figure 51 & Figure 52).



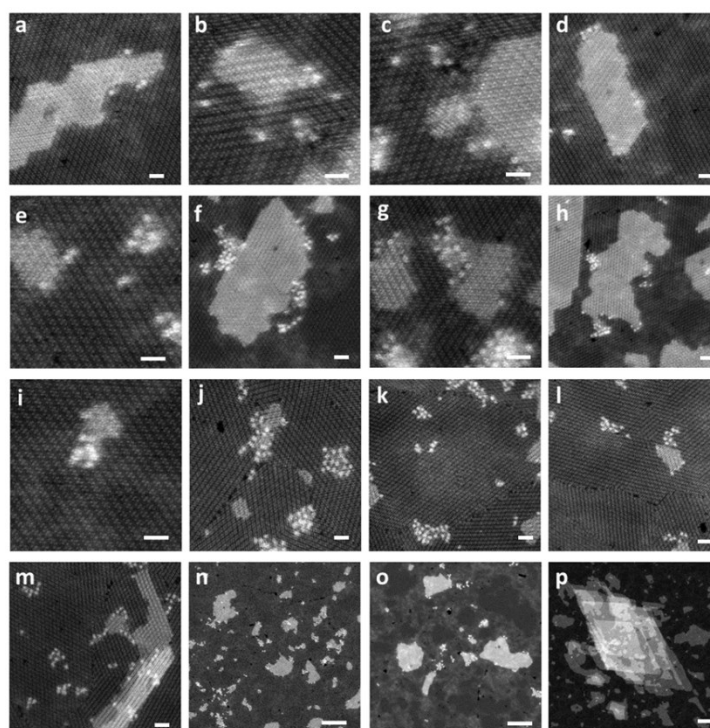
**Figure 49. STEM characterizations of  $\text{Re}_6\text{Se}_8$  clusters.** **a,b**,  $\text{Re}_6\text{Se}_8$  cluster aggregates residing in holes of mono- and bi-layer  $\text{ReSe}_2$ . Scale bars = 2 nm. **c-e**, STEM-HAADF images, DFT derived atomic models and STEM image simulations of  $\text{Re}_6\text{Se}_8$  clusters in different orientations. **f**, STEM image, DFT derived atomic model and STEM image simulations for two  $\text{Re}_6\text{Se}_8$  clusters attached to the edge of 2D  $\text{ReSe}_2$ . Scale bar = 0.5 nm. **g** EELS results (background subtracted) for  $\text{Re}_6\text{Se}_8$  cluster aggregates, EELS quantification consistently gives higher Re/Se ratio in clusters than in 2D  $\text{ReSe}_2$  layers.



**Figure 50. Electron energy loss spectroscopy (EELS) spectra of  $\text{Re}_6\text{Se}_8$  clusters.** **(a-i)** show HRTEM image and EELS spectra of 1L  $\text{ReSe}_2$  and  $\text{Re}_6\text{Se}_8$  clusters on 1, 2, and 3 sccm  $\text{H}_2$  grown  $\text{ReSe}_2$ . **(a-c)** 1 sccm  $\text{H}_2$ , **(d-f)** 2 sccm  $\text{H}_2$ , **(g-i)** 3 sccm  $\text{H}_2$  conditions. **(b,e,h)** show the original EELS spectra and **(c,f,i)** show the signals after background subtraction. The peaks of 46 eV and 57 eV in **(b, c, e, f, h, i)** correspond to  $\text{Re O}_3$  and  $\text{Re O}_2$  with  $\text{Se M}_{4,5}$  peaks, respectively. Scale bar = 2 nm. Red dash boxes indicate the corresponding scanning areas of EELS acquisition.



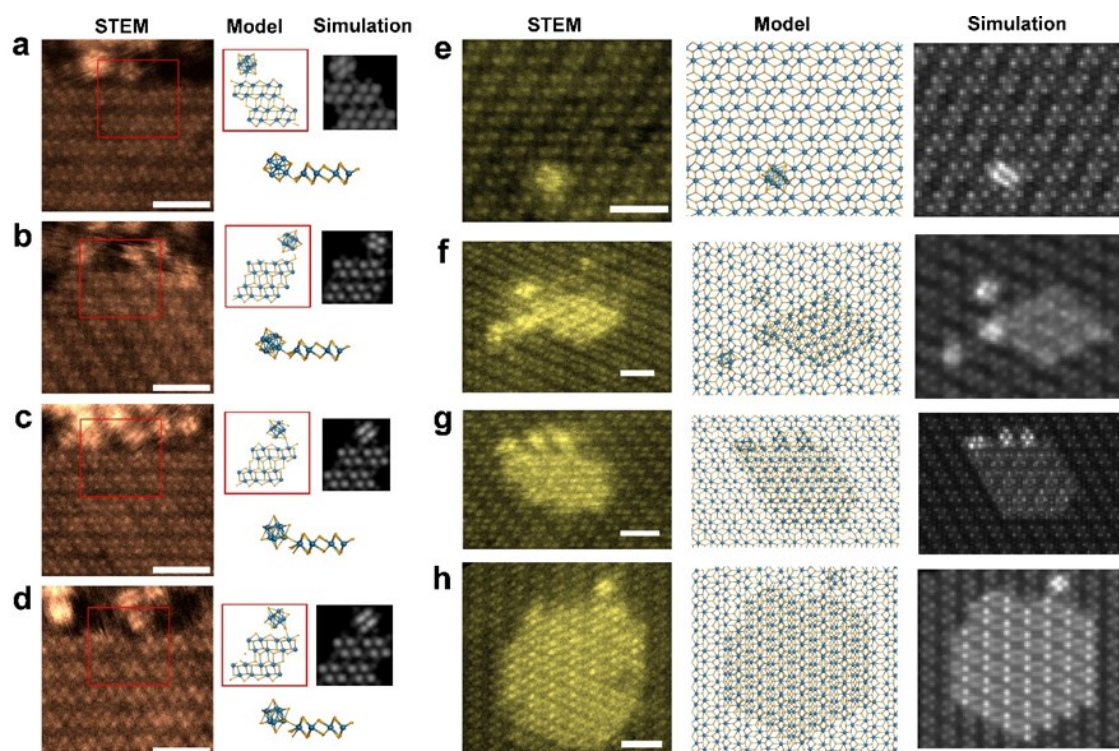
**Figure 51. STEM images of 2D ReSe<sub>2</sub> product grown with 1, 2 and 3 sccm H<sub>2</sub> condition.** Tiny clusters are shown in all (a-c) 1 sccm H<sub>2</sub> ReSe<sub>2</sub>, (d-f) 2 sccm H<sub>2</sub> ReSe<sub>2</sub>, (g-i) 3 sccm H<sub>2</sub>. The 3 sccm H<sub>2</sub> sample contains significantly less cluster aggregates than 1 and 2 sccm growth conditions. Scale bar = (a,d,g) 200 nm, (b,e,h) 5 nm, (c,f,i) 2 nm.



**Figure 52. STEM images for Re<sub>6</sub>Se<sub>8</sub> clusters on surfaces and edges of as-grown 2D ReSe<sub>2</sub> flakes.** Each dotted like bright spot corresponds to a single Re<sub>6</sub>Se<sub>8</sub> molecular cluster. Scale bars in (a-m) = 1 nm, scale bars in (n-p) = 10 nm.



### 3.3.3. Key reactions and intermediate steps involved in growth

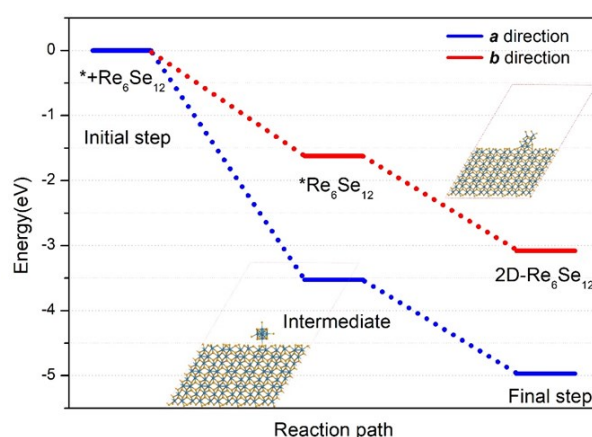


**Figure 53.  $\text{Re}_6\text{Se}_8$  clusters and nucleation.** a-d, STEM image, DFT derived atomic model and STEM image simulation for  $\text{Re}_6\text{Se}_8$  clusters anchored on different edges of 2D  $\text{ReSe}_2$  through Se linkage atoms. e-h, STEM image, atomic model and STEM image simulation for  $\text{Re}_6\text{Se}_8$  clusters anchored on monolayer  $\text{ReSe}_2$  surfaces and crystal nuclei for epilayers of 2D  $\text{ReSe}_2$  with  $\text{Re}_6\text{Se}_8$  clusters attached on edges. Scale bars = 1 nm.

Rhenium oxide clusters can be safely excluded in our STEM images because they are highly water soluble<sup>212</sup> and cannot survive the wet transfer processes from growth substrates to TEM grids (see 3.2.1). Our experiments, STEM image simulations and DFT atomistic simulations have captured the typical interfacial structures between  $\text{Re}_6\text{Se}_8$  clusters and 2D  $\text{ReSe}_2$  (Figure 49f & Figure 53). Most of the survived clusters on edge or surfaces are covalently bonded through the linkage Se atoms. In agreement with the reported structures of the rhenium octahedron ( $\text{Re}_6$ ) in  $\text{Re}_6\text{Se}_8$  cluster complexes<sup>213,214</sup>, the majority of clusters attached to the 2D specimens contain six Re atoms have been confirmed experimentally. The projected STEM images for  $\text{Re}_6\text{Se}_8$  clusters in different tilt angles with respect to the viewing direction ( $e^-$  beam direction) are presented in Figure



49c-e. Due to the weaker contrast of Se atoms, the exact number of Se atoms in each cluster cannot be resolved by direct STEM imaging. Nevertheless, our DFT simulations have suggested that these octahedron clusters play crucial roles in reaction paths and have revealed further selenization processes of clusters toward 2D  $\text{ReSe}_2$  (Figure 54). In addition, considering the prevalence of  $\text{Se}_8$  molecules in CVD chamber, the  $\text{Re}_6\text{Se}_8$  clusters are more likely to form compared to other clusters such as  $\text{Re}_2\text{Se}_4$  or  $\text{Re}_4\text{Se}_6$ .



**Figure 54. Reaction energy profile for selenization process along edges of *a* (blue) and *b* (red) by DFT calculations.** Initial and final steps involve gas phase  $\text{Re}_6\text{Se}_{12}$  cluster adsorbed on different edges to 2D cluster formation.

These *ex situ* observations do not preclude other possible reactants or intermediate species in high temperature CVD chambers. The weakly bonded clusters or atoms might have been removed/escaped from  $\text{ReSe}_2$  surfaces before observing them by STEM. However, with the high frequency of presence as observed in these post-CVD synthesis samples, it is reasonable to conclude that  $\text{Re}_6\text{Se}_8$  clusters have high stability among all the reactants. Importantly, once the reactive sites (edges, defects on surfaces) are occupied by  $\text{Re}_6\text{Se}_8$  clusters, further growth (selenization of  $\text{Re}_6\text{Se}_8$ ) requests to overcome relative high energy barriers. In other words, CVD growth is significantly retarded by this intermediate stage, and the growth rate is mainly controlled by the conversion from  $\text{Re}_6\text{Se}_8$  clusters to 2D  $\text{ReSe}_2$ . Hexarhenium cluster cores with the general formula



$[\text{Re}_6\text{Q}_8]^{2+}$  ( $\text{Q} = \text{S}, \text{Se}$ ) have very high stability, which can serve as the building blocks of many kinds of novel compounds<sup>200</sup>. Thus, such kinds of clusters as the main reactant can be directly observed during experiment. However, by far, the whole evolution process from the 3D face-capped octahedral core of  $\text{Re}_6\text{Q}_8$  to 2D  $\text{ReSe}_2$  formation is difficult to be determined via computational simulations. The  $\text{Re}/\text{Se}$  ratios in  $\text{Re}_6\text{Q}_8$  and 2D  $\text{ReSe}_2$  are 0.75 and 0.5, so additional four Se atoms ( $\text{Re}_6\text{Se}_{12}$ ) should be added in the 2D  $\text{ReSe}_2$  reactions. Here, a simple DFT model has been employed to evaluate the chemical reaction under thermodynamic consideration using  $\text{Re}_6\text{Se}_{12}$  as reactants. The adsorption energies of key intermediates are studied and depicted in Figure 54.

The DFT simulations have given the key reaction paths and revealed that the further selenization process of these clusters should proceed with high edge selectivity along edges along  $\vec{a}$  direction. The corresponding absorption energies of  $\text{Re}_6\text{Se}_{12}$  (4 Se atoms are subsequently added onto  $\text{Re}_6\text{Se}_8$  cluster) and the whole reaction energies are much lower than the case along  $\vec{b}$  edges by energy gaps of -1.90 and -1.89 eV under thermodynamic consideration (Figure 54). The result is in agreement with the preferred edges for 2D clusters formation in our STEM observations (Figure 53a-d). This also well explains why the 2D  $\text{ReSe}_2$  tends to grow along the diamond Re chain ( $\vec{a}$ ) direction and form elongated rectangles in morphology. Besides, each diamond cell in 2D  $\text{ReSe}_2$  contains four rhenium atoms, mismatched with the six atoms in each cluster. Hence the completion of selenization (from  $\text{Re}_6\text{Se}_8$  cluster to 2D  $\text{ReSe}_2$  layer) should sometimes leave bi-Re atom structures on edges (Figure 53g captures intermediate structures). These locations will be easier to trap another  $\text{Re}_6\text{Se}_8$  cluster, as observed in Figure 53g. For the same reason,  $\text{Re}_6\text{Se}_8$  clusters prefer to aggregate in odd numbers on growth edges, even number  $\text{Re}_6\text{Se}_8$  clusters are much easier to form 2D  $\text{ReSe}_2$ .

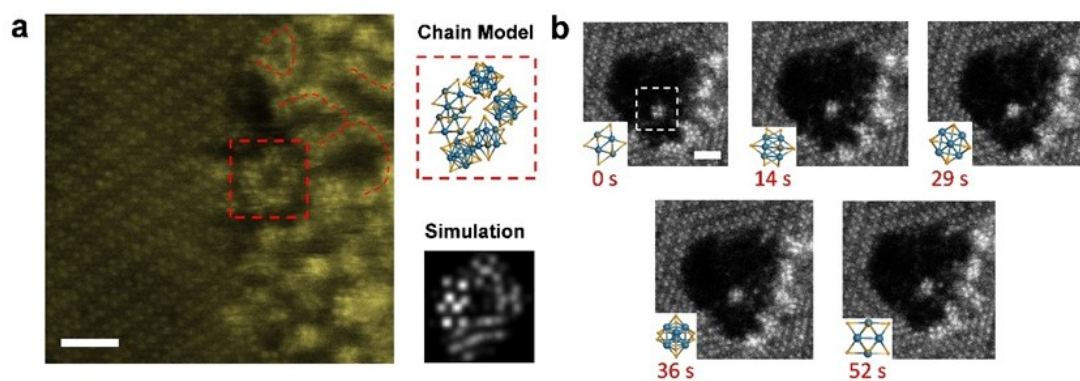


$\text{Re}_6\text{Se}_8$  clusters favor the further aggregation as cluster agglomerates sized from 1 nm to few nanometers (Figure 49a,b, Figure 52 and Figure 55a). The clusters form one-dimensional chain-like structures (Figure 55a). These cluster complexes are highly stable and embedded in the 1L or 2L  $\text{ReSe}_2$ . Experimentally, the density of such cluster complexes as well as survival individual clusters can be reduced by a higher concentration of hydrogen in CVD atmosphere (Figure 51), implying hydrogen is the key for reducing cluster aggregation and triggering conversion from clusters into a 2D structure. The cluster agglomerates embedded in the 2D layers can introduce large defects (holes) in 2D films after removal/evaporation of clusters, therefore maintaining a reductive hydrogen environment in CVD growth is indispensable for 2D full film growth.

$\text{Re}_6\text{Se}_8$  cluster is highly stable, Figure 55b shows a single cluster can withstand high energy  $e^-$  beam irradiation, while only cluster rotation is found. During CVD growth, these clusters can be freely transported in CVD atmosphere or on the solid (substrate/product) surfaces. Our STEM results directly unraveled the nucleation process. The observed smallest nuclei for 2D  $\text{ReSe}_2$  (on  $\text{ReSe}_2$  substrate) are smaller than 1 nm (Figure 53b), (*ca.* two by two unit cells of monoclinic  $\text{ReSe}_2$ ). Regarding the nucleation probability, as the observation in 2D specimens, a lot of nuclei are stable even in single  $\text{Re}_6\text{Se}_8$  cluster form or bi-cluster form (Figure 43e). With the undergoing reactions, these covalently surface-trapped clusters on surfaces of 2D  $\text{ReSe}_2$  can easily develop into larger islands of  $\text{ReSe}_2$  epilayers (Figure 53e-h). In contrast, the kinetics of individual metal or chalcogenide atoms (in some previous growth models<sup>178</sup>) are much faster. Therefore, the nucleation rate of 2D  $\text{ReSe}_2$  is greatly enhanced by such  $\text{Re}_6\text{Se}_8$  clusters, and the kinetical (non-thermal) growth is also greatly strengthened due to the existence of such molecular clusters. To suppress unwanted nucleation and epi-layer growth, and to achieve the ideal

Frank-van der Merwe (FM) layer-by-layer growth, high quality layers with minimum atomic defects and vacancies (anchoring sites for clusters) is favored.

Our observations do not rule out other growth mechanisms, such as direct individual atomic growth or selenization from oxides. Nonetheless, evidenced by our direct STEM observations,  $\text{Re}_6\text{Se}_8$  clusters can easily and stably bond to edges as well as surfaces of 2D  $\text{ReSe}_2$ , giving rise to higher reaction possibilities and yielding the 2D structures. The preferential adsorption of  $\text{Re}_6\text{Se}_8$  clusters on different edges and the retarded transport of  $\text{Re}_6\text{Se}_8$  clusters along edges/on surfaces significantly alter the growth kinetics and the final product morphologies. Some unexpected effects might even occur, for instance, due to the preferred bonding of  $\text{Re}_6\text{Se}_8$  clusters with atomic vacancies and the enhanced Se vacancies at higher temperatures, the nucleation rate for epi-layers actually increases with temperature, violating normal principles for 2D material growth whereas higher temperature yields higher uniformity<sup>215</sup>.



**Figure 55. Stable  $\text{Re}_6\text{Se}_8$  clusters and aggregates.** **a**, STEM image, atomic model and image simulation for cluster aggregates. Chain-like structures are highlighted by red dashed lines and boxes in STEM images. **b**, Stability of single  $\text{Re}_6\text{Se}_8$  cluster under e beam irradiation for 52 s. Rotation of cluster (center in white dashed box) is noted, corresponding atomic models for  $\text{Re}_6\text{Se}_8$  cluster of each time are embedded in lower left corners. Scale bar = 1 nm.



### 3.4. Summary

Our atomic-scale observations combined with theoretical simulations on the intermediate stages of the 2D ReSe<sub>2</sub> growth directly reveal the reaction paths in CVD process, with implications for general 2D TMDCs materials growth. Based on our observations, here, a simple model for APCVD of 2D TMDCs is proposed. It consists of two-step reactions: (1) Reduction reactions with chalcogenides and hydrogen in atmosphere to form  $M_xX_{2x-n}$  clusters ( $M$  = transition metals,  $X$  = chalcogens). (2) Attachment of  $M_xX_{2x-n}$  clusters to the growth fronts and conversion into 2D TMDCs layers with the aid of hydrogen. The unveiled reaction paths are of great significance to understand the nucleation and growth kinetics of 2D TMDCs materials and will benefit the growth control on thickness and morphology for such emergent group of materials.





## Chapter 4. Unexpected Plasticity in VdW Materials

VdW materials always give us the impression that which is extremely brittle. However, a remarkable plasticity of  $\beta$  phase InSe has been reported in 2020<sup>92</sup>. The mechanism of the huge difference of other van der Waals materials contains many mysteries. Why do the cracks prefer propagating along basal plane rather than z axis? What slows down structural fracture? After applying discrete and gentle mechanical force, we not only find there are abundant micro-cracks, but also notice phase transition without heating. Besides, the phase transition initiated by mechanical force plays an important role in the plasticity, that reduces the cracks propagations. The gliding energy barrier along  $\langle 1\bar{2}10 \rangle$  direction is significantly increased 24.07% from 2H-InSe to 3R-InSe that is much higher than other vdW materials. The significant change acts as a pinning point to stop the microcrack propagation. Dislocations, interlayer and intralayer reconnection are also observed in atomic scale surrounded by 3R-InSe that also contribute to the plasticity. These findings provide insights into semiconductor engineering, flexible electronics, and solid-state lubricant.

### 4.1. Introduction

Writing with a pencil is the process that the graphite on the pencil tip is mechanically deformed by compression and lateral friction, transferred from the tip to the paper and forms a thin film on paper. In the microscopic view, there are numerous fracture events on the tip during such writing. For the “3H” or “2H” grading pencils<sup>216,217</sup>, lack of plastic deformation on the tip renders discontinued patterns and lighter color of the writings. By contrast, the softer “3B” or “2B” grading pencils can create a much more smooth and continuous writing due to their improved plasticity. The hardness and



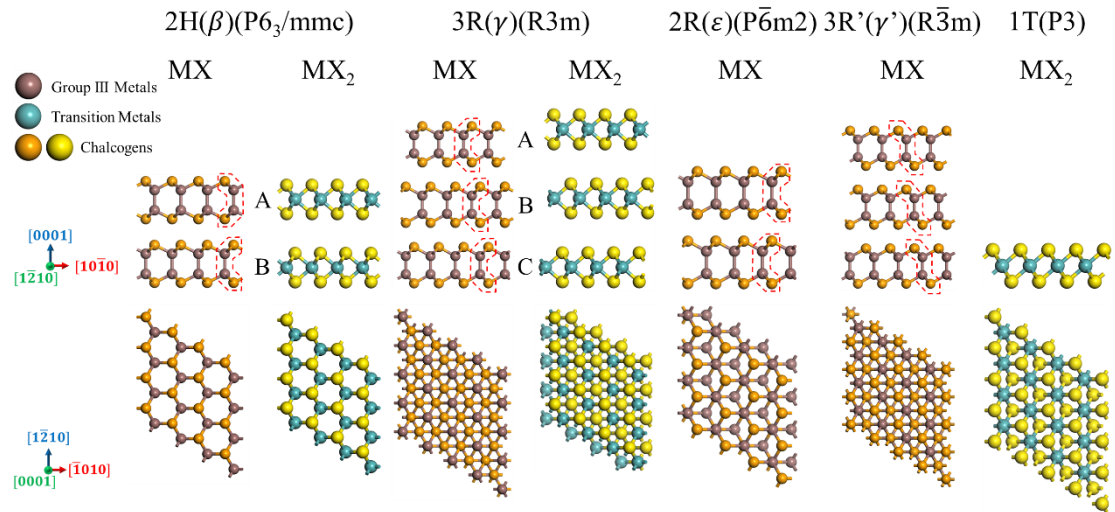


plasticity of the pencil tips are essentially determined by the structure and compositions of materials<sup>216,217</sup>.

In analogous to graphite, a rich family of van der Waals (vdW)-layered materials have been known for their strong intralayer bonding and weak interlayer interaction, which facilitate the easy interlayer gliding or exfoliation into the atomically-thin two-dimensional (2D) films<sup>78,92,218-220</sup>. The properties of ultra-thin metal chalcogenides (MX: M = Ga, In; X = S, Se, Te)<sup>221-225</sup> and transition metal dichalcogenides (MX<sub>2</sub>: M = Mo, W, Nb, Ta; X = S, Se, Te)<sup>44,226-233</sup> have been widely reported, including high carrier mobility<sup>224,225,232,233</sup>, high on/off ratio<sup>224-227</sup>, low subthreshold swing<sup>226,230</sup>, high deformability<sup>92,225,226,229,234-236</sup>, and ferroelectricity<sup>237,238</sup> etc. The excellent performances of flexible vdW-layered devices are even maintained at 2% strain<sup>225</sup>. They can also be engineered for wearable and bio-compatible devices<sup>234,236</sup>. The facile interlayer gliding also ensures the ultra-low friction between layers, enabling the vdW-layered materials to serve as solid-state lubricants (SSL) in industrial and engineering fields<sup>239,240</sup>. Very recently, an extraordinarily large plasticity (>80% for compression along in-plane and out-of-plane direction; >4000% for compression ratio by gradually rolling) was unveiled in a vdW-layered material —  $\beta$ -InSe<sup>92</sup>. Benefiting from the ultra-high deformation capabilities and the significantly lowered fracture and fragmentation tendency, such ultra-plastic, semiconducting, vdW-layered materials could open promising avenues for the future flexible electronics<sup>225,234,241</sup> and SSL industry<sup>239,240,242</sup>.

Apparently, the ultra-plasticity of 2H-InSe is associated with the interlayer gliding and the cross-layer dislocation slip<sup>92</sup>. However, the full picture of the plastic deformation, especially why the 2H-InSe possesses a much higher plasticity than other vdW-layered materials such as graphite<sup>243,244</sup> and transition metal dichalcogenides (TMDCs)<sup>92</sup> has not

been elucidated yet. Here, we perform comprehensive structural analysis in atomic scale, particularly the *in situ* transmission electron microscopy (TEM), combined with theoretical atomistic simulations to investigate the defect evolutions during the plastic deformation of various vdW-layered materials. We find that there are high density micro-cracks and phase transition after applying discrete and gentle mechanical driving force, that are effective in relieving the stress and responsible for the ultrahigh plasticity in  $\beta$ -InSe. No one considered the contributions of phase transition in the plasticity of the  $\beta$ -InSe in previous experimental and theoretical studies<sup>92,94</sup>. This is simply because there is no report about phase transition without thermal energy in vdW materials. Besides, the interlayer gliding results in stacking faults or dislocations<sup>92</sup>, however, owing to the different symmetry, interlayer gliding should not easily switch between 2H and 3R stacking without thermal energy.



**Figure 56. Structure of metal chalcogenides and transition metal dichalcogenides along  $[1\bar{2}10]$  and  $[0001]$  in  $P6_3/mmc$ ,  $R3m$ ,  $P\bar{6}m2$ ,  $R\bar{3}m$ , and  $P3$  symmetry. The red dashed polygons show the directions of each layer in MX.**

Figure 56 shows polymorph of MX and MX<sub>2</sub> that will be discussed in this chapter.

$\beta$ -InSe belongs to the space group  $P6_3/mmc$ , also is called 2H phase, whereas the two layers AB stacked in one unit cell are alternatively rotated by  $180^\circ$  (equivalent to  $60^\circ$ )<sup>245</sup>.



The counterpart, meaning the atomic layers are stacked without rotation,  $\gamma$ -,  $\varepsilon$ -, and  $\gamma'$ -InSe with ABC, AB, ABC stacking belongs to the space group  $R3m$ ,  $P\bar{6}m2$ ,  $R\bar{3}m$ , respectively. Similarly, there are 2H, 3R, 1T phases for  $MX_2$ . To be more comparable, 2H, 3R, 2R, 3R', and 1T are used to compare the properties of InSe,  $MoS_2$  and  $MoTe_2$ .

More importantly, the overlooked phase transition plays an important role in the plasticity. The microscale intralayer cracks do not extend in  $\vec{z}$  direction (vertical to the basal plane) or coalesce to form macroscopic fracture surfaces in 2H-InSe. It is primarily because the stacking order changes (2H to 3R) at the interlayer micro-cracks due to the phase transition, and the 3R stacking of InSe has markedly higher gliding barrier than the pristine 2H stacking order confirmed by using molecular dynamic (MD) simulations here. Hence, the 3R stacking locations originated from the micro-cracks could play as pinning points which prevent microcrack propagation to form complete fracture along  $\vec{z}$  direction. Subsequently, large quantity of micro-cracks in different layers and different locations allow for the reorganization of layers under compression or tensile stress, resulting in the ultra-plastic behavior. We also examined several other typical vdW-layered materials and close gliding energy barriers are found in 2H and 3R phases of all the other materials, implying the exceptional plasticity in 2H-InSe, much higher than the other layered materials, probably arise from the micro-cracks and “3R pinning”.

## 4.2. Methodology

In this session, the bulk crystals were purchased to minimize the workflow. A small hammer was used to provide gentle and discrete force onto the tested samples. The TEM specimens were prepared by mechanical exfoliations and focused ion beam (FIB) for different purposes. The predictions have been done by DFT, and MD. The details will be clearly stated below.



### 4.2.1. Specimen preparations and experimental design

2H-InSe single crystal (size:  $5 \times 5 \text{ mm}^2$ ) was purchased from Nanjing Mukenano. 2H-MoS<sub>2</sub> (size: 10 mm) and 2H-MoTe<sub>2</sub> (size: 10 mm) were purchased from HQ Graphene. Compression force and uniaxial shear stress were gently applied by a hammer for approximately 100-200 times with strain rate  $\sim 0.5/\text{s}$  until no more deformation, in order to create high density dislocations and cracks. The size of the crystals was measured by a pair of digital calipers ( $\pm 0.01 \text{ mm}$ ) and the force was measured by YISIDA digital force gauge ( $\pm 0.01 \text{ N}$ ). The hammered crystals were mechanically exfoliated by scotch tape and transferred by thermal release tape<sup>173</sup>. Control group was mechanically exfoliated without applying compress force and shear stress. The cross-section specimens were prepared by Helios 5 CX DualBeam focused ion beam (FIB).

### 4.2.2. Preliminary characterizations

Raman spectra were collected by the WITec Alpha300R confocal microscopy using a 532 nm laser with a grating of 1800 g/mm. XRD spectra were conducted by the Rigaku SmartLab X-ray diffractometer with 9 kW rotating anode X-ray source (wavelength  $\approx 1.54 \text{ \AA}$ ).

### 4.2.3. (S)TEM characterizations

Atomic STEM images were acquired under a Cs-corrected STEM (Thermo Scientific<sup>TM</sup> Spectra 300 (S)TEM operated at 300 kV with a convergence semi-angle of 24.4 mrad. The collection angles of ADF detector were set as 35-200 mrad. The screen current was set as 10 pA by an unfiltered monochromator to reduce the irradiation damage. TEM and STEM images were acquired by Orius SC1000 charge-coupled device (CCD) and Digiscan II under a (S)TEM (JEOL JEM-2100F) operated at 200 kV.



#### 4.2.4. *In situ* TEM

Nanofactory<sup>TM</sup> holder has been implemented in JEM-2100F operated at 200 kV to conduct *in situ* experiments. Similar to our previous works<sup>246</sup>, a homemade tungsten (W) tip was electrochemically etched for manipulating the specimen and a homemade TEM grid holder was used for the further characterization without damaging the TEM grid. The bending experiment was initiated by moving the W tip towards the InSe crystal via piezo-driven fine control. The bending process was video recorded in real time by Olympus Veleta CCD.

#### 4.2.5. Thickness estimation in HAADF-STEM

The line profiles with integration width 40 were extracted from GMS 3. The signal differences were confirmed by both HAADF-STEM and *in situ* TEM data, that correlated to the specimen thickness for thin specimens. The fitting by adjacent-averaging method presented the extracted data points more understandable.

#### 4.2.6. HAADF-STEM simulations

Dr. Probe<sup>247</sup> was used for simulating STEM-HAADF images. Accelerating voltage, convergence semi-angle, and collection angle were set same as the imaging, which were 300 kV, 24.4 mrad, and 35-200 mrad, respectively. Aberration correction values were set as following: A1: 1.84 nm (83.2°), A2: 13.5 nm (9.3°), B2: 30.7 nm (108.5°), C3: 252 nm, A3: 600 nm (-162°), S3: 216 nm (2.1°), A4: 3.31  $\mu$ m (170.3°).

#### 4.2.7. Molecular dynamics

Large-scale Atomic/Molecular Massively Parallel Simulator (LAMMPS) (version, 29 September 2021)<sup>248</sup> has been performed to calculate the gliding barrier along  $\langle 10\bar{1}0 \rangle$



and  $\langle 1\bar{2}10 \rangle$  for 2H and 3R stack with a bi-layer model. A developed Stillinger-Weber potential<sup>249</sup> was used to approximate the intralayer interactions in MX and MX<sub>2</sub> and 12-6 Lennard-Jones potentials<sup>250</sup> was used to approximate the non-bonded interlayer interactions. Lennard-Jones cutoffs were set 12.8 and 12.0 for MX and MX<sub>2</sub>, respectively. All force-field parameters used in this work were taken from Rappe's work<sup>251</sup>.

#### 4.2.8. DFT calculations

Density functional theory (DFT) calculations were performed to study structural, electronic and mechanical properties of the vdW MX and MX<sub>2</sub> structures, in which Vienna Ab initio Simulation Package (VASP.5.4.4.18)<sup>202,203</sup> was used with a projector augmented wave (PAW)<sup>204</sup> basis and Perdew-Burke-Ernzerhof (PBE) parameterized Generalized Gradient Approximation (GGA) exchange-correlation functional. For all the calculations, the kinetic energy cutoff for electronic plane wave expansion was set to 400 eV.  $\Gamma$ -centered  $12 \times 12 \times 2$  and  $1 \times 12 \times 2$   $k$ -points-grids were used to sample the first Brillouin zone of InSe and MoS<sub>2</sub> unit cell and supercell, respectively. Moreover, van der Waals interaction was included using DFT-D3 method with Becke-Jonson damping<sup>207,252</sup>. The energy barrier of phase transition was calculated by the climbing image nudged elastic band (CI-NEB)<sup>253</sup> method using  $10 \times 1 \times 1$  supercell. Total energy and the forces on each atom were converged to less than  $10^{-8}$  eV and 0.01 eV/Å, respectively. The elastic modulus of 2H and 3R phase of InSe and MoS<sub>2</sub> were calculated using a finite differences approach. The crystal orbital Hamilton populations (COHP) were calculated by LOBSTER package<sup>254</sup> to estimate the bond strength. The integration of partial COHP for bonding state (below fermi level) was conducted to estimate the strength of In-Se and Mo-S bonding due to their same bonding configuration.



### 4.2.9. Mechanical properties from the elastic constants

In generally, the stiffness tensor is denoted as following matrix,

$$C = \begin{bmatrix} C_{11} & C_{12} & C_{13} & C_{14} & C_{15} & C_{16} \\ C_{21} & C_{22} & C_{23} & C_{24} & C_{25} & C_{26} \\ C_{31} & C_{32} & C_{33} & C_{34} & C_{35} & C_{36} \\ C_{41} & C_{42} & C_{43} & C_{44} & C_{45} & C_{46} \\ C_{51} & C_{52} & C_{53} & C_{54} & C_{55} & C_{56} \\ C_{61} & C_{62} & C_{63} & C_{64} & C_{65} & C_{66} \end{bmatrix} \quad \text{eq. 32}$$

Considering the crystal symmetry of MoS<sub>2</sub> and InSe, we can simplify the matrix to be,

$$C = \begin{bmatrix} C_{11} & C_{12} & C_{13} & C_{14} & 0 & 0 \\ C_{12} & C_{11} & C_{13} & -C_{14} & 0 & 0 \\ C_{13} & C_{13} & C_{33} & 0 & 0 & 0 \\ C_{14} & -C_{14} & 0 & C_{44} & 0 & 0 \\ 0 & 0 & 0 & 0 & C_{44} & C_{14} \\ 0 & 0 & 0 & 0 & C_{14} & C_{66} \end{bmatrix} \quad \text{eq. 33}$$

Due to the anisotropic nature, Voigt-Reuss-Hill method is used to calculate the mechanical properties<sup>255</sup>. The bulk and shear moduli are denoted as,

$$B = 1/2(B_V + B_R) \quad \text{eq. 34}$$

$$G = 1/2(G_V + G_R) \quad \text{eq. 35}$$

where  $B_V$  and  $G_V$  are the Voigt bulk and shear moduli<sup>256</sup>, and  $B_R$  and  $G_R$  are the Reuss bulk and shear moduli<sup>257</sup>.

$$B_V = (2C_{11} + 2C_{12} + 4C_{13} + C_{33})/9 \quad \text{eq. 36}$$

$$G_V = (2C_{11} - C_{12} - 2C_{13} + C_{33} + 6C_{44} + 3C_{66})/15 \quad \text{eq. 37}$$

$$B_R = (2S_{11} + 2S_{12} + 4S_{13} + S_{33})^{-1} \quad \text{eq. 38}$$

$$G_R = 15(8S_{11} - 4S_{12} - 8S_{13} - 4S_{33} + 6S_{44} + 3S_{66})^{-1} \quad \text{eq. 39}$$

where  $S_{ij}$  is the elastic compliances of  $C_{ij}$ . Then, the Young's modulus ( $E$ ) and Poisson ratio ( $\nu$ ) are obtained.





$$E = 9BG/(3B + G) \quad \text{eq. 40}$$

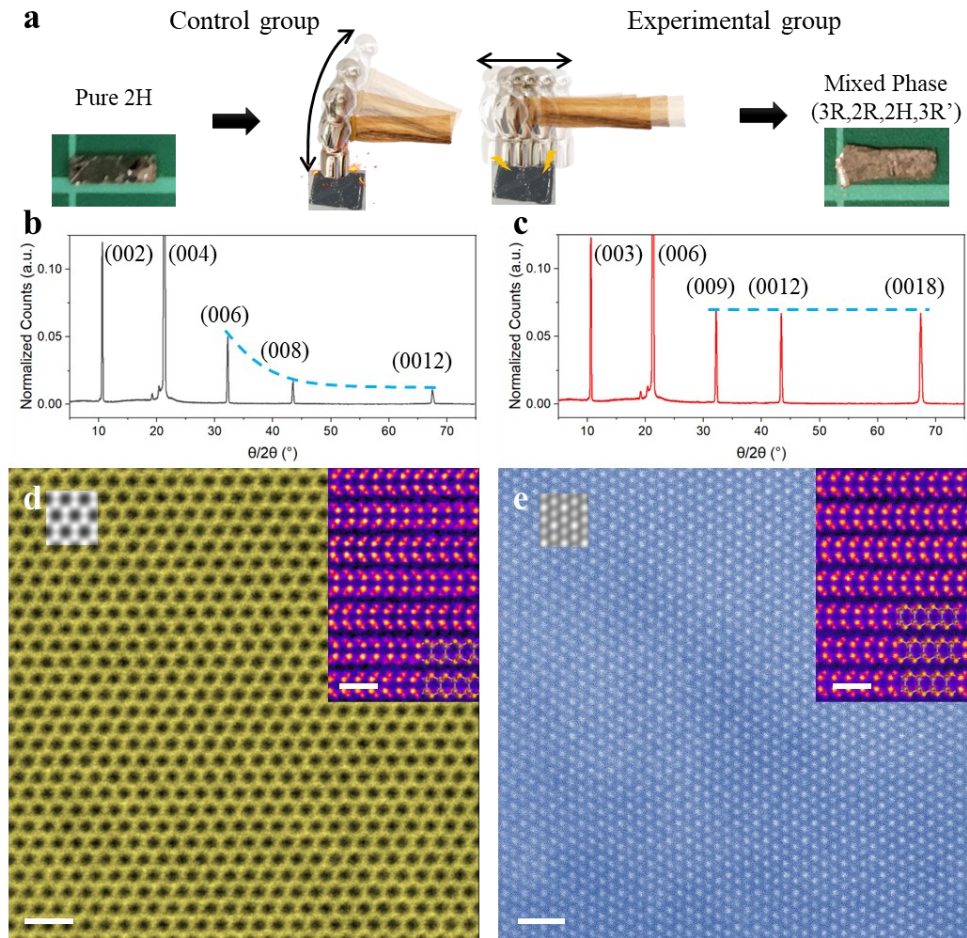
$$\nu = (3B - 2G)/[2(3B + G)] \quad \text{eq. 41}$$

The Vickers hardness ( $H_v$ ) is simply estimated by<sup>258</sup>,

$$H_v = 0.151G \quad \text{eq. 42}$$

### 4.3. Results

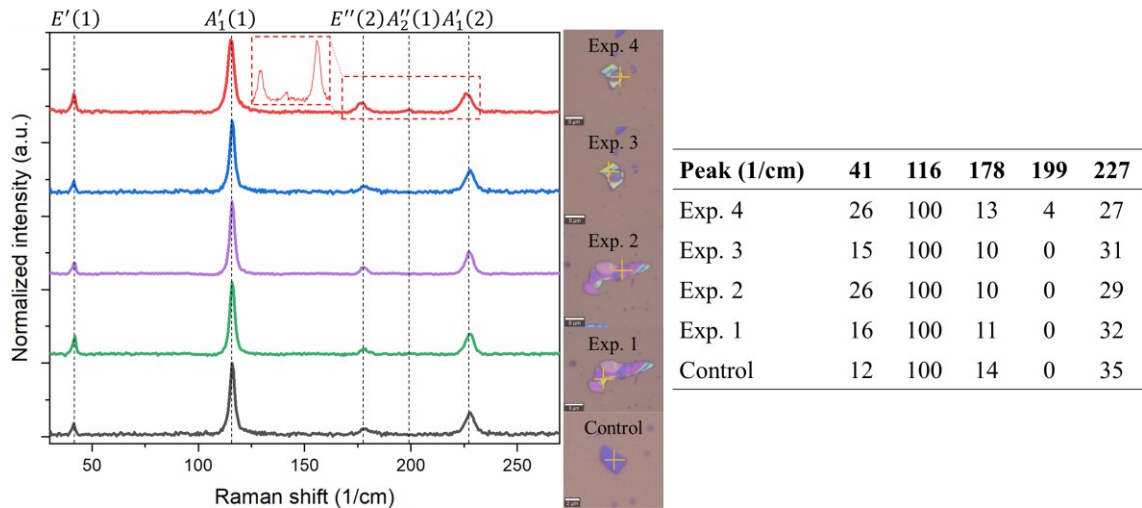
In following experiments, the single crystal 2H-InSe bulk is mechanically deformed (see session 4.2.1 and Figure 57a). The compressive and uniaxial shear forces applied on the single crystal result in significant plastic deformation, and then the conventional mechanical exfoliation method by scotch tape is used to further thin down the crystals. A mild compressive and shear plastic deformation here will restore the intermediate stages during deformation and unveils the main plasticity mechanisms. First, according to the X-ray diffraction (XRD) results on the post-deformation samples, we can clearly identify signatures of phase transition. The original 2H-InSe single crystal is transformed to InSe polymorph with mainly 3R phase (Figure 57b-e). The peak ratios of 3 major peaks, highlighted by light blue dashed lines, show significant changes from pristine samples. This observed phase transition is mainly driven by mechanical force here, rather than by thermal treatments in previous literatures<sup>44,259,260</sup>. The plane-view and cross-section scanning transmission electron microscopy high-angle annular dark-field (STEM-HAADF) images have an excellent agreement with the XRD results (Figure 57b-e). The pristine control group shows clean 2H stacking and the experiment group upon plastic deformation shows much more 3R structures. The STEM-HAADF images for the two phases match with their corresponding atomic models (Figure 57d-e), that 3 and 4 atomic columns can be seen in 2H and 3R stacking along a unit of arm-chair direction, respectively.



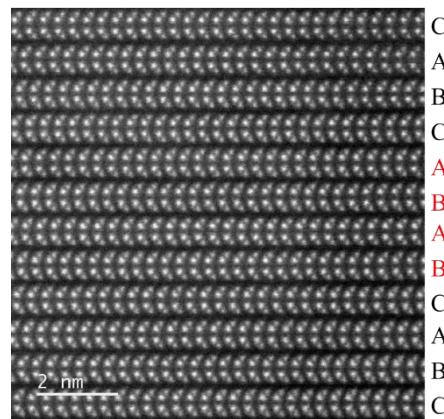
**Figure 57. The structural change of 2H-InSe after mechanical deformation.** **a**, The experimental workflow. **b,c**, XRD result of control group (before deformation) (**b**), and experimental group (with deformation) (**c**). The light blue dashed lines highlight the differences between (**b**) and (**c**). **d,e**, High resolution STEM-HAADF images in zone axis of  $[0001]$  and  $[1\bar{2}10]$  of the control group (**d**), and the experimental group (**e**), showing 2H and 3R stacking, respectively. Insets in (**d,e**), STEM simulation images. Scale bars: 1 nm.

Meanwhile, Figure 58 shows our Raman spectroscopy data does not show extra peak for 2H phase and 3R phase InSe with respect to control and Exp. 1-3, respectively. Exp. 1-4 are the same batch of exfoliated InSe after loading with different laser exciting positions, indicated by the orange crosses. It can be distinguished by the peak ratios of  $E'(1)$  and  $E''(2)$ .  $E'(1)$  peak is higher than  $E''(2)$  peak in 3R phase, but lower or similar to 2H phase. However, only the red dashed box in Exp. 4 displays a red shift with an extra peak that attributes to some local 2R phase, which can be recognized as the stacking faults

in 3R phase<sup>261,262</sup>, and it is also verified by the cross-section STEM results shown in Figure 59.



**Figure 58. Raman spectra with corresponding optical images and a table of normalized peak intensity (%).** The orange crosses in the optical images indicate the laser excited position.

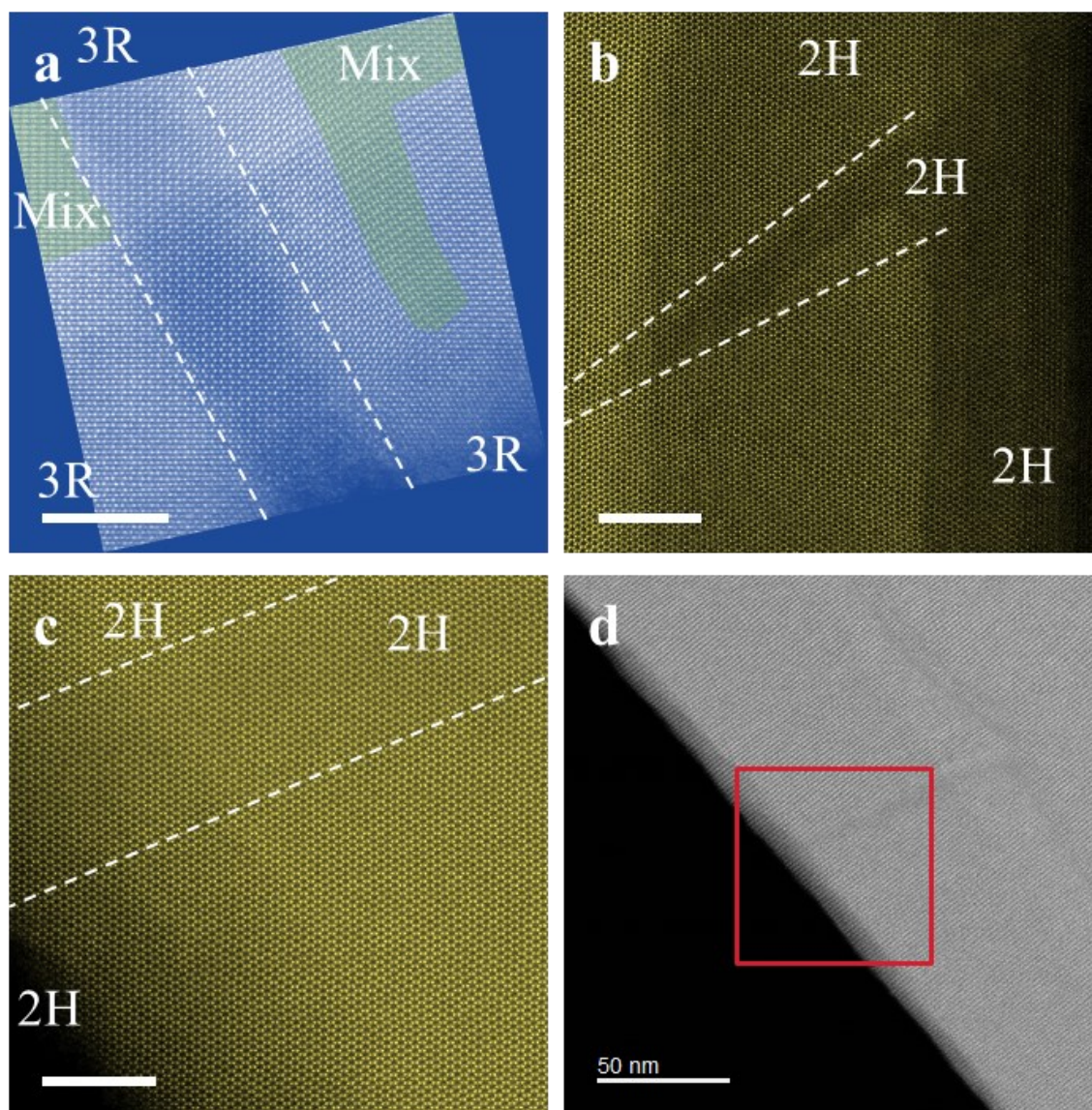


**Figure 59. Example of stacking fault of 2R phase InSe in between 3R phase InSe.**

#### 4.3.1. The atomic structures close to micro-cracks

As observed by TEM, micro-cracks can be created under deformation. In comparisons between InSe, MoS<sub>2</sub> and MoTe<sub>2</sub> specimens, Figure 60a-c show InSe transits to 3R phase with mixed phase (highlighted by green areas), but MoS<sub>2</sub> and MoTe<sub>2</sub> retain 2H phase (micro-crack is highlighted in between a pair of white dashed lines; detailed structural models of MX and MX<sub>2</sub> have been mentioned in Figure 56 in session 4.1, and the micro-crack of MoTe<sub>2</sub> can be observed in lower magnification in Figure 60d).

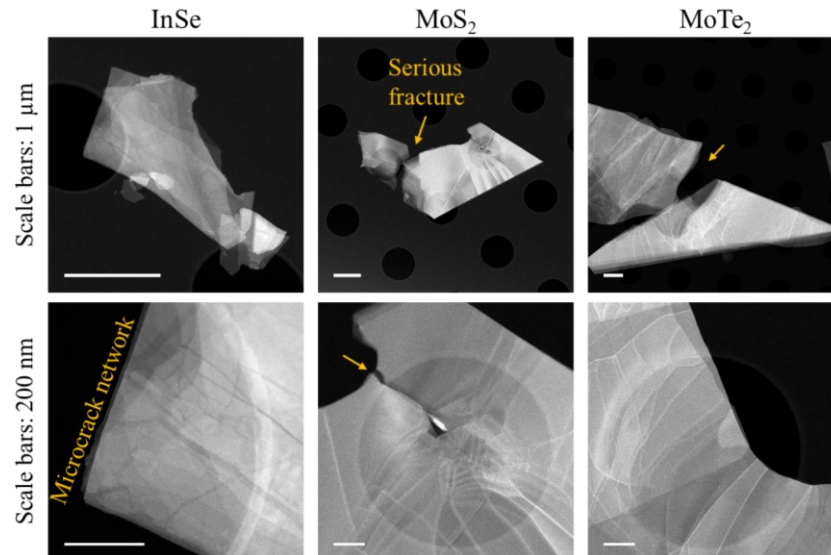




**Figure 60. Atomic structures near micro-cracks along [0001]. a, InSe. b, MoS<sub>2</sub>. c, MoTe<sub>2</sub>. Scale bars: (a-c) 5 nm. d, Corresponding low magnification of (c) highlighted by the red box.**

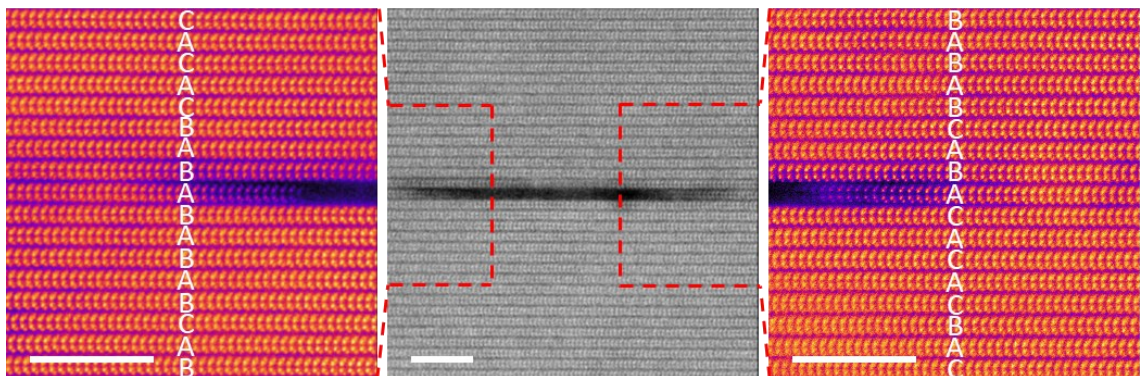
In typical low magnification STEM-HAADF images after deformation, InSe shows numerous few layer intralayer micro-cracks with less dislocation lines compared with MoS<sub>2</sub> and MoTe<sub>2</sub> (Figure 61). These results indicate that InSe releases much strain by forming micro-cracks associated with phase transition, which is distinct from MoS<sub>2</sub> and MoTe<sub>2</sub>. Since much more micro-cracks are observed in InSe, the crack propagation perpendicular to the basal plane which leads to macroscopic failure is clearly suppressed.

On the contrary,  $\text{MoX}_2$  prefer accumulating dislocations. Once the strain is unaffordable, the serious fracture would be formed, and the strain can be finally relaxed.



**Figure 61. Typical low magnification STEM-HAADF images after deformation of InSe,  $\text{MoS}_2$  and  $\text{MoTe}_2$ .**

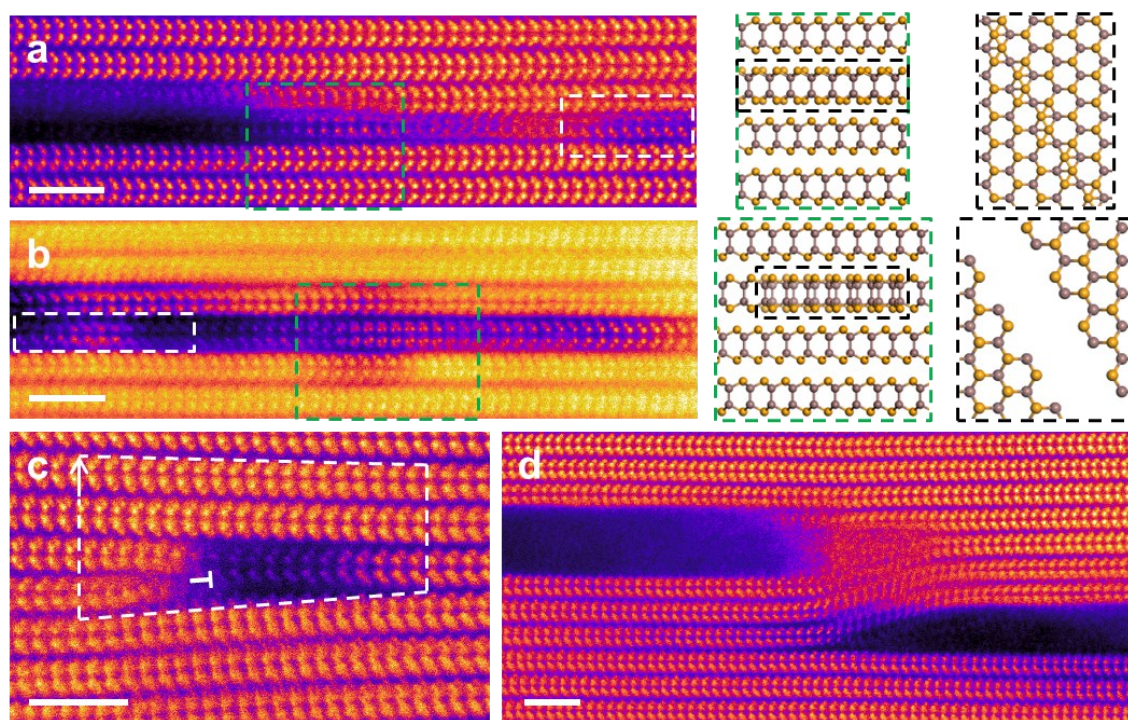
Figure 62 displays a typical single layer (1L) micro-crack STEM image where only one layer of InSe breaks without dislocation. The noted stacking order indicates 2R and 3R phases are formed near the crack in the pristine 2H sample. The micro-cracks can also occur in InSe multilayer surrounded by mainly 3R phase, followed by 2R phase as shown in Figure 62. These cross-section TEM results are in line with the above analysis that more 3R phase is formed after mechanical deformation.



**Figure 62. Cross-section HAADF-STEM images of a typical single layer (1L) micro-crack without dislocation along  $[1\bar{2}10]$ .** Scale bars: 5 nm. The red dashed lines indicate the enlarged view, the layer stacking order is marked.



With careful inspection on the post-deformation specimens, other phase transition  $3R'$  phase, intralayer phase boundaries, a cross-layer joint of micro-cracks, and  $1/3\vec{z}$  edge dislocation can be also observed in InSe specimens (Figure 63). Figure 63a&b present the phase boundaries before and after intralayer cracking. Part of the  $2H$ -InSe is transformed to  $3R$ -InSe showing in the model in the green dashed boxes, and there is also  $3R'$ -InSe part as indicated by the white dashed boxes. The results imply that the  $3R'$  phase might be the intermediate stage of intralayer gliding on the phase transition pathway from  $2H$ -to- $3R$ . This transition is thermodynamically reversible, however, due to the different kinetic energy upon interlayer sliding which will be presented later, the  $3R$  phase is more favorable.

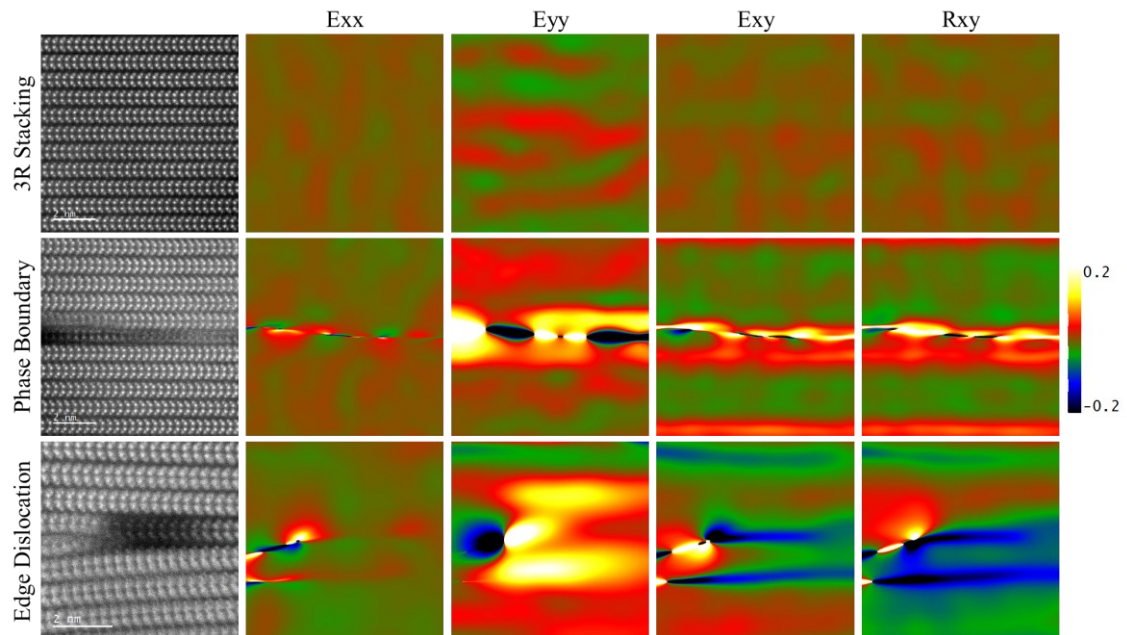


**Figure 63.** Cross-section HAADF-STEM images of post-deformation specimens. **a,b**, Phase boundaries **(a)** before and **(b)** after intralayer crack with phase transitions intermediate state  $3R'$  phase. The white dashed boxes indicate the local  $3R'$  InSe, the green dashed boxes model the sideview and the black dashed boxes show the corresponding projection view in **(a&b)**. **c**, One micro-crack forms  $1/3\vec{z}$  edge dislocation. **d**, Interlayer and intralayer reconnection. Scale bars: 2 nm.

From structural perspective, the emerged 3R phase in InSe cannot be simply caused by interlayer gliding along the energy favorable axis such as  $\langle 10\bar{1}0 \rangle$  or  $\langle 1\bar{2}10 \rangle$ , instead, the intralayer reconstruction is necessary. According to our density functional theory (DFT) calculation, the formation energy of 2H and 3R is very close, -0.743, and -0.746 eV/atom (Table 2), respectively, which explains the co-existed phases, such that there are 2H, 2R, 3R, and 3R' phases in InSe. The slightly lower energy in 3R phases also implies a stronger inter-layer interaction in 3R phase than 2H phase, which is also in agreement with exfoliation energy difference for the two phases (0.29, and 0.30 J/m<sup>2</sup> for 2H and 3R phase, respectively).

**Table 2. Exfoliation energy and formation energy**

	Exfoliation energy (J/m <sup>2</sup> )	Formation energy (eV/atom)
3R-InSe	0.30	-0.746
2H-InSe	0.29	-0.743
2H-MoS <sub>2</sub>	0.52	-1.202



**Figure 64. Strain analysis by geometric phase analysis of completely transformed 3R region, phase boundary and edge dislocation. Scale bars: 2 nm.**





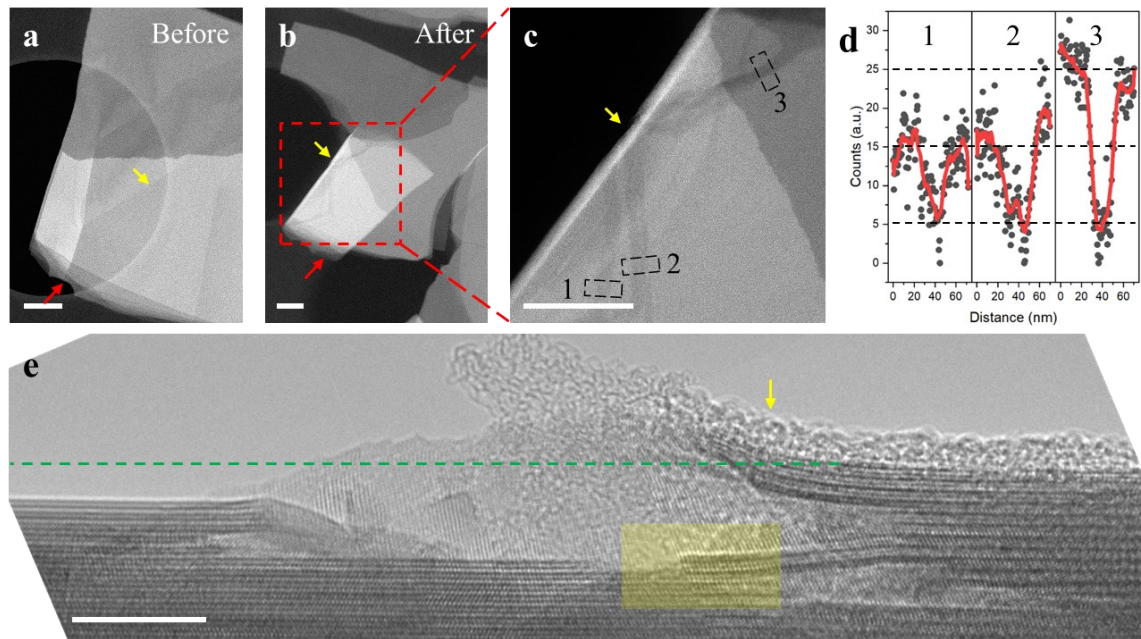
Other than strain concentrated high energy phase boundary induced micro-cracks, edge dislocations like  $\vec{b} = 1/3\vec{z}$  can also initiate micro-cracks at the high energy zones (Figure 63c). The phase boundaries and edge dislocations are highly strained area incubating micro-cracks, see geometric phase analysis results in Figure 64. After prevailed generation, the suddenly ceased extension of these micro-cracks is owing to the much higher energy barrier for the gliding in 3R stacking (see later discussion).

Interestingly, the micro-cracks in different layers can combine and automatically stop the propagation of each other due to their highly flexible nature. Usually, coalescence of cracks will bring catastrophic failure, but in InSe the micro-cracks in different layers can self-collectively form a stable network. Figure 63d shows that a cross-layer joint of two micro-cracks connecting 3L InSe prevents micro-cracks further propagation. Until here we have clarified the correlated micro-cracks and phase transition is the key to the high plasticity of InSe and distinguish it from other brittle vdW layered materials.

### 4.3.2. Mechanical manipulations by *in situ* TEM

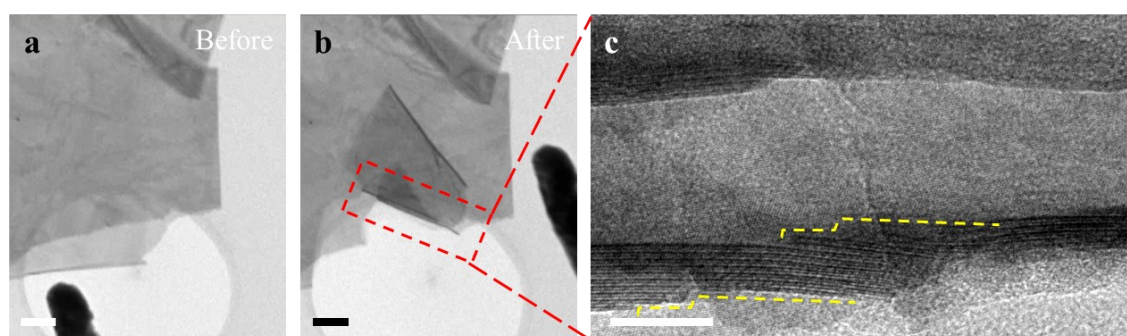
In order to gain deep insight into the plastic deformation of 2H-InSe, *in situ* TEM bending experiments were implemented (Figure 65). We expect that plastic deformation could occur in those highly bended zones. Herein, an InSe flake with dislocation lines was bent by the nanomanipulator with a tungsten tip (method see session 4.2.4). Two emerged dislocation lines are tracked by yellow and red arrows as shown in Figure 65a&b. One crack is initiated at the dislocation position marked by the yellow arrows. The intralayer micro-cracks are obviously created by the concentrated strain. Notably, the induced interlayer gliding can also eliminate the dislocation marked by the red arrows. The strain is prone to be relaxed by the interlayer gliding after micro-crack formation. Similar to the case in Figure 63d, a cross-layer joint pair of micro-cracks is found in

Figure 65c&e, as highlighted by yellow color. The thickness of the intralayer cracks that continuously fracture along  $\vec{z}$  direction can be defined by the layer numbers, which can be determined by the contrast in STEM-HAADF images (Figure 65b-e & method see session 4.2.5). The thickness of the intralayer micro-cracks changes from 4L to a pair of 2L micro-cracks. An outmost fracture labeled by green dashed line is created during the *in situ* bending (Supplementary Video 1@2:11). The thickness estimated by STEM-HAADF intensity is accurate for thin specimen like InSe in this study<sup>263</sup>. Thus, here we also show that the propagation of micro-cracks can be stopped when they meet, therefore numerous nanometre (nm)-width micro-cracks without further expansion and forming a micro-crack network in InSe can be clearly seen in low magnification HAADF-STEM (Figure 61).



**Figure 65.** *In situ* TEM bending experiment of 2H-InSe. **a-c**, STEM-HAADF images **(a)** before, and **(b,c)** after *in situ* bending experiment. **c**, Enlarged view of red dashed box in **(b)**. **d**, The line profiles of corresponding numbers in **(c)** for thickness estimation. **e**, Merged HRTEM image with respect to **(b,c)**. An outmost fracture during *in situ* bending experiment is indicated by green dashed line (Supplementary Video 1) and a cross-layer joint of micro-cracks is highlighted by the yellow area. The yellow and red arrows track two dislocations in **(a-c&e)**.

Achieving excellent compression ratio ( $>4000\%^{92}$ ) needs to reduce the number of layers of vdW materials without macroscopic fracture. The secret for preventing complete interlayer fracture is uncovered by our *in situ* TEM, that InSe re-attaches not only with the adjacent interlayer, but also easily with the completely fractured parts (Figure 66). A pair of green dashed lines demonstrate the original connection (Figure 66h). The strong interfacial energy here contributes to the stability of the layered structure during the lateral expansion of micro-cracks, and upon gliding, the newly extracted layers are able to keep the integrity of the structure.

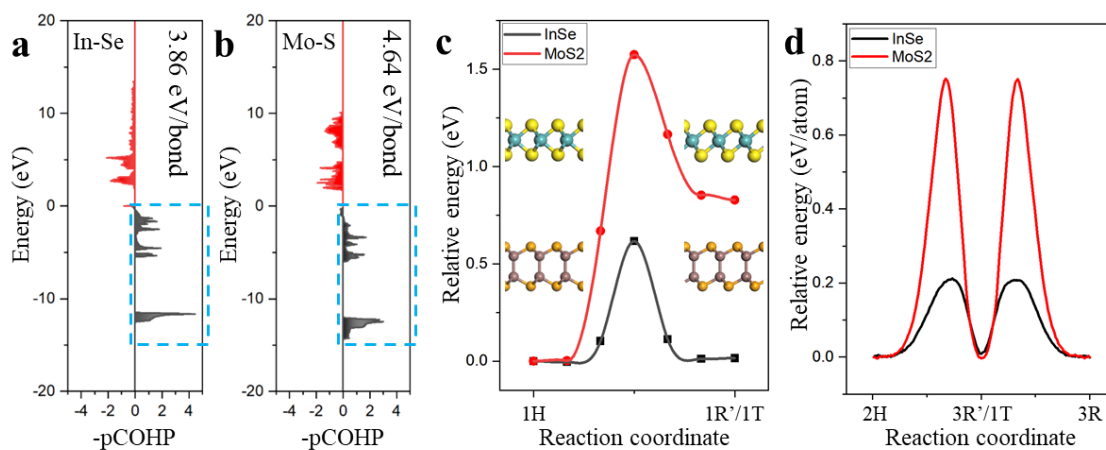


**Figure 66. Second example of *in situ* TEM bending experiment of 2H-InSe.** a,b, Another set of *in situ* bending experiment. Snapshots before (a) and after (b&c) *in situ* experiment with corresponding HRTEM image (c) indicated by red dashed box in (b). A pair of yellow dashed lines indicate the original position of the edges before vertical fracture in (c). Scale bars: 200 nm (a,b) and 10 nm (c).

### 4.3.3. Phase transition barrier and interlayer gliding barrier

In order to examine the physical origin which prevents the interlayer propagation of micro-cracks in 2H-InSe, we have performed in-depth first-principles calculations. First, to evaluate the bonding strength of MX and MX<sub>2</sub>, we have calculated their bonding energy. It is noted that the phase transition requires lattice rotation or X atom translation. Without thermal treatment, X atom translation is preferred under deformation, and each translation requires breaking one intralayer M-X bond and translating a X atom along  $1/3(10\bar{1}0)$ . Thus, the bonding strengths of 2H-InSe and MoS<sub>2</sub> were examined by crystal orbital Hamilton populations (COHP). As shown in Figure 67a-b, the bonding strength

of In-Se ( $\sim 3.86$  eV/bond) is found weaker than that of Mo-S ( $\sim 4.64$  eV/bond). This indicates the breaking of In-Se bonds in InSe is relatively easier than MoS<sub>2</sub>, which facilitates the movement of Se atoms and eventually the change of atomic stacking.



**Figure 67. Theoretical calculations.** **a-c**, First-principles calculations of intralayer bonding strength and 1L phase transition barrier. -pCOHP for intralayer bonding of (a) In-Se, and (b) Mo-S. The integrated areas and the integrated bonding strengths are marked in the light blue dashed boxes in (a&b). **c**, 1L phase transition energy barrier for InSe (1H-to-1R') and MoS<sub>2</sub> (1H-to-1T) with schematics of the transition of chalcogen atoms. **d**, LAMMPS simulations of two steps phase transition of a 3L model for InSe (2H-to-3R'-to-3R) and MoS<sub>2</sub> (2H-to-1T-to-3R).

Second, to evaluate the energy barriers of phase transition and interlayer gliding for both 2H and 3R MX and MX<sub>2</sub>, we have performed molecular dynamics simulations (method see session 4.2.7). Those phase boundaries with significant local strain eventually leads the intralayer fracture (micro-cracks). In terms of external stress, phase transition occurs near micro-cracks in InSe more easily than that in MoS<sub>2</sub>, as evidenced by the 3R'-InSe observed in the experiment. This is further supported by our first-principles calculation, as the calculated energy barrier for translating X atom in 1L InSe ( $\sim 0.616$  eV) is much smaller than that in 1L MoS<sub>2</sub> ( $\sim 1.575$  eV) as shown in Figure 67c. The transition energy is only from mechanical force without any thermal energy, and hence the phase transition only occurs in InSe but not in MoS<sub>2</sub> and MoTe<sub>2</sub>. Furthermore, Figure 67d shows the energy barrier for the two-step phase transition of InSe (2H-to-3R'-



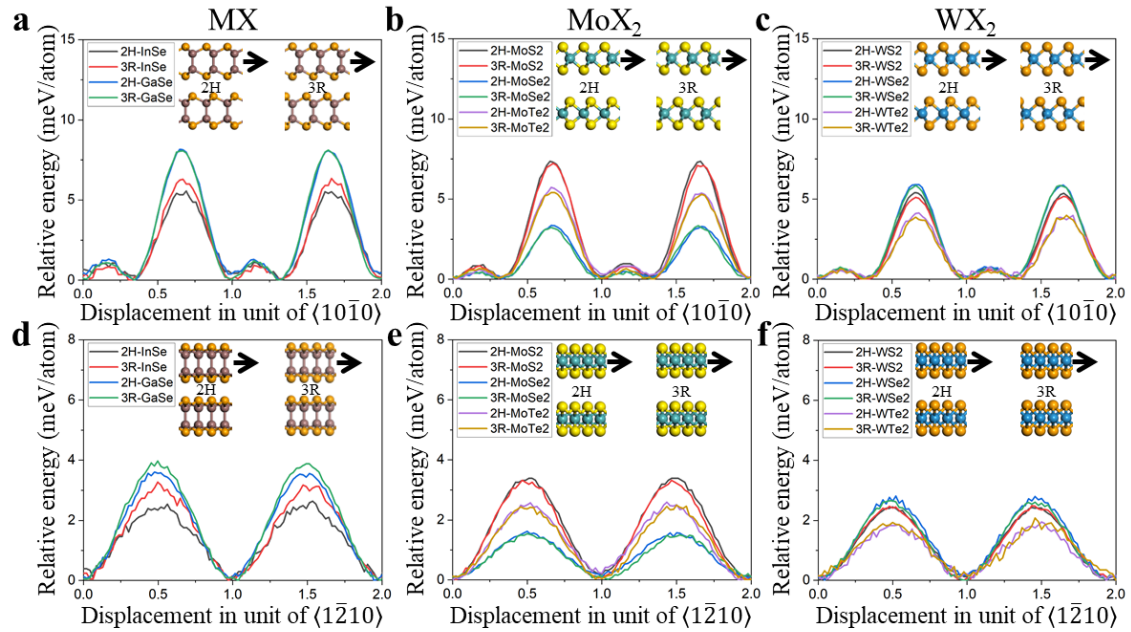
to-3R) and MoS<sub>2</sub> (2H-to-1T-to-3R) is in good agreement with the first-principles calculation and confirms that InSe has a much lower phase transition barrier than MoS<sub>2</sub>. For InSe, the energy barrier for the phase transition 2H-to-3R' is ~0.212 eV/atom, and it becomes ~0.199 eV/atom for 3R'-to-3R. In contrast, for MoS<sub>2</sub>, the energy barrier of phase transition 2H-to-1T is ~0.756 eV/atom, and it is ~0.755 eV/atom for 1T-to-3R. On the hand, 1L cleaving energies for 4-atom-thick InSe and 3-atom-thick MoS<sub>2</sub> along  $[\bar{1}\bar{2}10](0001)$  are ~0.338 eV<sup>92</sup> and ~0.150 eV<sup>92</sup>, respectively. Compared with the single chalcogens atom phase transition, InSe demonstrates the capability of phase transition (~0.21 eV/step), but MoS<sub>2</sub> is incapable (~0.76 eV/step). This comparison shows the reasons why we can observe 3R phases near the micro-crack in InSe (Figure 60), but MoX<sub>2</sub> only forms serious fracture (Figure 61). Besides, the results also demonstrate the 3R'-InSe can act as a transitional state between 2H-to-3R phase transition.

Third, the MD is applied to study the gliding barrier along energy favorable low index direction:  $\langle\bar{1}\bar{2}10\rangle$  and  $\langle10\bar{1}0\rangle$ . Our MD simulations indicate that the  $\langle\bar{1}\bar{2}10\rangle$  direction is more energetically favorable path for the interlayer gliding (Figure 68&Table 3). The gliding energy barrier of InSe is almost the same as MoS<sub>2</sub> in 2H stacking, implying the lubrication ability for InSe is similar to that of MoS<sub>2</sub>. However, among the various MX and MX<sub>2</sub> we studied here, only InSe has a significant increase of gliding energy barrier in between 2H and 3R stacking, which is 14.04 % along  $\langle10\bar{1}0\rangle$  direction and 24.07 % along  $\langle\bar{1}\bar{2}10\rangle$  direction. GaSe has *ca.* 10% differences in 2H and 3R gliding along  $\langle\bar{1}\bar{2}10\rangle$  direction, while all the other TMDCs have less than 6.5% energy barrier differences for 2H and 3R gliding. This is the reason why we can observe many stopped micro-crack surrounded by 3R phase and the GaSe also has relatively good plasticity like InSe<sup>264,265</sup>. The significant increment of the gliding barrier suppresses the further





propagation of the micro-crack, and then the strain would concentrate at other position. After the strain is relaxed by the micro-crack formation with phase transition, created micro-crack will be stopped eventually, and so on. Hence, the micro-crack network is formed and 3R-InSe acts as a pinning point here that suppress the propagation of micro-cracks as we have observed in Figure 60-Figure 63.



**Figure 68.** Relative gliding energy by molecular dynamics from LAMMPS. **a-f**, Relative gliding energy per atom of (a) MX, (b) MoX<sub>2</sub> and (c) WX<sub>2</sub> along  $\langle 10\bar{1}0 \rangle$ , and that of (d) MX, (e) MoX<sub>2</sub> and (f) WX<sub>2</sub> along  $\langle 1\bar{2}10 \rangle$ . Barrier values in (a-f) can be seen in Table 3.

**Table 3.** Gliding barrier along  $\langle 10\bar{1}0 \rangle$  and  $\langle 1\bar{2}10 \rangle$  directions

	$\langle 10\bar{1}0 \rangle$ (meV/atom)			$\langle 1\bar{2}10 \rangle$ (meV/atom)		
	2H	3R	% Diff.	2H	3R	% Diff.
InSe	5.566	6.348	14.04	2.637	3.271	24.07
GaSe	8.164	8.114	-0.6089	3.607	3.973	10.16
MoS <sub>2</sub>	7.357	7.227	-1.770	3.385	3.320	-1.923
MoSe <sub>2</sub>	3.356	3.340	-0.4656	1.622	1.523	-4.897
MoTe <sub>2</sub>	5.732	5.418	-5.479	2.593	2.492	-3.867
WS <sub>2</sub>	5.398	5.160	-4.399	2.447	2.490	1.764
WSe <sub>2</sub>	5.909	5.856	-0.9001	2.810	2.654	-5.583
WTe <sub>2</sub>	4.135	3.988	-3.544	1.950	2.078	6.561



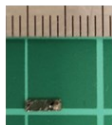
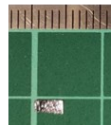
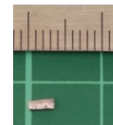
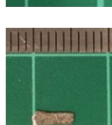



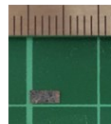




#### 4.3.4. Macroscopic view via elastic constants

After calculating the microscopic view, we have also studied the mechanical properties by calculating the elastic constants of InSe and MoS<sub>2</sub>. The calculated stiffness matrices of InSe and MoS<sub>2</sub> are summarized in Table 4. The incompressibility along basal plane and out-of-plane can be estimated by  $C_{11}$  and  $C_{33}$ , which implies that the deformation would be harder in 2H-MoS<sub>2</sub> ( $C_{11} \approx 235.1$  GPa;  $C_{33} \approx 65.5$  GPa;  $\epsilon_{xx} \approx 6.67\%$ ;  $\epsilon_{zz} \approx -6.67\%$ ) compared with 2H-InSe ( $C_{11} = 64.7$  GPa;  $C_{33} = 47.3$  GPa;  $\epsilon_{xx} \approx 16.09\%$ ;  $\epsilon_{zz} \approx -15.91\%$ ) under the same mechanical deformation, especially for the in-plane deformation. This agrees with the results in Figure 69. The difference of the in-plane shear deformation between 2H-InSe and 2H-MoS<sub>2</sub> can be further seen from the calculated  $C_{66}$ , which are 21.5, 89.7 GPa, respectively. That implies the possibility of the in-plane rotation is easier in 2H-InSe compared with 2H-MoS<sub>2</sub>. That implies the phase transition can be also caused by lattice rotation. However, the required energy of lattice rotation must be much higher than the phase transition caused by chalcogen atom translation. Besides, the shear moduli of 2H-InSe and MoS<sub>2</sub> are 15.1 and 46.5 GPa, respectively. The lower shear moduli in InSe indicates that it is more easily deformed without structural failure in response to the shear deformation. In addition, the structure hardness can be seen from the calculated Vickers hardness (Hv). For 3R-InSe, 2H-InSe, and 2H-MoS<sub>2</sub>, they are  $\sim 2.4$ ,  $\sim 2.3$ , and  $\sim 7.0$  GPa, respectively, demonstrating that InSe is much softer than MoS<sub>2</sub>. Soft crystals are generally ductile. Thus, from both microscopic- and macroscopic-view, InSe demonstrates better plasticity, as supported by the tensile test results for InSe ( $\sim 12\%$ <sup>92</sup>) and MoS<sub>2</sub> ( $\sim 9\%$ <sup>264</sup>). These first-principles calculations results agree with the experimental results and previous calculations.



**Table 4. DFT calculated elastic constants ( $C_{ij}$ ), bulk modulus (B), shear modulus (G), Young's modulus (E), Poisson ratio ( $\nu$ ), Vickers hardness (Hv), and Anisotropy index ( $A^L$ ) of 3R-InSe, 2H-InSe, and 2H-MoS<sub>2</sub>.**

Materials	3R-InSe	2H-InSe	2H-MoS <sub>2</sub>
$C_{11}$ (GPa)	65.7310	64.6741	235.1130
$C_{12}$ (GPa)	21.3761	21.7808	55.6896
$C_{13}$ (GPa)	14.1131	13.2617	11.1473
$C_{14}$ (GPa)	3.4500	0.0000	0.0000
$C_{33}$ (GPa)	37.1275	41.2595	65.4895
$C_{44}$ (GPa)	11.2887	9.4826	21.6482
$C_{66}$ (GPa)	22.1774	21.5316	89.7117
B (GPa)	28.3924	28.7132	63.3425
G (GPa)	15.7165	15.0827	46.5166
E (GPa)	39.8049	38.5058	112.1072
$\nu$	0.2663	0.2765	0.2050
Hv (GPa)	2.3732	2.2775	7.0240
$A^L$	0.3463	0.3543	1.1242

	InSe	MoS <sub>2</sub>	MoTe <sub>2</sub>		$\epsilon_{xx}(\pm 2\%)$	$\epsilon_{yy}(\pm 2\%)$	$\epsilon_{zz}(\pm 2\%)$
Before							
				InSe	16.09	3.82-54.78	-15.91
After				MoS <sub>2</sub>	6.67	2.86-3.33	-6.67
				MoTe <sub>2</sub>	1.40	3.97-5.34	-2.96

**Figure 69. Optical images and a table of estimated strain before and after compression and shear force.** The measured peak force of compression is 2.45 N and the peak normal shear force is 3.63 N. The strain rate is  $\sim 0.5/s$ .

#### 4.3.5. The origin of ultra-high plasticity

The previously overlooked gliding induced phase transition plays an important role. In our two-step phase transition model, the phase transition of 2H-to-3R' requires  $\sim 0.212$  eV/unit cell and that of 3R'-to-3R requires  $\sim 0.199$  eV/unit cell, that is lower than the 1L cleavage energy ( $\sim 0.338$  eV<sup>92</sup>). This brings a series of consequences, in which the

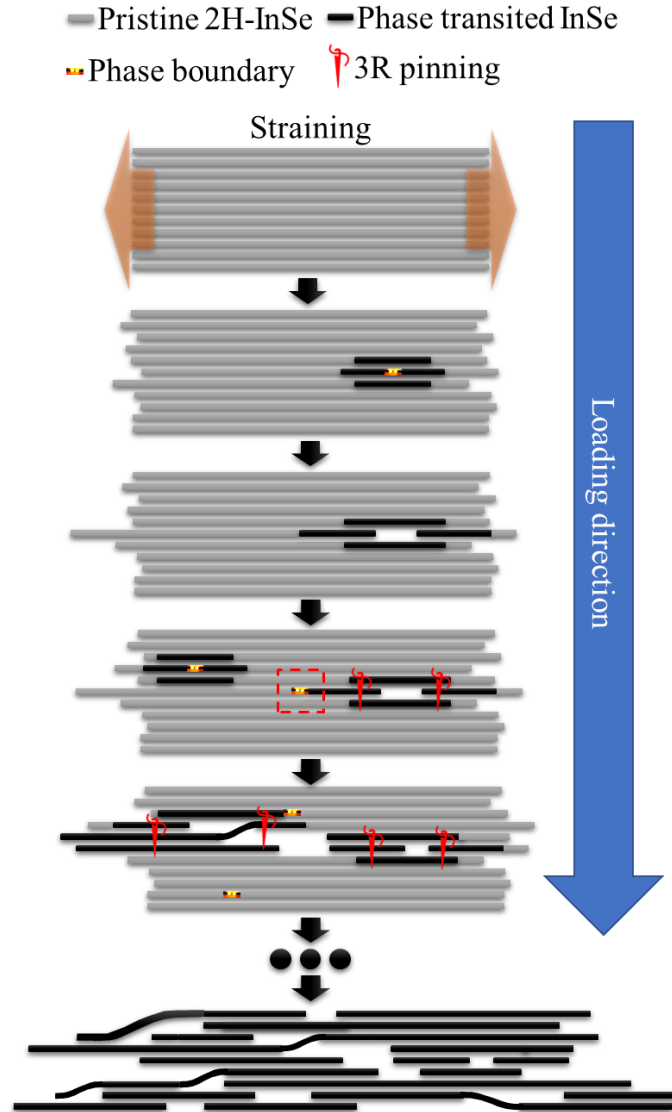


most important one is that the phase transition creates phase boundary where micro-cracks initiate/extend. Then the micro-cracks promote more degrees of freedom for interlayer gliding, and the ultra-plasticity loop is established.

Another main point is the microscale intralayer cracks do not extend in  $\vec{z}$  direction (vertical to the basal plane) or coalesce to form macroscopic fracture surfaces in InSe, because InSe does not accumulate dislocations, which are relaxed by micro-cracks and interlayer gliding as shown in the *in situ* experiment (Figure 65). The accumulation of dislocations causes eventually complete fracture that can be seen in the low magnification comparison between InSe, MoS<sub>2</sub>, and MoTe<sub>2</sub> (Figure 61). It is also relied on the phase transition in InSe that forming phase boundary, followed by micro-crack. Thus, strain would concentrate at other position when the strain is relaxed by the micro-crack. Besides, the micro-crack propagation is also gradually ceased by the 3R-InSe due to the stark contrast of 3R and 2H interlayer gliding barrier, that means 3R can act as “pinning points”. That is also why the 3R phase is tremendously arisen in the specimens. Therefore, the concept of “2H gliding and 3R pinning” around the micro-cracks holds the key for the ultra-plasticity of InSe.

Subsequently, large quantity of micro-cracks in different layers and different locations allow for the reorganization of layers under compression or tensile stress, resulting in the ultra-plastic behavior. So, the self-stabilized joint of 3R stacked micro-cracks not only avoids the complete fracture, but also forms micro-crack networks to strengthen the structure. So, here, a scheme of the mechanism of ultra-plasticity is illustrated in Figure 70. The ultra-plasticity is the synergetic effect of interlayer gliding, gliding induced phase transition, phase transition caused phase boundary, phase boundary concentrated strain relaxation micro-cracks, micro-crack propagation stopping 3R

pinning, and structure strengthening micro-crack networks. This virtuous circle facilitates the plasticity of materials.



**Figure 70. Schematic diagram of the mechanism of ultra-plasticity.**

#### 4.4. Summary

In short, we reveal that the intralayer micro-cracks associated with phase transition from 2H- to 3R-InSe are essential for the stress relaxation and the ultra-high plastic behavior. The abundant micro-cracks in 2H-InSe come from the stark differences between the gliding energy in different phases/stacking orders, i.e., 2H and 3R stackings. Because of the higher gliding energy in 3R phase and the 3R pinning effect, the micro-



cracks cannot coalesce or extend freely along  $\vec{z}$  direction, but mainly develop microscopic intralayer cracks distributed in different layers which eventually carry the ultra-high plastic strain via free-edge gliding and reorganization of fragmented layers. These new insights have clearly rationalized the superior plasticity in InSe over other vdW-layered materials. Similar materials with large gliding energy contrast in different phases, such as GaSe, could also be potential plastic semiconductors. These findings will open new directions for the mechanical engineering on the inorganic semiconducting crystals and will benefit the development of flexible electronic materials and solid-state lubricants.



## Chapter 5. Quantitative Charge Density Study of Hydrogen in MOFs

### 5.1. Introduction

Recent developed iDPC-STEM imaging technique<sup>157,158</sup> provides an opportunity to acquire light elements with better contrast and SNR than ABF-STEM<sup>103</sup>. Other than just imaging, iDPC-STEM can have a quantitatively study about the local electric field and projected charge density of the materials, if there are enough references of 4D-STEM dataset. Although iDPC-STEM facilitates acquiring light elements, imaging biomolecules in atomic scale like DNA is still challenging in TEM due to the irradiation damage. Combining iDPC-STEM with monochromator and high-speed camera can minimize the dose onto beam sensitive materials: MOFs<sup>109-111</sup>.

Recently, MOFs demonstrate high potential electrocatalysis ability in terms of HER and OER due to their flexibly porous structure, that provide sufficient catalytic sites<sup>112</sup>. In the recent work of OER MOFs<sup>50</sup>, the performance of Ni-BDC has been increased better than the commercial product RuO<sub>2</sub> via understanding the doping ion and ligand doping by using iDPC-STEM. The localized lattice strain was induced by introducing 2-aminoterephthalate (ATA) ligands or Fe<sup>3+</sup> ions into Ni-BDC that provides three advantages: (1) Dramatically improving the weak electrical conductivity of MOFs. (2) Increasing the catalytic sites due to the defective hierarchical porous structure. (3) Promoting mass permeability of conductive Ni@C by using mild heat treatment to relax the doping induced strain.



The structure of MOFs usually based on the estimation by XRD with DFT optimization in the past. However, the accurate atomic structure only can be unveiled by direct observation experiments. Here, certain Ni-BDC structure from CCDC<sup>266</sup> were used to model our direct observation of Ni-BDC for further theoretical calculation and image simulation. Further, the application of charge density was studied quantitatively by dDPC-STEM in terms of C-H, N-H and O-H bonds.

## 5.2. Methodology

### 5.2.1. Specimen preparations

2-Aminoterephthalate ( $\text{H}_2\text{ATA}$ ) and 1,4-Benzenedicarboxylic acid ( $\text{H}_2\text{BDC}$ ) were purchased from Sigma Aldrich Co.  $\text{NiCl}_2 \cdot 6\text{H}_2\text{O}$ ,  $\text{FeCl}_2 \cdot 4\text{H}_2\text{O}$  and KOH were purchased from Aladdin Co. All the reagents were used directly without further purifications. Ni-BDC was prepared by following the previously reported procedures with slight modifications<sup>267</sup>. Typically,  $\text{H}_2\text{BDC}$  (124.6 mg, 0.75 mmol) and  $\text{NiCl}_2 \cdot 6\text{H}_2\text{O}$  (178.3 mg, 0.75 mmol) were dissolved in a mixture of 32 mL of dimethylformamide (DMF), 2 mL EtOH and 2 mL  $\text{H}_2\text{O}$ . The above mixture was stirred at room temperature for 5 min to dissolve the reagents. Subsequently, the solution was transferred to 100 mL Teflon liner, followed by reacting at 140 °C for 48 h. After cooling down, the resultant suspension was filtered, washed with ethanol for six time and dried at 60 °C to obtain the light green product.

### 5.2.2. STEM characterization

The atomic images of ADF-, iDPC-, dDPC-STEM images were captured under a Cs-corrected STEM (Thermo Scientific™ Spectra 300 S/TEM) operated at 300 kV. The collection angles of iDPC-STEM and ADF-STEM were set as 4 to 17 mrad, and 18 to



110 mrad, respectively. Electron probe was optimized by a DCOR and spherical aberration corrector via a standard gold sample before observations. The corresponding corrector parameters as follow: WD: 47.8  $\mu\text{rad}$ ; (124.5°); C1: -270.6 pm; A1: 476.4 pm (-153.0°); A2: 27.58 nm (-10.9°); B2: 19.68 nm (-37.5°); C3: 743.6 nm; A3: 455.8 nm (-76.7°); S3 : 58.59 nm (96.3°); A4: 4.791  $\mu\text{m}$  (170.5°); D4: 3.321  $\mu\text{m}$  (154.0°); B4: 5.238  $\mu\text{m}$  (175.1°); C5: -1.083 mm; A5: 43.63  $\mu\text{m}$  (-100.6°); R5: 30.03  $\mu\text{m}$  (-65.0°); S5 78.31  $\mu\text{m}$  (-151.2°). The iDPC images were acquired by 4-segmented annular dark field detector. Low-frequency information was reduced by applying high-pass filter. The electron-beam current was reduced  $\leq 1$  pA by unfiltered monochromator. The maximum dwell time was 10  $\mu\text{s}$  and the minimum pixel size was 8.789 pm. Hence, the combination of the electron dose was  $\leq 1616 \text{ e}^-/\text{\AA}^2$  to compromise between imaging quality and sample integrity.

### 5.2.3. Density functional theory simulation

In this study, geometric and electronic properties of Ni-BDCs are obtained from spin-polarized density function theory (DFT) calculations by using the Vienna ab initio Simulation Package (VASP) program package<sup>202,203</sup> within the projector augmented wave (PAW)<sup>204</sup>. The exchange-correlation interactions are described with the generalized gradient approximation (GGA)<sup>205</sup> in the form of the Perdew, Burke, and Ernzerhof (PBE) functional<sup>206</sup>. The kinetic energy cutoff for the plane-wave basis set is chosen as 450 eV. The DFT-D3 scheme of Grimme for the vdW correction<sup>207</sup> is applied. The electronic SCF tolerance is set to 10<sup>-5</sup> eV. Fully relaxed geometries and lattice constant are obtained by optimizing all atomic positions until the Hellmann–Feynman forces are less than 0.02 eV/ $\text{\AA}$ . The k-points samplings with a Monkhorst-Pack scheme<sup>268</sup> are 1 $\times$ 7 $\times$ 2 for structural optimization and electron density distribution.





#### 5.2.4. DDPC-STEM image simulations

Dr. Probe<sup>247</sup> was used to simulate the dDPC-STEM images. The parameters are set same as the conditions mentioned in Session 5.2.2. The observation-based crystal information file was used for the multi-slice. Similarly, VASP is used to simulate the charge density of the model. The results from VASP are convoluted by the probe similar to our experimental conditions.

### 5.3. Results and discussion

#### 5.3.1. Modeling Ni-BDC by direct observation

First of all, the goal is to study charge density quantitatively by using dDPC-STEM, so a model of the specimens Ni-BDC is required for the theoretic calculations. Figure 71a-d shows the direct observation of Ni-BDC along [010] and [001]. The direct observations suggest there is a period of 4 Ni atoms in Ni-O chain to form up and down Ni-O chain along [010] projection view, so the benzene rings in between the Ni-O chain can be seen as up and down too along horizontal view (Figure 71a-c). The cross-section view along [001] show the benzene rings are almost perpendicular to the Ni-O framework (Figure 71d). In the orange dashed boxes, the view near a benzene ring is enlarged. Therefore, the reference crystal information file from CCDC 985792<sup>266</sup> has been edited and relaxed to create our own model which is P2/C symmetry with lattice parameters  $a = 12.300 \text{ \AA}$ ,  $b = 3.2087 \text{ \AA}$ ,  $c = 22.946 \text{ \AA}$ ,  $\alpha = 90^\circ$ ,  $\beta = 112.31^\circ$ , and  $\gamma = 90^\circ$  (Figure 71e-f).

The SNR comparison between ADF-STEM and iDPC-STEM well demonstrates the  $\sim Z^2$  and  $\sim Z$  contrast here (Figure 71a&b), that shows the advantage of iDPC-STEM in imaging MOFs because it can image the high Z metal and low Z organic compounds simultaneously. Under low dose conditions (total dose  $\leq 1600 \text{ e}^-/\text{\AA}^2$ ), the spatial

resolution is approximately 1.040 Å as shown in Figure 72. In addition, H position can be only found in dDPC-STEM with relatively low SNR. It provides an opportunity to study the charge density ( $\rho$ ) of H bonds by dDPC-STEM.

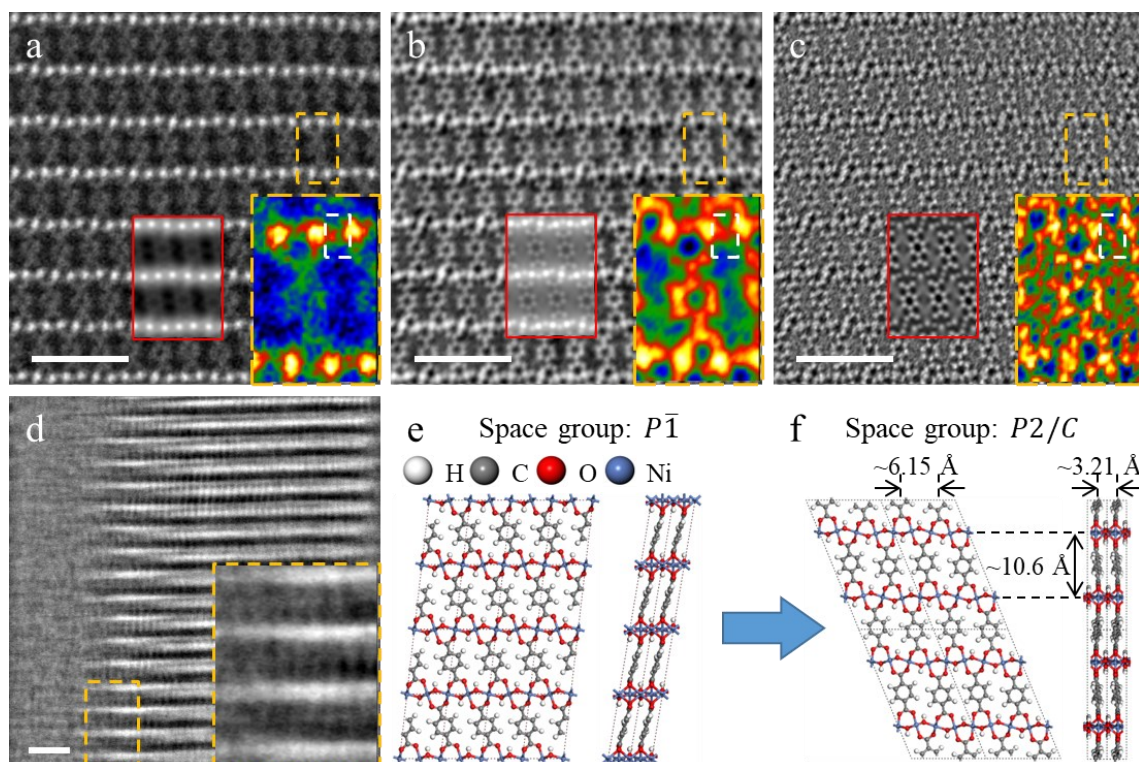


Figure 71. Modeling Ni-BDC by direct observations. a-c, Ni-BDC images along zone axis [010]. A, ADF-STEM image. b, iDPC-STEM image. c, Contrast inverted dDPC-STEM. D, iDPC-STEM image along [001]. Scale bars: 2 nm. Insets, red boxes in (a-c) indicate the simulated images, and the orange dashed boxes in (a-d) show the enlarged the view of a benzene ring. The white dashed boxes in (a-c) demonstrate O-H on the Ni-O chain. E, Similar model of Ni-BDC from CCDC: 985792<sup>266</sup>. F, Edited crystal structure suggested by direct observation along [010] and [001].

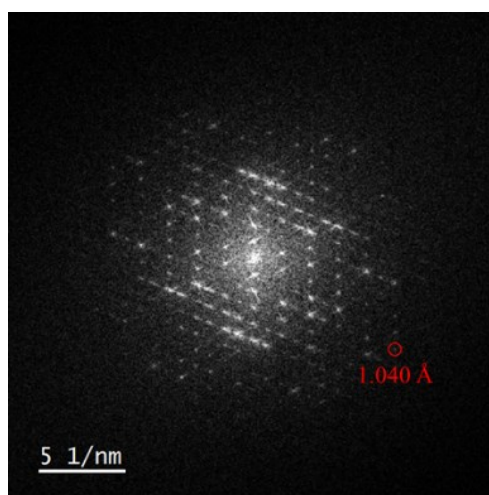
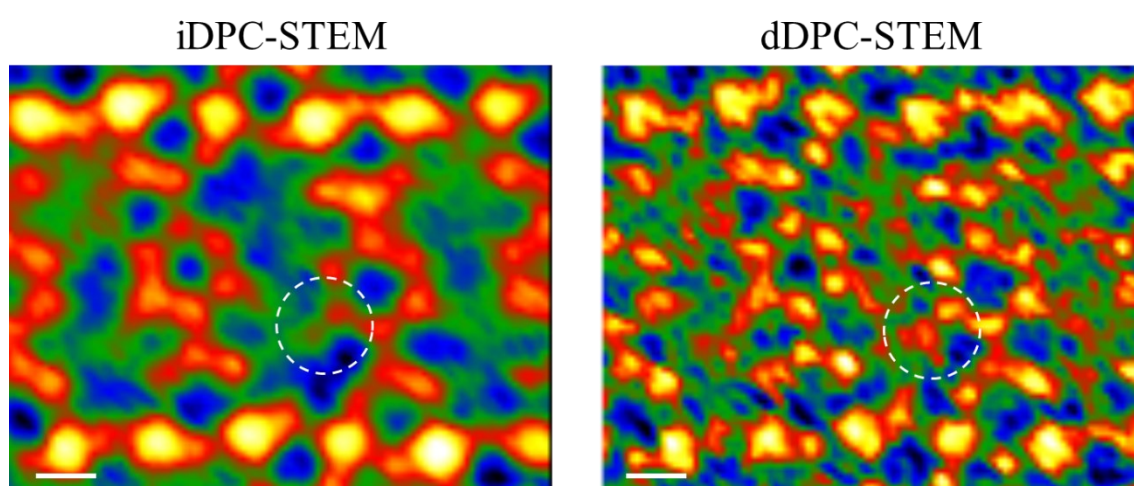


Figure 72. Spatial resolution by using corresponding FFT in Figure 71b.

### 5.3.2. Amino acid in Ni-BDC<sub>9</sub>ATA

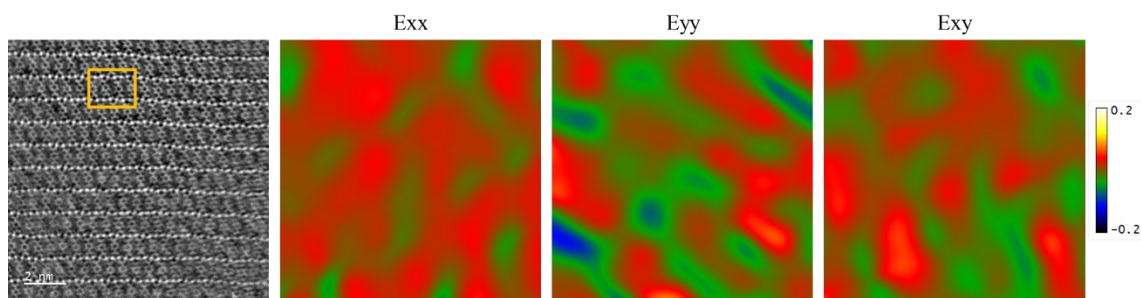
After modeling Ni-BDC, the ligands ratio of BDC:ATA = 9:1 is used to form the Ni-BDC<sub>9</sub>ATA MOFs. The ATA ligands contain one amino acid on the benzene rings, and hence the C-H, O-H, and N-H bonds can be quantitatively studied. Further, the orientation preference of the ATA ligands can be also investigated.

First, the best captured amino acid in Ni-BDC<sub>9</sub>ATA is shown in Figure 73. The nitrogen can be observed in iDPC-STEM, and the amino acid can be clearly shown in dDPC-STEM highlighted by the white dashed circles. However, the mixed ligands introduced strain into the structure, so there are few good regions of interest that can show amino acid as good as Figure 73. The geometric phase analysis (GPA) is applied to show the strain problem of the full field of view corresponding to the Figure 73 as shown in Figure 74. If the ratio of ATA ligands is too low, it is too difficult to find NH<sub>2</sub> in the specimen. If the ratio of ATA ligands is too high, the strain also affects the image quality. So, the ligands ratio is compromised between the number of ATA ligands and the introduction of strain.



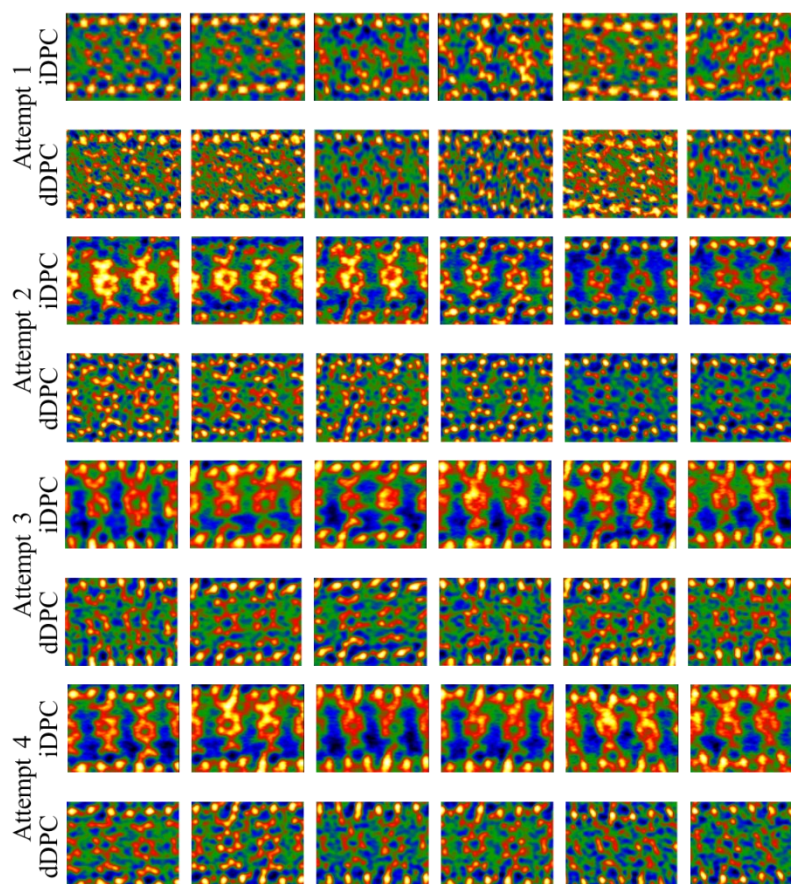
**Figure 73.** iDPC- and dDPC-STEM in Ni-BDC<sub>9</sub>ATA. Scale bars: 2 Å. White dashed circles highlighted the amino acid.





**Figure 74. GPA of the full field of view of Figure 73.** Orange box highlighted the corresponding position of Figure 73.

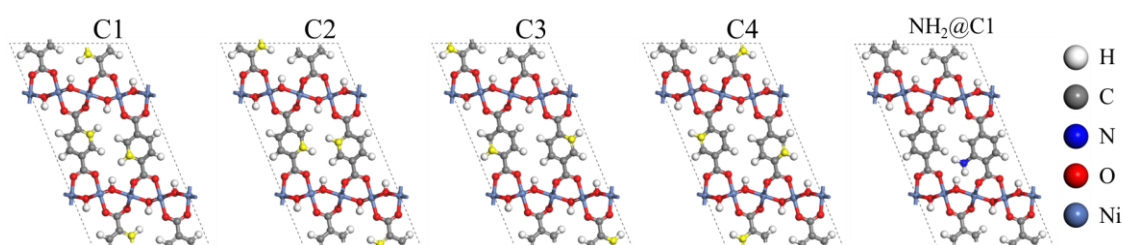
Based on the same strategy, the N atom is first distinguished in high SNR iDPC-STEM, then the amino acid is confirmed by low SNR dDPC-STEM. After tremendous efforts, the other amino acids are found in Figure 75. Although the quality amino acid is slightly worse than Figure 73, the amino acid can be barely identified and quantified. Before the orientation preference is discussed, the notation of the orientation will be denoted first.



**Figure 75. Other amino acids examples acquired by iDPC- and dDPC-STEM.** Field of views: 1.775 nm × 1.389 nm.

### 5.3.3. ATA orientation preference

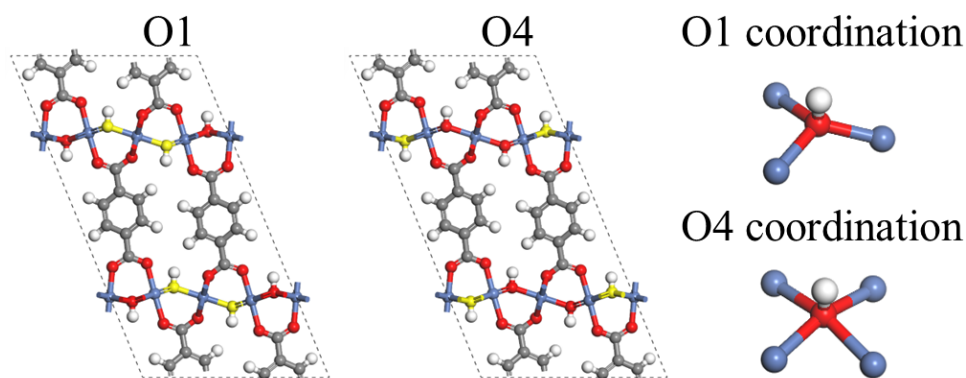
Figure 76 presents the notation C1 to C4 of the ATA ligand orientation with example of a relaxed  $\text{NH}_2@\text{C1}$  structure. The equivalent position of the same notation is highlighted by the yellow color. Combining the data above (Figure 73&Figure 75),  $\text{NH}_2@\text{C1}$  is found that mostly present (counts = 18) with the lowest relaxed energy, which means the  $\text{NH}_2@\text{C1}$  is an energy favorable position (Table 5). Other than the notation C1 to C4, there are also O1 and O4 that provide the coordination difference that O1 bonds with 3 Ni atoms and O4 bonds with 4 Ni atoms as shown in Figure 77.



**Figure 76.** Notation of the orientation of the ATA ligands with example. Yellow atoms show the equivalent position under the same notation.

**Table 5.** Table of counts and relaxed energy of different ATA orientation

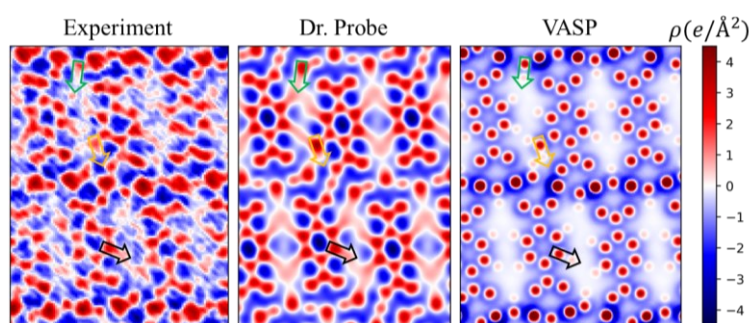
Orientation	Counts	$E_{\text{relaxed}}$ (eV)	$\Delta E_{\text{relaxed}}$ (eV)
$\text{NH}_2@\text{C1}$	18	-27178.1937	0
$\text{NH}_2@\text{C2}$	7	-27178.0717	0.1220
$\text{NH}_2@\text{C3}$	1	-27178.0937	0.1000
$\text{NH}_2@\text{C4}$	7	-27178.1243	0.0694



**Figure 77.** Notation of O1 and O4 showing different Ni coordination.

### 5.3.4. Quantitative study of the charge density with hydrogen

The line profiles extracted from experiments, Dr. Probe, and VASP simulations are statistically compared in terms of C-H, N-H (orange arrows), and O-H as shown in Figure 78. The black and green arrows demonstrate the examples of C2-H and O1-H line profile extraction. The sample size is as large as possible to minimize low SNR problem in dDPC-STEM, so the sample size is at least 100, except for the N-H (sample size = 22).



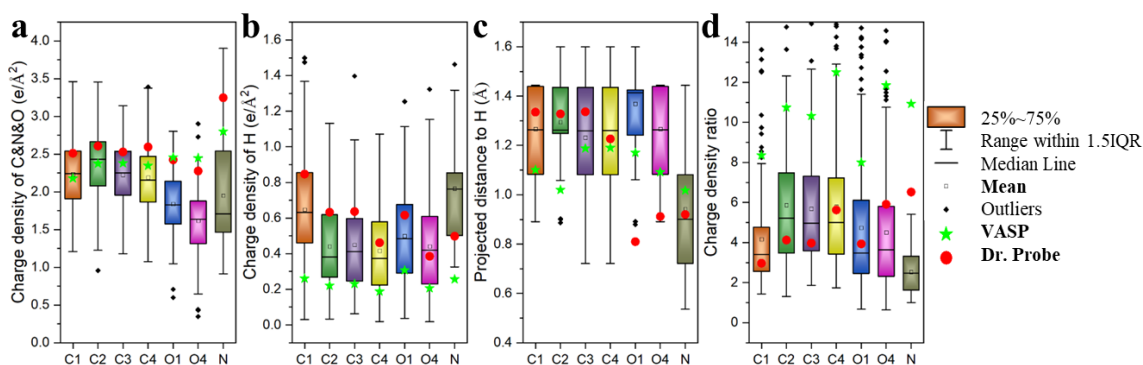
**Figure 78. Line profiles extraction from the charge density map in experiment, Dr. Probe and VASP.** Black, orange, and green arrows demonstrate how the line profiles are extracted for C-H, N-H, and O-H, respectively.

Figure 79 displays the statistic results that the theoretic results is close to the range of the statistical data. However, the low H intensity in VASP leads the huge difference in the final charge density ratio as shown in Figure 79b&d. It might be caused by the different potential used in the simulation<sup>269</sup>, but the used potential is as similar as possible in the Dr. Probe and VASP simulations. Noticeably, the charge density ratio of C/H and O/H is very similar, except for C1/H, which is similar to N-H. That coincides with the orientation preference of NH<sub>2</sub>@C1, that implies the orientation preference might be relevant to the similar charge density ratio. On the other hand, the charge density of H@C1 is higher than H@C2-C4, that implies the low energy bonding as shown in Figure 79b. When there is more interaction between the electron probe and H@C1, for example, low vibration and more stable, the scattering signal would be stronger. Besides, the charge density can relate to the coordination of O-H in the perspective of O1-H and O4-H (Figure





79a&b). The charge density of O1 and H@O1 is both higher than that of O4 and H@O4, that means the extra negatively charge from the Ni electron cloud reduces the charge density of O1 and H@O1 during the convolution between scanning probe and the charge. Besides, this is also why the charge density of O1 and O4 is generally lower than C1 to C4, that is about the coordination neighbor.



**Figure 79. Box charts of the charge density, atomic distance, and charge density ratio.** **a**, The charge density of C, N, or O. **b**, The charge density of H. **c**, The projected distance to H. **d**, The charge density ratio of C, N or O divided by H.

The projected atomic distance measured from dDPC-STEM is different because of the convolution and thermal vibration of the atoms. Hence, the highest positively charge position might be slightly adjusted after convolution, such that the peak distance extracted from the line profile is different. The mean of projected distance of C-H and O-H is approximate 1.25 Å, that is close to the simulations, but slightly longer than the previous studies. For example, the C-H bond length is ~1.079 Å in benzene<sup>270</sup>, and O-H bond length is ~0.95 Å in metal-OH<sup>271</sup>.

## 5.4. Summary

DPC-STEM provides the opportunity for structural identification and quantitative investigation in charge density in beam sensitive materials. Although the SNR of the charge density map is weak, the sufficient large sample size can minimize the data variation to achieve the quantitative investigation. In this work, the orientation preference



of amino acid has been found that prefers energy favorable position that is related to the H charge density, and the charge density ratio. The charge density can also represent the coordination difference because the total charge density is affected by convolution. If the electron cloud is larger, said high Z element, the signal difference would become larger. This work provides an alternative way to predict the ligands' arrangement in such flexibly complex structure of MOFs. This method also provides an insight to predict the structural engineering. Combining with the dDPC-STEM with big data, there will be more properties and applications of hydrogen bonds can be unveiled in the future.



## Chapter 6. Conclusion and Outlook

In this thesis, the applications of TEM have been demonstrated by 3 different projects. Taking the advantages of extremely high resolving power of TEM, the atomic structure can be relatively easily understood via direct observations. Coupling with the other techniques in TEM, such as EELS, *in situ* techniques, and dDPC-STEM, more information can be unveiled in real time, for example chemical structure, mechanical properties and mechanism, and charge density. The major findings of this thesis are concluded below.

The 2 step reactions and intermediate species of TMDCs have been resolved via the APCVD studies of ReSe<sub>2</sub>. The  $M_xX_{2x-n}$  clusters are first formed by the hydrogen reduced chalcogens and transition-metal in atmosphere. The clusters first nucleate on the surface for further chalcogenization to become  $MX_2$ , and then the further attached clusters either on the surface or on the edge will be gradually chalcogenized to form the 2<sup>nd</sup> layer or to grow epitaxially, respectively.

The phase transition pathway and “3R pinning effect” have been found via studying the exceptional plasticity of InSe. The unexpected atom translations induced phase transition from 2H-to-3R’-to 3R caused by solely mechanical driving force is rarely observed. The synergistic effects between enhanced gliding barrier and phase transition causes “3R pinning” which stops the cracks propagations, and the strain would be released by other micro-crack formation with the gradually forming micro-crack networks. Hence, this virtuous circle facilitates the plasticity of materials.

In the study of MOFs, iDPC-STEM has demonstrated the ability of structural analysis, and dDPC-STEM has demonstrated the resolving power on light elements and



the prediction of energy favorable site. The statistic results provide information of the number of atoms nearby due to the convolution of the total charge density. Furthermore, the higher charge density site implies the energy favorable possible when comparing with the same bonding structures.

Soon, the design of the *in situ* experiments is difficult because of the consideration of resolution, safety, and feasibility. Although the further selenization is confirmed, the process is still an attractive study. This idea can be implemented once there is a way to use the  $\text{H}_2\text{Se}$  gas in the Protochips atmosphere holder due to the gas is highly toxic and flammable.

The ductile brittle predictions still require giant efforts. Few data points of 2D materials have been contributed via DFT calculations to Pugh-Pettifor criteria that suggests the parabolic relations between Cauchy pressure-to-Young's modulus ratio and shear-to-bulk moduli. The Pugh criterion still works for vdW materials.

The recent developed iDPC-STEM has the great potential to image the biomolecule in RT. Although the DNA structure is well known, it is still worth a shot. The applications of dDPC-STEM are less reported. The successful prediction of the lower energy site motivates the further studies about the applications of dDPC-STEM for different low-dimensional materials.



# Appendices

1. Link of Supplementary Video 1: <https://youtu.be/UZbEuPliomY>



## Reference

- 1 Krättschmer, W., Lamb, L. D., Fostiropoulos, K. & Huffman, D. R. Solid C<sub>60</sub>: a new form of carbon. *Nature* **347**, 354-358 (1990). <https://doi.org/10.1038/347354a0>
- 2 Liu, Z. *et al.* Transmission Electron Microscopy Imaging of Individual Functional Groups of Fullerene Derivatives. *Physical Review Letters* **96**, 088304 (2006). <https://doi.org/10.1103/PhysRevLett.96.088304>
- 3 Iijima, S. Helical microtubules of graphitic carbon. *Nature* **354**, 56-58 (1991). <https://doi.org/10.1038/354056a0>
- 4 Guan, L., Suenaga, K. & Iijima, S. Smallest Carbon Nanotube Assigned with Atomic Resolution Accuracy. *Nano Letters* **8**, 459-462 (2008). <https://doi.org/10.1021/nl072396j>
- 5 Zhao, J. & Zhu, J. Electron microscopy and in situ testing of mechanical deformation of carbon nanotubes. *Micron* **42**, 663-679 (2011). [https://doi.org:https://doi.org/10.1016/j.micron.2011.04.004](https://doi.org/https://doi.org/10.1016/j.micron.2011.04.004)
- 6 Bachmatiuk, A. *et al.* Low Voltage Transmission Electron Microscopy of Graphene. *Small* **11**, 515-542 (2015). <https://doi.org:https://doi.org/10.1002/sml.201401804>
- 7 Novoselov, K. S. *et al.* Electric Field Effect in Atomically Thin Carbon Films. *Science* **306**, 666-669 (2004). <https://doi.org:doi:10.1126/science.1102896>
- 8 Zhao, J. *et al.* Free-Standing Single-Atom-Thick Iron Membranes Suspended in Graphene Pores. *Science* **343**, 1228-1232 (2014). <https://doi.org:doi:10.1126/science.1245273>
- 9 Zhao, J. *et al.* Two-dimensional membrane as elastic shell with proof on the folds revealed by three-dimensional atomic mapping. *Nature Communications* **6**, 8935 (2015). <https://doi.org/10.1038/ncomms9935>
- 10 Seol, J. H. *et al.* Two-Dimensional Phonon Transport in Supported Graphene. *Science* **328**, 213-216 (2010). <https://doi.org:doi:10.1126/science.1184014>
- 11 Lee, C., Wei, X., Kysar, J. W. & Hone, J. Measurement of the Elastic Properties and Intrinsic Strength of Monolayer Graphene. *Science* **321**, 385-388 (2008). <https://doi.org:doi:10.1126/science.1157996>
- 12 Bolotin, K. I. *et al.* Ultrahigh electron mobility in suspended graphene. *Solid State Communications* **146**, 351-355 (2008). <https://doi.org:https://doi.org/10.1016/j.ssc.2008.02.024>
- 13 Chen, J.-H., Jang, C., Xiao, S., Ishigami, M. & Fuhrer, M. S. Intrinsic and extrinsic performance limits of graphene devices on SiO<sub>2</sub>. *Nature Nanotechnology* **3**, 206-209 (2008). <https://doi.org/10.1038/nnano.2008.58>
- 14 Shin, D. H., Kim, J. M., Shin, S. H. & Choi, S.-H. Highly-flexible graphene transparent conductive electrode/perovskite solar cells with graphene quantum dots-doped PCBM electron transport layer. *Dyes and Pigments* **170**, 107630 (2019). <https://doi.org:https://doi.org/10.1016/j.dyepig.2019.107630>
- 15 Dellinger, A. *et al.* Application of fullerenes in nanomedicine: an update. *Nanomedicine* **8**, 1191-1208 (2013). <https://doi.org/10.2217/nnm.13.99>





- 16 Bakry, R. *et al.* Medicinal applications of fullerenes. *International Journal of Nanomedicine* **2**, 639-649 (2007). <https://doi.org:10.2147/IJN.S2.4.639>
- 17 Alshehri, R. *et al.* Carbon Nanotubes in Biomedical Applications: Factors, Mechanisms, and Remedies of Toxicity. *Journal of Medicinal Chemistry* **59**, 8149-8167 (2016). <https://doi.org:10.1021/acs.jmedchem.5b01770>
- 18 Chung, C. *et al.* Biomedical Applications of Graphene and Graphene Oxide. *Accounts of Chemical Research* **46**, 2211-2224 (2013). <https://doi.org:10.1021/ar300159f>
- 19 Priyadarsini, S., Mohanty, S., Mukherjee, S., Basu, S. & Mishra, M. Graphene and graphene oxide as nanomaterials for medicine and biology application. *Journal of Nanostructure in Chemistry* **8**, 123-137 (2018). <https://doi.org:10.1007/s40097-018-0265-6>
- 20 Gravel, E. & Doris, E. Fullerenes make copper catalysis better. *Science* **376**, 242-243 (2022). <https://doi.org:doi:10.1126/science.abo3155>
- 21 Felfli, Z., Suggs, K., Nicholas, N. & Msezane, A. Z. Fullerene Negative Ions: Formation and Catalysis. *International Journal of Molecular Sciences* **21**, 3159 (2020).
- 22 Gonçalves, L. P. L. *et al.* Understanding the importance of N-doping for CNT-supported Ni catalysts for CO<sub>2</sub> methanation. *Carbon* **195**, 35-43 (2022). <https://doi.org:https://doi.org/10.1016/j.carbon.2022.03.059>
- 23 Zhao, D. *et al.* Carbon nanotube-supported Cu-based catalysts for oxidative carbonylation of methanol to methyl carbonate: effect of nanotube pore size. *Catalysis Science & Technology* **10**, 2615-2626 (2020). <https://doi.org:10.1039/C9CY02407G>
- 24 Hu, K. *et al.* Catalytic activity of graphene-covered non-noble metals governed by proton penetration in electrochemical hydrogen evolution reaction. *Nature Communications* **12**, 203 (2021). <https://doi.org:10.1038/s41467-020-20503-7>
- 25 Chen, B. *et al.* Engineering the Active Sites of Graphene Catalyst: From CO<sub>2</sub> Activation to Activate Li-CO<sub>2</sub> Batteries. *ACS Nano* **15**, 9841-9850 (2021). <https://doi.org:10.1021/acsnano.1c00756>
- 26 Burkholder, M. B. *et al.* Metal supported graphene catalysis: A review on the benefits of nanoparticulate supported specialty sp<sup>2</sup> carbon catalysts on enhancing the activities of multiple chemical transformations. *Carbon Trends* **9**, 100196 (2022). <https://doi.org:https://doi.org/10.1016/j.cartre.2022.100196>
- 27 Cheng, P., Li, G., Zhan, X. & Yang, Y. Next-generation organic photovoltaics based on non-fullerene acceptors. *Nature Photonics* **12**, 131-142 (2018). <https://doi.org:10.1038/s41566-018-0104-9>
- 28 Wieland, L., Li, H., Rust, C., Chen, J. & Flavel, B. S. Carbon Nanotubes for Photovoltaics: From Lab to Industry. *Advanced Energy Materials* **11**, 2002880 (2021). <https://doi.org:https://doi.org/10.1002/aenm.202002880>
- 29 Das, S., Pandey, D., Thomas, J. & Roy, T. The Role of Graphene and Other 2D Materials in Solar Photovoltaics. *Advanced Materials* **31**, 1802722 (2019). <https://doi.org:https://doi.org/10.1002/adma.201802722>
- 30 Jiang, Z., Zhao, Y., Lu, X. & Xie, J. Fullerenes for rechargeable battery applications: Recent developments and future perspectives. *Journal of Energy Chemistry* **55**, 70-79 (2021). <https://doi.org:https://doi.org/10.1016/j.jechem.2020.06.065>



- 31 Zhu, S., Sheng, J., Chen, Y., Ni, J. & Li, Y. Carbon nanotubes for flexible batteries: recent progress and future perspective. *National Science Review* **8** (2020). <https://doi.org:10.1093/nsr/nwaa261>
- 32 Park, C. W. *et al.* Graphene collage on Ni-rich layered oxide cathodes for advanced lithium-ion batteries. *Nature Communications* **12**, 2145 (2021). <https://doi.org:10.1038/s41467-021-22403-w>
- 33 El-Kady, M. F., Shao, Y. & Kaner, R. B. Graphene for batteries, supercapacitors and beyond. *Nature Reviews Materials* **1**, 16033 (2016). <https://doi.org:10.1038/natrevmats.2016.33>
- 34 Chen, M., Guan, R. & Yang, S. Hybrids of Fullerenes and 2D Nanomaterials. *Advanced Science* **6**, 1800941 (2019). <https://doi.org:https://doi.org/10.1002/advs.201800941>
- 35 Desai, S. B. *et al.* MoS<sub>2</sub> transistors with 1-nanometer gate lengths. *Science* **354**, 99-102 (2016). <https://doi.org:doi:10.1126/science.aah4698>
- 36 Shahdeo, D., Chauhan, N., Majumdar, A., Ghosh, A. & Gandhi, S. Graphene-Based Field-Effect Transistor for Ultrasensitive Immunosensing of SARS-CoV-2 Spike S1 Antigen. *ACS Applied Bio Materials* **5**, 3563-3572 (2022). <https://doi.org:10.1021/acsabm.2c00503>
- 37 Bocharov, G. S. *et al.* Laser Strengthening of a Steel Surface with Fullerene Coating. *Doklady Physics* **63**, 489-492 (2018). <https://doi.org:10.1134/S1028335818120017>
- 38 Borges, D. J. A. *et al.* Stainless steel weld metal enhanced with carbon nanotubes. *Scientific Reports* **10**, 17977 (2020). <https://doi.org:10.1038/s41598-020-75136-z>
- 39 Bhattacharjee, S., Joshi, R., Chughtai, A. A. & Macintyre, C. R. Graphene Modified Multifunctional Personal Protective Clothing. *Advanced Materials Interfaces* **6**, 1900622 (2019). <https://doi.org:https://doi.org/10.1002/admi.201900622>
- 40 Chejanovsky, N. *et al.* Single-spin resonance in a van der Waals embedded paramagnetic defect. *Nature Materials* **20**, 1079-1084 (2021). <https://doi.org:10.1038/s41563-021-00979-4>
- 41 Kim, H. *et al.* Actively variable-spectrum optoelectronics with black phosphorus. *Nature* **596**, 232-237 (2021). <https://doi.org:10.1038/s41586-021-03701-1>
- 42 Wang, Y., Nie, Z. & Wang, F. Modulation of photocarrier relaxation dynamics in two-dimensional semiconductors. *Light: Science & Applications* **9**, 192 (2020). <https://doi.org:10.1038/s41377-020-00430-4>
- 43 Oliva, R. *et al.* Hidden spin-polarized bands in semiconducting 2H-MoTe<sub>2</sub>. *Materials Research Letters* **8**, 75-81 (2020). <https://doi.org:10.1080/21663831.2019.1702113>
- 44 Cho, S. *et al.* Phase patterning for ohmic homojunction contact in MoTe<sub>2</sub>. *Science* **349**, 625-628 (2015). <https://doi.org:doi:10.1126/science.aab3175>
- 45 Zheng, F. *et al.* Sub-Nanometer Electron Beam Phase Patterning in 2D Materials. *Advanced Science* **9**, 2200702 (2022). <https://doi.org:https://doi.org/10.1002/advs.202200702>
- 46 Cheng, P. K. *et al.* Nonlinear optical properties of two-dimensional palladium ditelluride (PdTe<sub>2</sub>) and its application as aerosol jet printed saturable absorbers for broadband ultrafast photonics. *Applied Materials Today* **26**, 101296 (2022). <https://doi.org:https://doi.org/10.1016/j.apmt.2021.101296>
- 47 Ho, T.-L. *et al.* Multi-Level Resistive Switching in SnSe/SrTiO<sub>3</sub> Heterostructure Based Memristor Device. *Nanomaterials* **12**, 2128 (2022).



- 48 Jiang, J. *et al.* Stable InSe transistors with high-field effect mobility for reliable nerve signal sensing. *npj 2D Materials and Applications* **3**, 29 (2019). <https://doi.org:10.1038/s41699-019-0110-x>
- 49 Chitara, B. & Ya'akovovitz, A. High-frequency electromechanical resonators based on thin GaTe. *Nanotechnology* **28**, 42LT02 (2017). <https://doi.org:10.1088/1361-6528/aa897d>
- 50 Sun, D. *et al.* Direct Visualization of Atomic Structure in Multivariate MOFs for Guiding Electrocatalysts Design. *Angewandte Chemie International Edition* **n/a** (2022). <https://doi.org:https://doi.org/10.1002/anie.202216008>
- 51 Liu, C.-K. *et al.* 2D Metal–Organic Framework Cu<sub>3</sub>(HHTT)<sub>2</sub> Films for Broadband Photodetectors from Ultraviolet to Mid-Infrared. *Advanced Materials* **34**, 2204140 (2022). <https://doi.org:https://doi.org/10.1002/adma.202204140>
- 52 Pang, S.-Y., Io, W.-F. & Hao, J. Facile Atomic-Level Tuning of Reactive Metal–Support Interactions in the Pt QDs@ HF-Free MXene Heterostructure for Accelerating pH-Universal Hydrogen Evolution Reaction. *Advanced Science* **8**, 2102207 (2021). <https://doi.org:https://doi.org/10.1002/advs.202102207>
- 53 Shao, Y. *et al.* Broadband Visible Nonlinear Absorption and Ultrafast Dynamics of the Ti<sub>3</sub>C<sub>2</sub> Nanosheet. *Nanomaterials* **10**, 2544 (2020).
- 54 Garvie, L. A., Craven, A. J. & Brydson, R. Use of electron-energy loss near-edge fine structure in the study of minerals. *American Mineralogist* **79**, 411–425 (1994).
- 55 Laffont, L. & Gibot, P. High resolution electron energy loss spectroscopy of manganese oxides: Application to Mn<sub>3</sub>O<sub>4</sub> nanoparticles. *Materials Characterization* **61**, 1268–1273 (2010). <https://doi.org:https://doi.org/10.1016/j.matchar.2010.09.001>
- 56 Ahn, C. C. *Transmission electron energy loss spectrometry in materials science and the EELS atlas*. (John Wiley & Sons, 2006).
- 57 Senga, R. *et al.* Position and momentum mapping of vibrations in graphene nanostructures. *Nature* **573**, 247–250 (2019). <https://doi.org:10.1038/s41586-019-1477-8>
- 58 Yang, X. *et al.* A review of *in situ* transmission electron microscopy study on the switching mechanism and packaging reliability in non-volatile memory. *Journal of Semiconductors* - **42**, - 013102 (2021). <https://doi.org:-10.1088/1674-4926/42/1/013102>
- 59 Li, S. *et al.* Review of recent progress on *in situ* TEM shear deformation: a retrospective and perspective view. *Journal of Materials Science* **57**, 12177–12201 (2022). <https://doi.org:10.1007/s10853-022-07331-4>
- 60 Lee, S. *et al.* Reversible cyclic deformation mechanism of gold nanowires by twinning–detwinning transition evidenced from *in situ* TEM. *Nature Communications* **5**, 3033 (2014). <https://doi.org:10.1038/ncomms4033>
- 61 Kondo, S., Mitsuma, T., Shibata, N. & Ikuhara, Y. Direct observation of individual dislocation interaction processes with grain boundaries. *Science Advances* **2**, e1501926 (2016). <https://doi.org:doi:10.1126/sciadv.1501926>
- 62 Kiener, D. & Minor, A. M. Source Truncation and Exhaustion: Insights from Quantitative *in situ* TEM Tensile Testing. *Nano Letters* **11**, 3816–3820 (2011). <https://doi.org:10.1021/nl201890s>
- 63 Guo, H. *et al.* Mechanics and Dynamics of the Strain-Induced M1–M2 Structural Phase Transition in Individual VO<sub>2</sub> Nanowires. *Nano Letters* **11**, 3207–3213 (2011). <https://doi.org:10.1021/nl201460v>



- 64 Momprou, F. & Legros, M. Quantitative grain growth and rotation probed by in-situ TEM straining and orientation mapping in small grained Al thin films. *Scripta Materialia* **99**, 5-8 (2015).  
<https://doi.org/10.1016/j.scriptamat.2014.11.004>
- 65 Feng, L., Hao, R., Lambros, J. & Dillon, S. J. The influence of dopants and complexion transitions on grain boundary fracture in alumina. *Acta Materialia* **142**, 121-130 (2018).  
<https://doi.org/10.1016/j.actamat.2017.09.002>
- 66 Samira, R., Vakahi, A., Eliasy, R., Sherman, D. & Lachman, N. Mechanical and Compositional Implications of Gallium Ion Milling on Epoxy Resin. *Polymers* **13**, 2640 (2021).
- 67 Vishnubhotla, S. B. *et al.* Quantitative measurement of contact area and electron transport across platinum nanocontacts for scanning probe microscopy and electrical nanodevices. *Nanotechnology* **30**, 045705 (2019).  
<https://doi.org/10.1088/1361-6528/aaebd6>
- 68 Zhu, Q. *et al.* Metallic nanocrystals with low angle grain boundary for controllable plastic reversibility. *Nature Communications* **11**, 3100 (2020).  
<https://doi.org/10.1038/s41467-020-16869-3>
- 69 Zhao, J., Huang, J.-Q., Wei, F. & Zhu, J. Mass Transportation Mechanism in Electric-Biased Carbon Nanotubes. *Nano Letters* **10**, 4309-4315 (2010).  
<https://doi.org/10.1021/nl1008713>
- 70 Liu, X. H. & Huang, J. Y. In situ TEM electrochemistry of anode materials in lithium ion batteries. *Energy & Environmental Science* **4**, 3844-3860 (2011).  
<https://doi.org/10.1039/C1EE01918J>
- 71 Clark, N. *et al.* Tracking single adatoms in liquid in a transmission electron microscope. *Nature* **609**, 942-947 (2022). <https://doi.org/10.1038/s41586-022-05130-0>
- 72 Yuk, J. M. *et al.* High-Resolution EM of Colloidal Nanocrystal Growth Using Graphene Liquid Cells. *Science* **336**, 61-64 (2012).  
<https://doi.org/10.1126/science.1217654>
- 73 Zheng, Q. *et al.* Direct visualization of anionic electrons in an electride reveals inhomogeneities. *Science Advances* **7**, eabe6819 (2021).  
<https://doi.org/10.1126/sciadv.abe6819>
- 74 Dye, J. L. Electrides: Ionic Salts with Electrons as the Anions. *Science* **247**, 663-668 (1990). <https://doi.org/10.1126/science.247.4943.663>
- 75 Jianghao, W., Guangshe, L. & Liping, L. in *Two-dimensional Materials* (ed Nayak Pramoda Kumar) Ch. 1 (IntechOpen, 2016).
- 76 Zheng, F., Wong, L., Zhao, J. & Ly, T. H. in *21st Century Nanoscience—A Handbook* 6-1-6-25 (CRC Press, 2020).
- 77 Xing, T. *et al.* Gas Protection of Two-Dimensional Nanomaterials from High-Energy Impacts. *Scientific Reports* **6**, 35532 (2016).  
<https://doi.org/10.1038/srep35532>
- 78 Nicolosi, V., Chhowalla, M., Kanatzidis, M. G., Strano, M. S. & Coleman, J. N. Liquid Exfoliation of Layered Materials. *Science* **340**, 1226419 (2013).  
<https://doi.org/10.1126/science.1226419>
- 79 Huo, C., Yan, Z., Song, X. & Zeng, H. 2D materials via liquid exfoliation: a review on fabrication and applications. *Science Bulletin* **60**, 1994-2008 (2015).  
<https://doi.org/10.1007/s11434-015-0936-3>





- 80 Zhou, J. *et al.* A library of atomically thin metal chalcogenides. *Nature* **556**, 355-359 (2018). <https://doi.org/10.1038/s41586-018-0008-3>
- 81 Gao, X. *et al.* Integrated wafer-scale ultra-flat graphene by gradient surface energy modulation. *Nature Communications* **13**, 5410 (2022). <https://doi.org/10.1038/s41467-022-33135-w>
- 82 Li, J. *et al.* Wafer-scale single-crystal monolayer graphene grown on sapphire substrate. *Nature Materials* **21**, 740-747 (2022). <https://doi.org/10.1038/s41563-021-01174-1>
- 83 Yang, P. *et al.* Batch production of 6-inch uniform monolayer molybdenum disulfide catalyzed by sodium in glass. *Nature Communications* **9**, 979 (2018). <https://doi.org/10.1038/s41467-018-03388-5>
- 84 Pacuski, W. *et al.* Narrow Excitonic Lines and Large-Scale Homogeneity of Transition-Metal Dichalcogenide Monolayers Grown by Molecular Beam Epitaxy on Hexagonal Boron Nitride. *Nano Letters* **20**, 3058-3066 (2020). <https://doi.org/10.1021/acs.nanolett.9b04998>
- 85 He, Q. *et al.* Molecular Beam Epitaxy Scalable Growth of Wafer-Scale Continuous Semiconducting Monolayer MoTe<sub>2</sub> on Inert Amorphous Dielectrics. *Advanced Materials* **31**, 1901578 (2019). [https://doi.org:https://doi.org/10.1002/adma.201901578](https://doi.org/https://doi.org/10.1002/adma.201901578)
- 86 Zhang, Y. *et al.* Recent progress in CVD growth of 2D transition metal dichalcogenides and related heterostructures. *Advanced materials* **31**, 1901694 (2019).
- 87 Li, B. *et al.* Solid–Vapor Reaction Growth of Transition-Metal Dichalcogenide Monolayers. *Angewandte Chemie International Edition* **55**, 10656-10661 (2016). <https://doi.org:https://doi.org/10.1002/anie.201604445>
- 88 Pondick, J. V., Woods, J. M., Xing, J., Zhou, Y. & Cha, J. J. Stepwise Sulfurization from MoO<sub>3</sub> to MoS<sub>2</sub> via Chemical Vapor Deposition. *ACS Applied Nano Materials* **1**, 5655-5661 (2018). <https://doi.org/10.1021/acsanm.8b01266>
- 89 Zhu, D. *et al.* Capture the growth kinetics of CVD growth of two-dimensional MoS<sub>2</sub>. *npj 2D Materials and Applications* **1**, 1-8 (2017).
- 90 Zhou, D. *et al.* Unveiling the Growth Mechanism of MoS<sub>2</sub> with Chemical Vapor Deposition: From Two-Dimensional Planar Nucleation to Self-Seeding Nucleation. *Crystal Growth & Design* **18**, 1012-1019 (2018). <https://doi.org/10.1021/acs.cgd.7b01486>
- 91 Xue, H. *et al.* High-temperature in situ investigation of chemical vapor deposition to reveal growth mechanisms of monolayer molybdenum disulfide. *ACS Applied Electronic Materials* **2**, 1925-1933 (2020).
- 92 Wei, T.-R. *et al.* Exceptional plasticity in the bulk single-crystalline van der Waals semiconductor InSe. *Science* **369**, 542-545 (2020). <https://doi.org:doi:10.1126/science.aba9778>
- 93 Rice, J. R. & Thomson, R. Ductile versus brittle behaviour of crystals. *The Philosophical Magazine: A Journal of Theoretical Experimental and Applied Physics* **29**, 73-97 (1974). <https://doi.org/10.1080/14786437408213555>
- 94 Rudenko, A. N., Katsnelson, M. I. & Gornostyrev, Y. N. Dislocation structure and mobility in the layered semiconductor InSe: a first-principles study. *2D Materials* **8**, 045028 (2021). <https://doi.org/10.1088/2053-1583/ac207b>
- 95 Rice, J. R. Dislocation nucleation from a crack tip: An analysis based on the Peierls concept. *Journal of the Mechanics and Physics of Solids* **40**, 239-271 (1992). [https://doi.org:https://doi.org/10.1016/S0022-5096\(05\)80012-2](https://doi.org:https://doi.org/10.1016/S0022-5096(05)80012-2)



- 96 Senkov, O. N. & Miracle, D. B. Generalization of intrinsic ductile-to-brittle criteria by Pugh and Pettifor for materials with a cubic crystal structure. *Scientific Reports* **11**, 4531 (2021). <https://doi.org/10.1038/s41598-021-83953-z>
- 97 Pugh, S. F. XCII. Relations between the elastic moduli and the plastic properties of polycrystalline pure metals. *The London, Edinburgh, and Dublin Philosophical Magazine and Journal of Science* **45**, 823-843 (1954). <https://doi.org/10.1080/14786440808520496>
- 98 Pettifor, D. G. *et al.* Bonding and structure of intermetallics: a new bond order potential. *Philosophical Transactions of the Royal Society of London. Series A: Physical and Engineering Sciences* **334**, 439-449 (1991). <https://doi.org/doi:10.1098/rsta.1991.0024>
- 99 Pettifor, D. G. Theoretical predictions of structure and related properties of intermetallics. *Materials Science and Technology* **8**, 345-349 (1992). <https://doi.org/10.1179/mst.1992.8.4.345>
- 100 Pettifor, D. G. New many-body potential for the bond order. *Physical Review Letters* **63**, 2480-2483 (1989). <https://doi.org/10.1103/PhysRevLett.63.2480>
- 101 Inc., M. Large scale indium selenide crystal, <<http://www.mukenano.com/index.php?m=&c=Show&a=index&cid=345&id=417>> (2022).
- 102 Inc., D. S. Indium Selenide (InSe), <<https://www.2dsemiconductors.com/indium-selenide-inse/#description>> (2022).
- 103 de Graaf, S., Momand, J., Mitterbauer, C., Lazar, S. & Kooi, B. J. Resolving hydrogen atoms at metal-metal hydride interfaces. *Science Advances* **6**, eaay4312 (2020). <https://doi.org/doi:10.1126/sciadv.aay4312>
- 104 Ishikawa, R. *et al.* Direct imaging of hydrogen-atom columns in a crystal by annular bright-field electron microscopy. *Nature Materials* **10**, 278-281 (2011). <https://doi.org/10.1038/nmat2957>
- 105 Li, H.-B. *et al.* Electric Field-Controlled Multistep Proton Evolution in  $H_xSrCoO_{2.5}$  with Formation of H-H Dimer. *Advanced Science* **6**, 1901432 (2019). <https://doi.org/https://doi.org/10.1002/advs.201901432>
- 106 Zhang, J. *et al.* Real-Space Identification of Intermolecular Bonding with Atomic Force Microscopy. *Science* **342**, 611-614 (2013). <https://doi.org/doi:10.1126/science.1242603>
- 107 Kawai, S. *et al.* Direct quantitative measurement of the C=O...H-C bond by atomic force microscopy. *Science Advances* **3**, e1603258 (2017). <https://doi.org/doi:10.1126/sciadv.1603258>
- 108 Gross, L., Mohn, F., Moll, N., Liljeroth, P. & Meyer, G. The Chemical Structure of a Molecule Resolved by Atomic Force Microscopy. *Science* **325**, 1110-1114 (2009). <https://doi.org/doi:10.1126/science.1176210>
- 109 Shen, B. *et al.* A single-molecule van der Waals compass. *Nature* **592**, 541-544 (2021). <https://doi.org/10.1038/s41586-021-03429-y>
- 110 Shen, B., Chen, X., Shen, K., Xiong, H. & Wei, F. Imaging the node-linker coordination in the bulk and local structures of metal-organic frameworks. *Nature Communications* **11**, 2692 (2020). <https://doi.org/10.1038/s41467-020-16531-y>
- 111 Li, X. *et al.* Direct Imaging of Tunable Crystal Surface Structures of MOF MIL-101 Using High-Resolution Electron Microscopy. *Journal of the American Chemical Society* **141**, 12021-12028 (2019). <https://doi.org/10.1021/jacs.9b04896>





- 112 Furukawa, H., Cordova, K. E., O’Keeffe, M. & Yaghi, O. M. The Chemistry and Applications of Metal-Organic Frameworks. *Science* **341**, 1230444 (2013). <https://doi.org/doi:10.1126/science.1230444>
- 113 The Nobel Foundation. *J.J. Thomson – Biographical*, <<https://www.nobelprize.org/prizes/physics/1906/thomson/biographical/>> (1906).
- 114 The Nobel Foundation. *Louis de Broglie – Biographical*, <<https://www.nobelprize.org/prizes/physics/1929/broglie/biographical/>> (1929).
- 115 Hessisches Landesamt für geschichtliche Landeskunde. *Busch, Hans Walter Hugo*, <<https://www.lagis-hessen.de/pnd/117692670>> (2021).
- 116 The Nobel Foundation. *Clinton Davisson – Biographical*, <<https://www.nobelprize.org/prizes/physics/1937/davisson/biographical/>> (1937).
- 117 The Nobel Foundation. *George Paget Thomson – Biographical*, <<https://www.nobelprize.org/prizes/physics/1937/thomson/biographical/>> (1937).
- 118 The Nobel Foundation. *Ernst Ruska – Biographical*, <<https://www.nobelprize.org/prizes/physics/1986/ruska/biographical/>> (1986).
- 119 Goodreads, I. *Max Knoll*, <[https://www.goodreads.com/author/show/4289817.Max\\_Knoll](https://www.goodreads.com/author/show/4289817.Max_Knoll)> (2022).
- 120 Microscopy Society of America. *Otto Scherzer: The father of aberration correction*, <<https://www.microscopy.org/images/posters/Scherzer.pdf>> (2022).
- 121 VON ARDENNE GMBH. *MANFRED VON ARDENNE (1907-1997)*, <<https://www.vonardenne.biz/en/company/mva/>> (2022).
- 122 The James Hillier Foundation. *Biography*, <<https://www.jameshillierfoundation.com/about-james-hillier/biography/>> (2007).
- 123 Teng, L. C. & Hildebrand, R. H. Albert Victor Crewe. *Physics Today* **63**, 66-68 (2010). <https://doi.org/10.1063/1.3502556>
- 124 The Nobel Foundation. *Willard S. Boyle – Biographical*, <<https://www.nobelprize.org/prizes/physics/2009/boyle/biographical/>> (2009).
- 125 The Nobel Foundation. *George E. Smith – Biographical*, <<https://www.nobelprize.org/prizes/physics/2009/smith/biographical/>> (2009).
- 126 Crick, F. & Anderson, P. W. *What Mad Pursuit: A personal view of scientific discovery*. (Pumyang, 1991).
- 127 Thomson, J. J. XL. Cathode rays. *The London, Edinburgh, and Dublin Philosophical Magazine and Journal of Science* **44**, 293-316 (1897).
- 128 de Broglie, L. in *Annales de Physique*. 22-128.
- 129 Davisson, C. & Germer, L. H. The Scattering of Electrons by a Single Crystal of Nickel. *Nature* **119**, 558-560 (1927). <https://doi.org/10.1038/119558a0>
- 130 Busch, H. Berechnung der Bahn von Kathodenstrahlen im axialsymmetrischen elektromagnetischen Felde. *Annalen der Physik* **386**, 974-993 (1926). [https://doi.org:https://doi.org/10.1002/andp.19263862507](https://doi.org/https://doi.org/10.1002/andp.19263862507)
- 131 Ruska, E. & Knoll, M. Die magnetische Sammelspule für schnelle Elektronenstrahlen. *The magnetic concentrating coil for fast electron beams.* *Z. techn. Physik* **12**, 389-400 (1931).
- 132 Scherzer, O. Über einige Fehler von Elektronenlinsen. *Zeitschrift für Physik* **101**, 593-603 (1936). <https://doi.org/10.1007/BF01349606>



- 133 Scherzer, O. Sphärische und chromatische korrektur von elektronen-linsen. *Optik* **2**, 114-132 (1947).
- 134 Haider, M. *et al.* Electron microscopy image enhanced. *Nature* **392**, 768-769 (1998). <https://doi.org/10.1038/33823>
- 135 von Ardenne, M. Improvements in electron microscopes. *British patent* (1937).
- 136 Hillier, J. & Baker, R. F. Microanalysis by Means of Electrons. *Journal of Applied Physics* **15**, 663-675 (1944). <https://doi.org/10.1063/1.1707491>
- 137 Crewe, A., Eggenberger, D., Wall, J. & Welter, L. Electron gun using a field emission source. *Review of Scientific Instruments* **39**, 576-583 (1968).
- 138 Crewe, A. V., Wall, J. & Welter, L. M. A High-Resolution Scanning Transmission Electron Microscope. *Journal of Applied Physics* **39**, 5861-5868 (1968). <https://doi.org/10.1063/1.1656079>
- 139 Boyle, W. S. & Smith, G. E. Charge coupled semiconductor devices. *The Bell System Technical Journal* **49**, 587-593 (1970). <https://doi.org/10.1002/j.1538-7305.1970.tb01790.x>
- 140 Tate, M. W. *et al.* High Dynamic Range Pixel Array Detector for Scanning Transmission Electron Microscopy. *Microscopy and Microanalysis* **22**, 237-249 (2016). <https://doi.org/10.1017/S1431927615015664>
- 141 Maiden, A. M., Humphry, M. J., Zhang, F. & Rodenburg, J. M. Superresolution imaging via ptychography. *J. Opt. Soc. Am. A* **28**, 604-612 (2011). <https://doi.org/10.1364/JOSAA.28.000604>
- 142 Allen, L. J., D'Alfonso, A. J. & Findlay, S. D. Modelling the inelastic scattering of fast electrons. *Ultramicroscopy* **151**, 11-22 (2015). [https://doi.org:https://doi.org/10.1016/j.ultramic.2014.10.011](https://doi.org/https://doi.org/10.1016/j.ultramic.2014.10.011)
- 143 Chen, Z. *et al.* Electron ptychography achieves atomic-resolution limits set by lattice vibrations. *Science* **372**, 826-831 (2021). [https://doi.org:doi:10.1126/science.abg2533](https://doi.org/doi:10.1126/science.abg2533)
- 144 Abbe, E. Die Beziehung zwischen Apertur und Vergrößerung beim Mikroskop (The Relation of Aperture and Power in the Microscope). *Journal of the Royal Society (2) II*, 300-309 (1883).
- 145 Muller, D. A. in *2021 Lecture videos* (PARADIM, PARADIM, 2021).
- 146 Rayleigh. XXXI. Investigations in optics, with special reference to the spectroscopy. *The London, Edinburgh, and Dublin Philosophical Magazine and Journal of Science* **8**, 261-274 (1879). <https://doi.org/10.1080/14786447908639684>
- 147 Carter, C. B. & Williams, D. B. *Transmission electron microscopy: Diffraction, imaging, and spectrometry*. (Springer, 2016).
- 148 Bragg, W. H. & Bragg, W. L. The reflection of X-rays by crystals. *Proceedings of the Royal Society of London. Series A, Containing Papers of a Mathematical and Physical Character* **88**, 428-438 (1913). <https://doi.org/doi:10.1098/rspa.1913.0040>
- 149 Cowley, J. M. *Diffraction physics*. (Elsevier, 1995).
- 150 Scherzer, O. The Theoretical Resolution Limit of the Electron Microscope. *Journal of Applied Physics* **20**, 20-29 (1949). <https://doi.org/10.1063/1.1698233>
- 151 Findlay, S. D. *et al.* Annular Bright-Field Scanning Transmission Electron Microscopy: Direct and Robust Atomic-Resolution Imaging of Light Elements in Crystalline Materials. *Microscopy Today* **25**, 36-41 (2017). <https://doi.org/10.1017/S1551929517001006>



- 152 Pennycook, S. J. & Nellist, P. D. *Scanning transmission electron microscopy: imaging and analysis*. (Springer Science & Business Media, 2011).
- 153 Liao, Y. Practical electron microscopy and database. *An Online Book* (2006).
- 154 Weyland, M. & Muller, D. A. Tuning the convergence angle for optimum STEM performance. *arXiv preprint arXiv:2008.12870* (2020).
- 155 Voyles, P. M., Muller, D. A. & Kirkland, E. J. Depth-Dependent Imaging of Individual Dopant Atoms in Silicon. *Microscopy and Microanalysis* **10**, 291-300 (2004). <https://doi.org:10.1017/S1431927604040012>
- 156 Hovden, R., Xin, H. L. & Muller, D. A. Channeling of a subangstrom electron beam in a crystal mapped to two-dimensional molecular orbitals. *Physical Review B* **86**, 195415 (2012). <https://doi.org:10.1103/PhysRevB.86.195415>
- 157 Lazić, I., Bosch, E. G. T. & Lazar, S. Phase contrast STEM for thin samples: Integrated differential phase contrast. *Ultramicroscopy* **160**, 265-280 (2016). <https://doi.org:https://doi.org/10.1016/j.ultramic.2015.10.011>
- 158 Lazić, I. & Bosch, E. G. T. in *Advances in Imaging and Electron Physics* Vol. 199 (ed Peter W. Hawkes) 75-184 (Elsevier, 2017).
- 159 Song, D. *et al.* Visualization of Dopant Oxygen Atoms in a  $\text{Bi}_2\text{Sr}_2\text{CaCu}_2\text{O}_{8+\delta}$  Superconductor. *Advanced Functional Materials* **29**, 1903843 (2019). <https://doi.org:https://doi.org/10.1002/adfm.201903843>
- 160 Bak, J., Bin Bae, H. & Chung, S.-Y. Atomic-scale perturbation of oxygen octahedra via surface ion exchange in perovskite nickelates boosts water oxidation. *Nature Communications* **10**, 2713 (2019). <https://doi.org:10.1038/s41467-019-10838-1>
- 161 Li, X. *et al.* Imaging biological samples by integrated differential phase contrast (iDPC) STEM technique. *Journal of Structural Biology* **214**, 107837 (2022). <https://doi.org:https://doi.org/10.1016/j.jsb.2022.107837>
- 162 Grant, I. S. & Phillips, W. R. *Electromagnetism*. (John Wiley & Sons, 2013).
- 163 Jenkins, R. *Quantitative X-ray spectrometry*. (CRC Press, 1995).
- 164 Du, K. *et al.* Manipulating topological transformations of polar structures through real-time observation of the dynamic polarization evolution. *Nature Communications* **10**, 4864 (2019). <https://doi.org:10.1038/s41467-019-12864-5>
- 165 Allen, L. J., D'Alfonso, A. J., Freitag, B. & Klenov, D. O. Chemical mapping at atomic resolution using energy-dispersive x-ray spectroscopy. *MRS Bulletin* **37**, 47-52 (2012). <https://doi.org:10.1557/mrs.2011.331>
- 166 MacArthur, K. E. *et al.* Optimizing Experimental Conditions for Accurate Quantitative Energy-Dispersive X-ray Analysis of Interfaces at the Atomic Scale. *Microscopy and Microanalysis* **27**, 528-542 (2021). <https://doi.org:10.1017/S1431927621000246>
- 167 Egerton, R. F. *Electron energy-loss spectroscopy in the electron microscope*. (Springer Science & Business Media, 2011).
- 168 Messiah, A. *Quantum mechanics*. (Courier Corporation, 2014).
- 169 Jorcin, J.-B., Aragon, E., Merlatti, C. & Pébère, N. Delaminated areas beneath organic coating: A local electrochemical impedance approach. *Corrosion Science* **48**, 1779-1790 (2006). <https://doi.org:https://doi.org/10.1016/j.corsci.2005.05.031>
- 170 dos Santos, F. J., dos Santos Dias, M., Guimarães, F. S. M., Bouaziz, J. & Lounis, S. Spin-resolved inelastic electron scattering by spin waves in noncollinear magnets. *Physical Review B* **97**, 024431 (2018). <https://doi.org:10.1103/PhysRevB.97.024431>



- 171 Sarikaya, M., Qian, M. & Stern, E. A. EXELFS revisited. *Micron* **27**, 449-466 (1996). [https://doi.org:https://doi.org/10.1016/S0968-4328\(96\)00044-3](https://doi.org/10.1016/S0968-4328(96)00044-3)
- 172 Suk, J. W. *et al.* Transfer of CVD-Grown Monolayer Graphene onto Arbitrary Substrates. *ACS Nano* **5**, 6916-6924 (2011). [https://doi.org:10.1021/nn201207c](https://doi.org/10.1021/nn201207c)
- 173 Caldwell, J. D. *et al.* Technique for the Dry Transfer of Epitaxial Graphene onto Arbitrary Substrates. *ACS Nano* **4**, 1108-1114 (2010). [https://doi.org:10.1021/nn901585p](https://doi.org/10.1021/nn901585p)
- 174 Giannuzzi, L. A. *Introduction to focused ion beams: instrumentation, theory, techniques and practice.* (Springer Science & Business Media, 2004).
- 175 Guise, O. L., Ahner, J. W., Jung, M.-C., Goughnour, P. C. & Yates, J. T. Reproducible Electrochemical Etching of Tungsten Probe Tips. *Nano Letters* **2**, 191-193 (2002). [https://doi.org:10.1021/nl010094q](https://doi.org/10.1021/nl010094q)
- 176 Liu, E. *et al.* Integrated digital inverters based on two-dimensional anisotropic ReS<sub>2</sub> field-effect transistors. *Nature communications* **6**, 1-7 (2015).
- 177 Cui, F. *et al.* Epitaxial growth of large-area and highly crystalline anisotropic ReSe<sub>2</sub> atomic layer. *Nano Research* **10**, 2732-2742 (2017).
- 178 Li, J. *et al.* Direct growth of vertically aligned ReSe<sub>2</sub> nanosheets on conductive electrode for electro-catalytic hydrogen production. *Journal of colloid and interface science* **553**, 699-704 (2019).
- 179 Xing, L. *et al.* Highly crystalline ReSe<sub>2</sub> atomic layers synthesized by chemical vapor transport. *InfoMat* **1**, 552-558 (2019).
- 180 Shi, Y., Li, H. & Li, L.-J. Recent advances in controlled synthesis of two-dimensional transition metal dichalcogenides via vapour deposition techniques. *Chemical Society Reviews* **44**, 2744-2756 (2015).
- 181 Jiang, S. *et al.* Salt-assisted growth and ultrafast photocarrier dynamics of large-sized monolayer ReSe<sub>2</sub>. *Nano Research* **13**, 667-675 (2020).
- 182 Shi, J. *et al.* Controllable growth and transfer of monolayer MoS<sub>2</sub> on Au foils and its potential application in hydrogen evolution reaction. *ACS nano* **8**, 10196-10204 (2014).
- 183 Etzkorn, J. *et al.* Metal–Organic Chemical Vapor Deposition Synthesis of Hollow Inorganic–Fullerene-Type MoS<sub>2</sub> and MoSe<sub>2</sub> Nanoparticles. *Advanced materials* **17**, 2372-2375 (2005).
- 184 Xie, C. *et al.* Space-confined growth of monolayer ReSe<sub>2</sub> under a graphene layer on Au foils. *Nano Research* **12**, 149-157 (2019).
- 185 Chareev, D. A. *et al.* Growth of transition-metal dichalcogenides by solvent evaporation technique. *Crystal Growth & Design* **20**, 6930-6938 (2020).
- 186 Huang, L. *et al.* Redox photochemistry on van der Waals surfaces for reversible doping in 2D materials. *Advanced Functional Materials* **31**, 2009166 (2021).
- 187 Huang, L. *et al.* Catalyzed kinetic growth in two-dimensional MoS<sub>2</sub>. *Journal of the American Chemical Society* **142**, 13130-13135 (2020).
- 188 An, G. H., Yun, S. J., Lee, Y. H. & Lee, H. S. Growth Mechanism of Alternating Defect Domains in Hexagonal WS<sub>2</sub> via Inhomogeneous W-Precursor Accumulation. *Small* **16**, 2003326 (2020).
- 189 Hong, S. *et al.* Computational synthesis of MoS<sub>2</sub> layers by reactive molecular dynamics simulations: initial sulfidation of MoO<sub>3</sub> surfaces. *Nano letters* **17**, 4866-4872 (2017).
- 190 Ji, Q., Zhang, Y., Zhang, Y. & Liu, Z. Chemical vapour deposition of group-VIB metal dichalcogenide monolayers: engineered substrates from amorphous to single crystalline. *Chemical Society Reviews* **44**, 2587-2602 (2015).





- 191 Shao, P., Ding, L.-P. & Ding, F. Mechanism of MoS<sub>2</sub> Growth on a Au (111) Surface: An Ab Initio Molecular Dynamics Study. *Chemistry of Materials* **33**, 3241-3248 (2021).
- 192 Kim, S. Y., Kwak, J., Ciobanu, C. V. & Kwon, S. Y. Recent developments in controlled vapor-phase growth of 2D group 6 transition metal dichalcogenides. *Advanced Materials* **31**, 1804939 (2019).
- 193 Barja, S. *et al.* Identifying substitutional oxygen as a prolific point defect in monolayer transition metal dichalcogenides. *Nature communications* **10**, 1-8 (2019).
- 194 Fan, X. *et al.* Direct observation of grain boundaries in graphene through vapor hydrofluoric acid (VHF) exposure. *Science advances* **4**, eaar5170 (2018).
- 195 Kim, H. *et al.* Role of alkali metal promoter in enhancing lateral growth of monolayer transition metal dichalcogenides. *Nanotechnology* **28**, 36LT01 (2017).
- 196 Liu, K.-K. *et al.* Growth of large-area and highly crystalline MoS<sub>2</sub> thin layers on insulating substrates. *Nano letters* **12**, 1538-1544 (2012).
- 197 Yue, R. *et al.* Nucleation and growth of WSe<sub>2</sub>: enabling large grain transition metal dichalcogenides. *2D Materials* **4**, 045019 (2017).
- 198 Cain, J. D., Shi, F., Wu, J. & Dravid, V. P. Growth mechanism of transition metal dichalcogenide monolayers: the role of self-seeding fullerene nuclei. *ACS nano* **10**, 5440-5445 (2016).
- 199 Murugan, P., Kumar, V., Kawazoe, Y. & Ota, N. Atomic structures and magnetism in small MoS<sub>2</sub> and WS<sub>2</sub> clusters. *Physical Review A* **71**, 063203 (2005).
- 200 Zheng, Z., Long, J. R. & Holm, R. A basis set of Re<sub>6</sub>Se<sub>8</sub> cluster building blocks and demonstration of their linking capability: directed synthesis of an Re<sub>12</sub>Se<sub>16</sub> dicluster. *Journal of the American Chemical Society* **119**, 2163-2171 (1997).
- 201 Gray, T. G., Rudzinski, C. M., Nocera, D. G. & Holm, R. Highly emissive hexanuclear rhenium (III) clusters containing the cubic cores [Re<sub>6</sub>S<sub>8</sub>]<sup>2+</sup> and [Re<sub>6</sub>Se<sub>8</sub>]<sup>2+</sup>. *Inorganic Chemistry* **38**, 5932-5933 (1999).
- 202 Kresse, G. & Furthmüller, J. Efficient iterative schemes for ab initio total-energy calculations using a plane-wave basis set. *Physical review B* **54**, 11169 (1996).
- 203 Kresse, G. & Furthmüller, J. Efficiency of ab-initio total energy calculations for metals and semiconductors using a plane-wave basis set. *Computational materials science* **6**, 15-50 (1996).
- 204 Blöchl, P. E. Projector augmented-wave method. *Physical review B* **50**, 17953 (1994).
- 205 Perdew, J. P., Burke, K. & Ernzerhof, M. Generalized gradient approximation made simple. *Physical review letters* **77**, 3865 (1996).
- 206 Perdew, J. P., Ernzerhof, M. & Burke, K. Rationale for mixing exact exchange with density functional approximations. *The Journal of chemical physics* **105**, 9982-9985 (1996).
- 207 Grimme, S., Antony, J., Ehrlich, S. & Krieg, H. A consistent and accurate ab initio parametrization of density functional dispersion correction (DFT-D) for the 94 elements H-Pu. *The Journal of Chemical Physics* **132**, 154104 (2010). <https://doi.org:10.1063/1.3382344>
- 208 Alcock, N. & Kjekshus, A. The crystal structure of ReSe<sub>2</sub>. *Acta Chem. Scand* **19**, 19-0079 (1965).
- 209 Speziali, N. *et al.* Single crystal growth, structure and characterization of the octahedral cluster compound Re<sub>6</sub>Se<sub>8</sub>Br<sub>2</sub>. *Materials research bulletin* **23**, 1597-1604 (1988).



- 210 Zheng, F. *et al.* The Mobile and Pinned Grain Boundaries in 2D Monoclinic Rhenium Disulfide. *Advanced Science* **7**, 2001742 (2020).
- 211 Yang, S. *et al.* Tuning the optical, magnetic, and electrical properties of ReSe<sub>2</sub> by nanoscale strain engineering. *Nano letters* **15**, 1660-1666 (2015).
- 212 Kühn, F. E. & Herrmann, W. A. Rhenium-oxo and rhenium-peroxo complexes in catalytic oxidations. *Metal-Oxo and Metal-Peroxo Species in Catalytic Oxidations*, 213-236 (2000).
- 213 Zheng, Z.-P., Selby, H. D. & Roland, B. K. The first hexaqua-'complex of the [Re<sub>6</sub>Se<sub>8</sub>]<sup>2+</sup> cluster core, [Re<sub>6</sub>Se<sub>8</sub> (OH)<sub>2</sub> (H<sub>2</sub>O)<sub>4</sub>] · 12H<sub>2</sub>O. *Acta Crystallographica Section E: Structure Reports Online* **57**, i77-i79 (2001).
- 214 Gabriel, J.-C. P., Boubekur, K., Uriel, S. & Batail, P. Chemistry of hexanuclear rhenium chalcogenide clusters. *Chemical Reviews* **101**, 2037-2066 (2001).
- 215 Li, X. *et al.* Controlled growth of large-area anisotropic ReS<sub>2</sub> atomic layer and its photodetector application. *Nanoscale* **8**, 18956-18962 (2016).
- 216 Petroski, H. M. C. The Pencil : a History of Design and Circumstance. (2011).
- 217 Kim, Y., Sung, A., Seo, Y., Hwang, S. & Kim, H. Measurement of hardness and friction properties of pencil leads for quantification of pencil hardness test. *Advances in Applied Ceramics* **115**, 443-448 (2016).  
<https://doi.org/10.1080/17436753.2016.1186364>
- 218 Heissenbüttel, M.-C., Maruhn, P., Deilmann, T., Krüger, P. & Rohlfing, M. Nature of the excited states of layered systems and molecular excimers: Exciplex states and their dependence on structure. *Physical Review B* **99**, 035425 (2019).  
<https://doi.org/10.1103/PhysRevB.99.035425>
- 219 Ermolaev, G. A. *et al.* Giant optical anisotropy in transition metal dichalcogenides for next-generation photonics. *Nature Communications* **12**, 854 (2021).  
<https://doi.org/10.1038/s41467-021-21139-x>
- 220 Wang, Q. H., Kalantar-Zadeh, K., Kis, A., Coleman, J. N. & Strano, M. S. Electronics and optoelectronics of two-dimensional transition metal dichalcogenides. *Nature Nanotechnology* **7**, 699-712 (2012).  
<https://doi.org/10.1038/nnano.2012.193>
- 221 Wang, Y., Szökölóvá, K., Nasir, M. Z. M., Sofer, Z. & Pumera, M. Electrochemistry of Layered Semiconducting AIIIBVI Chalcogenides: Indium Monochalcogenides (InS, InSe, InTe). *ChemCatChem* **11**, 2634-2642 (2019).  
[https://doi.org:https://doi.org/10.1002/cctc.201900449](https://doi.org/https://doi.org/10.1002/cctc.201900449)
- 222 Luxa, J., Wang, Y., Sofer, Z. & Pumera, M. Layered Post-Transition-Metal Dichalcogenides (X–M–M–X) and Their Properties. *Chemistry – A European Journal* **22**, 18810-18816 (2016).  
<https://doi.org:https://doi.org/10.1002/chem.201604168>
- 223 Late, D. J. *et al.* GaS and GaSe Ultrathin Layer Transistors. *Advanced Materials* **24**, 3549-3554 (2012). <https://doi.org:https://doi.org/10.1002/adma.201201361>
- 224 Feng, W., Zheng, W., Cao, W. & Hu, P. Back Gated Multilayer InSe Transistors with Enhanced Carrier Mobilities via the Suppression of Carrier Scattering from a Dielectric Interface. *Advanced Materials* **26**, 6587-6593 (2014).  
<https://doi.org:https://doi.org/10.1002/adma.201402427>
- 225 Wu, L. *et al.* InSe/hBN/graphite heterostructure for high-performance 2D electronics and flexible electronics. *Nano Research* **13**, 1127-1132 (2020).  
<https://doi.org/10.1007/s12274-020-2757-1>





- 226 Yoon, Y., Ganapathi, K. & Salahuddin, S. How Good Can Monolayer MoS<sub>2</sub> Transistors Be? *Nano Letters* **11**, 3768-3773 (2011). <https://doi.org:10.1021/nl2018178>
- 227 Radisavljevic, B. & Kis, A. Mobility engineering and a metal–insulator transition in monolayer MoS<sub>2</sub>. *Nature Materials* **12**, 815-820 (2013). <https://doi.org:10.1038/nmat3687>
- 228 Zhong, F. *et al.* Substitutionally Doped MoSe<sub>2</sub> for High-Performance Electronics and Optoelectronics. *Small* **17**, 2102855 (2021). <https://doi.org:https://doi.org/10.1002/sml.202102855>
- 229 Wu, E. *et al.* Dynamically controllable polarity modulation of MoTe<sub>2</sub> field-effect transistors through ultraviolet light and electrostatic activation. *Science Advances* **5**, eaav3430 (2019). <https://doi.org:doi:10.1126/sciadv.aav3430>
- 230 Fang, H. *et al.* High-Performance Single Layered WSe<sub>2</sub> p-FETs with Chemically Doped Contacts. *Nano Letters* **12**, 3788-3792 (2012). <https://doi.org:10.1021/nl301702r>
- 231 Iqbal, M. W. *et al.* High-mobility and air-stable single-layer WS<sub>2</sub> field-effect transistors sandwiched between chemical vapor deposition-grown hexagonal BN films. *Scientific Reports* **5**, 10699 (2015). <https://doi.org:10.1038/srep10699>
- 232 Wang, Y. *et al.* Electron mobility in monolayer WS<sub>2</sub> encapsulated in hexagonal boron-nitride. *Applied Physics Letters* **118**, 102105 (2021). <https://doi.org:10.1063/5.0039766>
- 233 Fu, D. *et al.* Tuning the electrical transport of type II Weyl semimetal WTe<sub>2</sub> nanodevices by Ga<sup>+</sup> ion implantation. *Scientific Reports* **7**, 12688 (2017). <https://doi.org:10.1038/s41598-017-12865-8>
- 234 Yan, Z. *et al.* Highly stretchable van der Waals thin films for adaptable and breathable electronic membranes. *Science* **375**, 852-859 (2022). <https://doi.org:doi:10.1126/science.abl8941>
- 235 Wang, H. *et al.* Orientation-dependent large plasticity of single-crystalline gallium selenide. *Cell Reports Physical Science* **3**, 100816 (2022). <https://doi.org:https://doi.org/10.1016/j.xcrp.2022.100816>
- 236 Qiu, D., Chu, Y., Zeng, H., Xu, H. & Dan, G. Stretchable MoS<sub>2</sub> Electromechanical Sensors with Ultrahigh Sensitivity and Large Detection Range for Skin-on Monitoring. *ACS Applied Materials & Interfaces* **11**, 37035-37042 (2019). <https://doi.org:10.1021/acsami.9b11554>
- 237 Sui, F. *et al.* Sliding ferroelectricity in van der Waals layered  $\gamma$ -InSe semiconductor. *Nature Communications* **14**, 36 (2023). <https://doi.org:10.1038/s41467-022-35490-0>
- 238 Rogée, L. *et al.* Ferroelectricity in untwisted heterobilayers of transition metal dichalcogenides. *Science* **376**, 973-978 (2022). <https://doi.org:10.1126/science.abm5734>
- 239 Vazirisereshk, M. R., Martini, A., Strubbe, D. A. & Baykara, M. Z. Solid Lubrication with MoS<sub>2</sub>: A Review. *Lubricants* **7**, 57 (2019).
- 240 Scharf, T. W. & Prasad, S. V. Solid lubricants: a review. *Journal of Materials Science* **48**, 511-531 (2013). <https://doi.org:10.1007/s10853-012-7038-2>
- 241 El-Kady, M. F., Strong, V., Dubin, S. & Kaner, R. B. Laser Scribing of High-Performance and Flexible Graphene-Based Electrochemical Capacitors. *Science* **335**, 1326-1330 (2012). <https://doi.org:doi:10.1126/science.1216744>



- 242 Berman, D., Erdemir, A. & Sumant, A. V. Graphene: a new emerging lubricant. *Materials Today* **17**, 31-42 (2014). <https://doi.org/https://doi.org/10.1016/j.mattod.2013.12.003>
- 243 Akimov, I. V., Sylovanyuk, V. P., Volchok, I. P. & Ivantyshyn, N. A. Influence of the shape of graphite inclusions on the mechanical properties of iron-carbon alloys. *Materials Science* **48**, 620-627 (2013). <https://doi.org/10.1007/s11003-013-9546-x>
- 244 Berre, C. *et al.* Failure analysis of the effects of porosity in thermally oxidised nuclear graphite using finite element modelling. *Journal of Nuclear Materials* **381**, 1-8 (2008). <https://doi.org/https://doi.org/10.1016/j.jnucmat.2008.07.021>
- 245 Küpers, M. *et al.* Controlled Crystal Growth of Indium Selenide,  $\text{In}_2\text{Se}_3$ , and the Crystal Structures of  $\alpha\text{-In}_2\text{Se}_3$ . *Inorganic Chemistry* **57**, 11775-11781 (2018). <https://doi.org/10.1021/acs.inorgchem.8b01950>
- 246 Wong, L.-W. *et al.* Site-specific electrical contacts with the two-dimensional materials. *Nature Communications* **11**, 3982 (2020). <https://doi.org/10.1038/s41467-020-17784-3>
- 247 Barthel, J. Dr. Probe: A software for high-resolution STEM image simulation. *Ultramicroscopy* **193**, 1-11 (2018). <https://doi.org/https://doi.org/10.1016/j.ultramic.2018.06.003>
- 248 Thompson, A. P. *et al.* LAMMPS - a flexible simulation tool for particle-based materials modeling at the atomic, meso, and continuum scales. *Computer Physics Communications* **271**, 108171 (2022). <https://doi.org/https://doi.org/10.1016/j.cpc.2021.108171>
- 249 Jin-Wu, J. & Yu-Ping, Z. in *Handbook of Stillinger-Weber Potential Parameters for Two-Dimensional Atomic Crystals* (eds Jiang Jin-Wu & Zhou Yu-Ping) Ch. 1 (IntechOpen, 2017).
- 250 Jones, J. E. & Chapman, S. On the determination of molecular fields.—I. From the variation of the viscosity of a gas with temperature. *Proceedings of the Royal Society of London. Series A, Containing Papers of a Mathematical and Physical Character* **106**, 441-462 (1924). <https://doi.org/doi:10.1098/rspa.1924.0081>
- 251 Rappe, A. K., Casewit, C. J., Colwell, K. S., Goddard, W. A., III & Skiff, W. M. UFF, a full periodic table force field for molecular mechanics and molecular dynamics simulations. *Journal of the American Chemical Society* **114**, 10024-10035 (1992). <https://doi.org/10.1021/ja00051a040>
- 252 Grimme, S., Ehrlich, S. & Goerigk, L. Effect of the damping function in dispersion corrected density functional theory. *Journal of Computational Chemistry* **32**, 1456-1465 (2011). <https://doi.org/https://doi.org/10.1002/jcc.21759>
- 253 Henkelman, G., Uberuaga, B. P. & Jónsson, H. A climbing image nudged elastic band method for finding saddle points and minimum energy paths. *The Journal of Chemical Physics* **113**, 9901-9904 (2000). <https://doi.org/10.1063/1.1329672>
- 254 Nelson, R. *et al.* LOBSTER: Local orbital projections, atomic charges, and chemical-bonding analysis from projector-augmented-wave-based density-functional theory. *Journal of Computational Chemistry* **41**, 1931-1940 (2020). <https://doi.org/https://doi.org/10.1002/jcc.26353>
- 255 Hill, R. The Elastic Behaviour of a Crystalline Aggregate. *Proceedings of the Physical Society. Section A* **65**, 349 (1952). <https://doi.org/10.1088/0370-1298/65/5/307>



- 256 Voigt, W. Lehrbuch der Kristallphysik (Textbook of crystal physics). *BG Teubner, Leipzig und Berlin* (1928).
- 257 Reuss, A. Calculation of the flow limits of mixed crystals on the basis of the plasticity of monocrystals. *Z. Angew. Math. Mech* **9**, 49-58 (1929).
- 258 Chen, X.-Q., Niu, H., Li, D. & Li, Y. Modeling hardness of polycrystalline materials and bulk metallic glasses. *Intermetallics* **19**, 1275-1281 (2011). [https://doi.org:https://doi.org/10.1016/j.intermet.2011.03.026](https://doi.org/https://doi.org/10.1016/j.intermet.2011.03.026)
- 259 Duerloo, K.-A. N. & Reed, E. J. Structural Phase Transitions by Design in Monolayer Alloys. *ACS Nano* **10**, 289-297 (2016). [https://doi.org:10.1021/acsnano.5b04359](https://doi.org/10.1021/acsnano.5b04359)
- 260 Keum, D. H. *et al.* Bandgap opening in few-layered monoclinic MoTe<sub>2</sub>. *Nature Physics* **11**, 482-486 (2015). [https://doi.org:10.1038/nphys3314](https://doi.org/10.1038/nphys3314)
- 261 Hao, Q. *et al.* Phase Identification and Strong Second Harmonic Generation in Pure  $\epsilon$ -InSe and Its Alloys. *Nano Letters* **19**, 2634-2640 (2019). [https://doi.org:10.1021/acs.nanolett.9b00487](https://doi.org/10.1021/acs.nanolett.9b00487)
- 262 Sun, M. *et al.*  $\epsilon$ -InSe single crystals grown by a horizontal gradient freeze method. *CrystEngComm* **22**, 7864-7869 (2020). [https://doi.org:10.1039/D0CE01271H](https://doi.org/10.1039/D0CE01271H)
- 263 Dutta, A., Reid, C. & Heinrich, H. Simulation of Incoherent Scattering in High-Angle Annular Dark-Field Scanning Electron Microscopy. *Microscopy and Microanalysis* **19**, 852-853 (2013). [https://doi.org:10.1017/s1431927613006259](https://doi.org/10.1017/s1431927613006259)
- 264 Gao, Z. *et al.* High-throughput screening of 2D van der Waals crystals with plastic deformability. *Nature Communications* **13**, 7491 (2022). [https://doi.org:10.1038/s41467-022-35229-x](https://doi.org/10.1038/s41467-022-35229-x)
- 265 Grzonka, J., Claro, M. S., Molina-Sánchez, A., Sadewasser, S. & Ferreira, P. J. Novel Polymorph of GaSe. *Advanced Functional Materials* **31**, 2104965 (2021). [https://doi.org:https://doi.org/10.1002/adfm.202104965](https://doi.org/https://doi.org/10.1002/adfm.202104965)
- 266 Mesbah, A. *et al.* From Hydrated Ni<sub>3</sub>(OH)<sub>2</sub>(C<sub>8</sub>H<sub>4</sub>O<sub>4</sub>)<sub>2</sub>(H<sub>2</sub>O)<sub>4</sub> to Anhydrous Ni<sub>2</sub>(OH)<sub>2</sub>(C<sub>8</sub>H<sub>4</sub>O<sub>4</sub>): Impact of Structural Transformations on Magnetic Properties. *Inorganic Chemistry* **53**, 872-881 (2014). [https://doi.org:10.1021/ic402106v](https://doi.org/10.1021/ic402106v)
- 267 Qin, Z. *et al.* Ni-MOF composite polypyrrole applied to supercapacitor energy storage. *RSC Advances* **12**, 29177-29186 (2022). [https://doi.org:10.1039/D2RA04939B](https://doi.org/10.1039/D2RA04939B)
- 268 Monkhorst, H. J. & Pack, J. D. Special points for Brillouin-zone integrations. *Physical Review B* **13**, 5188-5192 (1976). [https://doi.org:10.1103/PhysRevB.13.5188](https://doi.org/10.1103/PhysRevB.13.5188)
- 269 Meyer, J. C. *et al.* Experimental analysis of charge redistribution due to chemical bonding by high-resolution transmission electron microscopy. *Nature Materials* **10**, 209-215 (2011). [https://doi.org:10.1038/nmat2941](https://doi.org/10.1038/nmat2941)
- 270 Demaison, J. & Wlodarczak, G. The equilibrium C-H bond length. *Structural Chemistry* **5**, 57-66 (1994). [https://doi.org:10.1007/BF02278696](https://doi.org/10.1007/BF02278696)
- 271 Demaison, J., Herman, M. & Lievin, J. The equilibrium OH bond length. *International Reviews in Physical Chemistry* **26**, 391-420 (2007). [https://doi.org:10.1080/01442350701371919](https://doi.org/10.1080/01442350701371919)